Statistical Aspects of Multi-Scale Structures

from Quantum Field in Curved Spacetimes

Ka Hei Choi

Doctoral Thesis

Ludwig-Maximilians-Universität München
Faculty of Physics
Munich, 2025

Statistical Aspects of Multi-Scale Structures from Quantum Field in Curved Spacetimes

Ka Hei Choi

München 2025

Statistical Aspects of Multi-Scale Structures from Quantum Field in Curved Spacetimes

Ka Hei Choi

Dissertation
an der Fakultät für Physik
der Ludwig-Maximilians-Universität
München

vorgelegt von
Ka Hei Choi
aus Hong Kong

München 2025

Erstgutacher/in: Prof. Dr. Stefan Hofmann
Zweitgutachter/in: Prof. Dr. Otmar Biebel
Tag der mündlichen Prüfung: 10.02.2026

Statistical Aspects of Multi-Scale Structures

from Quantum Field in Curved Spacetimes

Ka Hei Choi

Supervised by Prof. Dr. Stefan Hofmann

Second Referee:	Prof. Dr. Otmar Biebel
Third Referee:	PD Dr. Michael Haack
Chair Person:	Prof. Dr. Steffen Rulands

Date of submission:	09th December 2025
Date of Doctoral Examination:	10th February 2026

Arnold Sommerfeld Center of Theoretical Physics
Ludwig–Maximilians–Universität München
Faculty of Physics
Munich, 2025

Abstract

This thesis discusses the application and theoretical method of field theory in curved spacetimes across a wide range of physical scales. On the smallest scale, we investigate the limitations of the semiclassical framework, in which quantum fields evolve on a classical spacetime background. A diagnostic framework is developed to assess the validity of this approximation when it operates within strong gravitational fields. The resulting unitarity loss is an intrinsic feature of effective field theory that quantifies the degree to which the semiclassical approximation is violated. Next, we analyze the statistics of rare events in the early Universe using random fields that represent overdensities in the primordial density fluctuations. We extend the framework of extreme value statistics to consider random fields with nontrivial spatial correlation and finite-size effects. We show that, even in strongly spatially correlated fields, their tail behaviors of extreme values are preserved due to the statistical independence of rare events sampled by local maxima. Finally, using hydrodynamical simulations of cosmological structure formation, we analyze the unexpected decorrelation between thermal pressure and matter density in large-scale structures of the low-redshift Universe. We show that this decorrelation does not imply a breakdown of the linear bias relation between pressure and matter. Instead, such decorrelation can be accurately predicted by the halo model, where the one-halo term admits a physical interpretation as stochastic shot noise.

Zusammenfassung

Diese Dissertation behandelt die Anwendung und theoretische Methodik der Feldtheorie in gekrümmten Raumzeiten über ein breites Spektrum physikalischer Längenskalen hinweg. Auf den kleinsten Skalen untersuchen wir die Grenzen des semiklassischen Rahmens, in dem Quantenfelder auf einem klassischen Raumzeithintergrund evolvieren. Ein diagnostisches Rahmenwerk wird entwickelt, um die Gültigkeit dieser Näherung in Bereichen starker Gravitationsfelder zu bewerten. Der daraus resultierende Unitaritätsverlsut ist ein intrinsisches Merkmal der effektiven Feldtheorie und quantifiziert den Grad, zu dem die semiklassische Näherung verletzt wird. Anschließend analysieren wir die Statistik seltener Ereignisse im frühen Universum mithilfe von Zufallsfeldern, die Überdichten in den primordialen Dichtefluktuationen beschreiben. Dazu erweitern wir den Rahmen der Extremwertstatistik, um räumliche Korrelationen und endliche Systemgrößen zu berücksichtigen. Wir zeigen, dass selbst in stark räumlich korrelierten Feldern das Randverhalten der Extremwertverteilung erhalten bleibt, da seltene Ereignisse, die durch lokale Maxima erfasst werden, statistisch unabhängig bleiben. Schließlich untersuchen wir anhand hydrodynamischer Simulationen der kosmologischen Strukturbildung die unerwartete Entkopplung zwischen thermischem Druck und Materiedichte in großskaligen Strukturen des niederrotverschobenen Universums. Wir zeigen, dass diese Dekorrelation keinen Zusammenbruch der linearen Bias-Relation zwischen Druck und Materie impliziert. Vielmehr kann sie im Rahmen des Halo-Modells präzise beschrieben werden, wobei der Ein-Halo-Termen eine physikalische Interpretation als stochastisches Schrotrauschen zulässt.

Preface

This thesis discusses the theoretical methods of field in curved spacetimes across a wide range of scales, from quantum fluctuations in strong gravitational backgrounds, to the statistics of the large-scale structure Universe. In Chapter 1, we discuss quantum fluctuations interacting with spacetime geometry within the framework of effective field theory in curved spacetime. In particular, we present a rigorous diagnostic framework for investigating non-unitary evolution groups in relation to the breakdown of effective field theories in general semiclassical spacetimes. Our approach is based on local stability analysis of the algebra of observables in quantum field theory in curved spacetimes and the geometric concepts in the functional representation of quantum field theory. Within this representation, we demonstrated how to construct infinitely many self-adjoint extensions of the canonical conjugate momentum operator at the kinematical level, which, by usual functional analysis, extends to the Hamiltonian operator. However, the self-adjoint domains for the Hamiltonian generally do not intersect with the solution space of the functional Schrodinger equation, except in globally static spacetimes. This is related to the probability flows crossing the boundaries of the effective configuration field space, which leaks into configuration space that requires a more fundamental description. The loss of probability implies that the evolution of the effective field theory does not admit a unitary representation but instead a contractive evolution semigroup. The degree of unitarity loss, in turn, quantitatively assesses the quality of the semiclassical approximation. Numerical simulations based on the formal investigation are also performed to determine regions in cosmological spacetimes where the semiclassical approximation breaks down for a free quantum field.

Afterwards, we consider macroscopic fields that represent matter density fluctuations in the early Universe. Rare events in these fluctuations correspond to overdensities in regions that are relevant to the formation of massive galaxies, halos, and supermassive black holes observed in the high-redshift universe. So in Chapter 2, we analyze the statistics of rare events within spatially correlated random scalar fields. Our approach extends extreme value statistics to consider random events that are identically distributed but not independent. The simulated random fields model the small-scale primordial

density fluctuations, and are restricted to consider either the Gaussian or exponential statistics. In both cases, their spatial correlations are determined by their power spectra following an inverse power law with various spectral indices. We will present a spatial correlation analysis that uses correlation length to evaluate the necessary lower bound of the neighborhood size. This allows us to sample a well-defined local maximum, which intuitively generalizes the conventional notion of peaks in the random field statistics. Then we demonstrate that the population of rare events can be strongly enhanced within a cluster due to spatial correlations, yet the rare event statistics of spatially correlated fields converge to the same class of extreme value distribution as their uncorrelated counterparts. Lastly, we discuss how rare events and tail distributions can enhance non-sphericities of clusters.

Finally, in Chapter 3, we analyze the statistics of gas pressure and matter density on large scales in the low redshift universe. The electron pressure of hot gas in dark matter halos are linearly biased tracer of the matter density field on large scales, so their correlation is expected to improve with increasing length scales. However, simulations of cosmic structure formation have shown that the pressure-matter correlation decreases instead when considering scales greater than roughly 200Mpc, with an even stronger effect at lower redshift. As we will demonstrate, this decorrelation neither implies that pressure is not an excellent tracer of matter, nor the loss of predictability of the pressure distribution based solely on the information of the matter density field. In fact, it is entirely possible to predict pressure-matter decorrelation by the halo model even if the pressure is an excellent tracer of matter. This is caused by stochastic shot noise within individual halos, and the theoretically estimated decorrelation can then be used to recover the coherent relation between pressure and matter on a large scale.

In the Chapter 4 we will briefly discuss the outlook of this thesis which includes various topics of ongoing collaborations.

Contents

Chapter 1

Diagnostic Method for Quantum Field Theory in Curved-Spacetimes

The results presented in this chapter are based on a collaborative work with Stefan Hofmann and Marc Schneider, published in the Physical Review D on ***111*** *(2025) 2, 025019.*

1.1 Introduction

Physical theories, although constructed within rigorous mathematical frameworks, are formulated under assumptions abstracted from observations within a finite perceivable domain of reality. They provide effective descriptions of the observable structures of phenomena, and for that reason, there is little reason to regard any as truly fundamental; perhaps even more evident by the numerous unresolved divergencies or singularities that mark their limits.

Such recognition forms the conceptual foundation of effective (field) theory [1–10]. The central idea is to separate well-understood low-energy physics from the unknown higher-energy physics at smaller length scales by perturbative methods in the most general covariant form compatible with the symmetries of the system. This separation enables us to make reliable predictions of low-energy phenomena, and extension to describe higher-energy phenomena modeled by suppressed interaction terms.

In the case of gravity, General Relativity is remarkable in describing macroscopic phenomena such as stellar structures and cosmic expansion, and yet it is also known to be perturbatively non-renormalizable when formulated in quantum field theory. A parallel historical analogy once occurred is the Fermi theory of weak interactions: the ratio of the neutron decay rate to that of the muon diverges at one loop but becomes finite in the standard model [11–13]. On one hand, this analogy demonstrates an optimistic possibility that an apparently perturbatively non-renormalizable low-

energy macroscopic theory can emerge as a renormalizable theory in a "high-energy" microscopic description. But what is more interesting is that when Fermi theory operates outside its domain of validity, it begins to strongly violate unitarity when the effective description breaks down. If unitarity violation is a universal feature that signals the breakdown of an effective description, then by the same reasoning, unitarity violation should naturally occur in quantum field theory in curved spacetimes [14–18], since it is too an effective field theory that makes reliable predictions only within the perturbative and semiclassical approximation. The purpose of this chapter is to explore this nature expectation rigorously and to develop a diagnostic framework that relates unitarity violation to the validity of quantum field theory in curved spacetime.

The semiclassical framework of quantum field theory in curved spacetimes implies that already free quantum fields are coupled to and excited by the dynamics of the background geometries, while the dynamical background itself is assumed to be inert against the energy content of the quantum fluctuations. Specifically, consider spacetimes $(\mathcal{M}, g)$ for $\mathcal{M}$ is a smooth, four-dimensional spacetimes manifold, equipped with a Lorentzian metric g. Then, the action consists of the Einstein-Hilbert action and the matter field action are

$$\begin{aligned} S_g[g] &= \frac{2}{\kappa^2}\int \mathrm{d}^4x\ \sqrt{-g}R + \mathcal{O}(R^2) \\ S_m[\phi, g] &= \frac{1}{2}\int \mathrm{d}^4x\,\sqrt{-g}\Big[g^{-1}(\mathrm{d}\phi, \mathrm{d}\phi) - (m^2 + \zeta R)\phi^2\Big] + \mathcal{O}(R^2) \end{aligned} \tag{1.1}$$

where κ is a dimensionful parameter, $g = \det g$ is the metric tensor, R is the Ricci scalar and ζ is a coupling parameter. Terms of order R^2 and higher are relevant only when further generalizing the Einstein-Hilbert action to an even smaller length scale, which we will ignore for the purpose of this chapter. Suppose we split the gravitational field into a smooth background metric $\bar{g}$ and a small fluctuations h of the gravitational field $g = \bar{g} + \kappa h$, and perform a similar expansion for the matter field over its background value $\phi = \phi_0 + \kappa\delta\phi$. Then, expanding the Einstein-Hilbert and matter action in powers of κ yields corrections to the classical systems: $S = S_g^{(0)} + S_m^{(0)} + S_g^{(2)} + S_m^{(2)} + S_{\text{int}}^{(3)}$.

The linear contributions $S_g^{(1)} + S_m^{(1)}$ are absent because they vanish under Hamilton's principle of least action, that is, the background metric satisfies the Einstein's equations:

$$\bar{\mathrm{Ric}} - \frac{1}{2}g\bar{R} = 8\pi G T, \tag{1.2}$$

whose $T = \mathrm{d}\phi_0 \otimes \mathrm{d}\phi_0 + (1/2)(g^{-1}(\mathrm{d}\phi_0, \mathrm{d}\phi_0) - (m^2 - \zeta R)\phi_0^2)$ g is the energy-momentum stress tensor of the matter field. The terms $S_m^{(2)}$ and $S_g^{(2)}$ govern the dynamics of the matter and gravitational field fluctuation, respectively. Meanwhile, the leading interaction terms $S^{(3)} \propto -\kappa \int \mathrm{d}^4x \sqrt{-g}\, \langle \delta T, h \rangle$ describe the interaction between the energy-momentum stress tensor of the quantum matter field δT and the fluctuations of the gravitational field. Intuitively, the stability of background geometry requires[1] $|\bar{g}_{\mu\nu}| \gg |\kappa h_{\mu\nu}|$ for each μ, ν and $S_{\mathrm{int}}^{(3)} \approx 0$ when compared to $S^{(2)}$. The former is by definition such that the approximation $g \approx \bar{g}$ holds up to small perturbation relative to κh; The latter, however, holds only if $\langle \delta T, h \rangle$ is sufficiently small over the time interval of interest. So the assumption and approximation that classical background is stable simultaneously relies on δT to be small compared κ^{-1}. This assumption, for example, can be violated in spacetime regions where spacetime dynamics could excite large fluctuations of quantum fields. Due to these large fluctuations $S_{\mathrm{int}}^{(3)}$ is no longer negligible, which amplifies h and in turn cascades its effect to $S_{\mathrm{int}}^{(3)}$, and ultimately leads to the complete breakdown of the semiclassical framework.

The validity analysis of the effective semiclassical framework can even be extended to a more general setup by specifying a set of observables singled out by certain observers, which they intend to measure in particular regions of spacetime. Then statements concerning the stability of the classical background can be made relative to this chosen set of observables. From a technical perspective, the semiclassical approximation remains valid only if the probability of exciting quantum fluctuations outside the effective configuration space is negligible. This configuration space consists of all allowed quantum fluctuations consistent with the semiclassical approximation, and its boundary is determined by geometric arguments based on semi-norms constructed from the stability requirement of the background observables. The existence of such a boundary is crucial because there are no asymptotic conditions imposed on the quantum state (the

[1] This is only a rough estimation for the purpose of illustration. It does not hold, for example, when the off-diagonal terms of $|\bar{g}_{\mu\nu}|$ are strictly zero.

Schrödinger wave functional). So quantum observables must be evaluated within this effective configuration space, whose boundaries influence the spectral analysis of field operators. As we will show later, the canonical pair consisting of a real scalar field and its conjugate momentum field admits self-adjoint extensions on certain Hilbert spaces, and thereby they constitute the basic observables. However, this construction is purely kinematic: the corresponding Hilbert space must also intersect with the solution space of Schrödinger wave functionals, so that the self-adjoint realization also complies with the dynamic content of the theory.

In dynamical spacetimes, however, the Hamilton operator generally fails to satisfy this intersection property, even if it admits a self-adjoint extension at the kinematical level. Unitarity violations manifest either as probability sources or sinks. Probability sources cannot exist if the underlying quantum field theory is consistent in Minkowski spacetime. Thus, only probability sinks are possible. These can be interpreted as quantifying the degree to which the semiclassical approximation is invalidated, and have operational consequences which indicate the breakdown of the semiclassical framework.

The corresponding evolution operators of the semiclassical framework therefore form a contractive representation of the time translation group. In analogy with Stone's theorem, which establishes a one-to-one correspondence between self-adjoint operators to one-parameter unitary groups, contractive representations are generated by accretive operators [19]. This grants the semiclassical approximation predictive power and consistency. It also qualifies the underlying Hamiltonian as non-observable if regions of spacetime are considered that contain significant probability sinks.

The functional Schrödinger picture of quantum field theory (cf. [20–35] for details) provides a natural framework to address the issues discussed above, particularly in determining the domain of validity of the semiclassical approximation and the associated unitarity violation. In the absence of ghosts, such violations are tied to a significant probability flux leaving the effective configuration space. Whether probability non-conservation is acceptable depends on the resolution at which observables are measured. If unitarity violations remain tolerable within the spacetime region probed by a measurement process, then contractive representations generalize unitary evolution groups and retain predictive power even when the probabilistic framework underlying effective quantum theories becomes challenged.

The formal arguments presented in the main body of this chapter are then applied numerically using simulations based on Gaussian random fields. These numerical experiments illustrate the potential of our framework in concrete settings, such as free fields populating in contracting radiation-dominated universes evolving towards a future singularity and the asymptotic past of de Sitter universes. The simulations reveal spacetime regions where the semiclassical approximation fails, as diagnosed by a geometric stability criterion based on the algebra of observables.

1.2 Kinematical aspects

1.2.1 Configuration Spaces

Formal statements of semiclassical effective field theory are often expressed by expanding the fields around a classical background, $\phi(x) = \phi_{cl}(x) + \kappa\,\delta\phi(x) + \mathcal{O}(\kappa^2)$ and $g = \bar{g} + \kappa h + \mathcal{O}(\kappa^2)$, where $\kappa^{-1} = M_P$ is the Planck mass that serves as the smallness parameter. At the intuitive level, the perturbative framework then requires $|\phi_{cl}(x)| \gg |\kappa\delta\phi(x)|$ and $|\bar{g}_{\mu\nu}| \gg |\kappa h_{\mu\nu}|$ respectively, and higher orders terms $\mathcal{O}(\kappa^2)$ are negligible. While this requirement is almost true in many circumstances, it is insufficient in general. For example, consider a free quantum field with a trivial background classical fields $\phi_{cl} = 0$ or $h_{\mu\nu}$ for $\mu \neq \nu$ that has no classical counterpart if the classical metric is diagonal. In these cases, the inequality is ill-defined because the ratio $r \equiv |\kappa\delta\phi(x)|/\phi_{cl}$ diverges. Therefore, perturbative validity cannot be qualified solely using the field magnitudes, and it is necessary to consider a larger set of physical observables. This motivates other natural candidates, for example, the expectation value of the Hamiltonian or the two-point correlation function, which should remain bounded below the Planck scale. Such a bound then in turn restricts the allowed values of $\delta\phi(x)$ and h or informs the smallest length scales that the semiclassical framework can probe. Nevertheless, this approach faces two difficulties. First, their expectation value are not bounded from above due to ultraviolet divergence, so this only defines the smallest length scales but does not fully address the earlier discussion regarding the stability of the classical background; Second, the translation from the restriction of Hamiltonian and two-point functions into constraints on $\delta\phi(x)$ is not unique, which

requires careful implementation or otherwise may lead to a canonical momentum operator that cannot even be self-adjoint.

These consideration hints at the necessity of a rigorous construction for the effective framework of quantum field theory in curved spacetimes. As a first step, we will construct an effective instantaneous field configuration space that contains all the allowed quantum field configurations that are consistent with the assumptions made in quantum field theory in curved spacetimes based on a local description of fields and physical observables.

We begin by introducing the general properties of an instantaneous field configuration space. Let us consider the real vector bundle $\mathcal{C}_t$ over the hypersurface Σ_t for $t \in I$, which is the quadruple $(C_t, \pi_t, \Sigma_t, V)$ where C_t denotes the total space, π_t is the bundle projection of C_t onto the base Σ_t. For each point $p \in \Sigma_t$, $V(p)$ is a real vector space homeomorphic to the fibre $\pi^{-1}(p)$. Suppose $\mathcal{C}_t$ is the configuration bundle of instantaneous scalar field configurations, then $\mathcal{C}_t \equiv \Sigma_t \times \mathbb{R}$ is a trivial rank one bundle for real scalar fields. Instantaneous configuration fields ϕ are the smooth sections of the real vector bundle $\mathcal{C}_t$, and $\Gamma(\mathcal{C}_t)$ is the vector space that collects all the smooth sections. So this vector space consists of all possible values that the instantaneous scalar field configuration ϕ can take at all possible positions $p \in \Sigma_t$. Suppose the initial data is compactly supported in a region $\mathcal{K}_0 \subset \Sigma_{t_0}$ at initial time t_0, the causal future of the respective evolved field satisfying the normally hyperbolic equations is also supported inside a compact set $\mathcal{J}^+(\mathcal{K}_0) \cap \Sigma_t$ for any finite time $t \in I$, provided that the spacetime $\mathcal{M}$ is globally hyperbolic. Therefore, of particular physical interest, we consider the space of compactly supported smooth sections $\Gamma_c(\mathcal{C}_t)$ of the configuration bundle $\mathcal{C}_t$.

On the basis of the instantaneous field configuration space $\Gamma(\mathcal{C}_t)$, we proceed to construct the corresponding quantum theory, in which the states carry the probabilistic interpretation. Let us introduce the space $\Gamma^*(\mathcal{C}_t)$ that is dual to the configuration space $\Gamma(\mathcal{C}_t)$. The dual space contains the space of generalized complex-valued functionals $F : \Gamma(\mathcal{C}_t) \to \mathbb{C}$ that assign a complex number to each field configuration $\phi \in \Gamma(\mathcal{C}_t)$. A particularly important class of functionals in quantum field theory is the class of wave functionals $\Psi_t \in \Gamma^*(\mathcal{C}_t)$ that describe a quantum state. Let $(\Gamma(\mathcal{C}_t), \mathscr{D}\phi)$ be the formal measure space with a configuration space $\Gamma(\mathcal{C}_t)$ and a formal measure $\mathscr{D}\phi$. Then the complex vector space $\mathcal{L}^2(\Gamma(\mathcal{C}_t), \mathscr{D}\phi)$ is the space that consists of all

measurable complex-valued wave functionals Ψ_t, whose modulus is square integrable with respect to the formal Lebesgue measure $\mathscr{D}\phi$:

$$\|\Psi_t\|^2 = \int_{\Gamma(\mathcal{C}_t)} \mathscr{D}\phi \; |\Psi_t[\phi]|^2 \tag{1.3}$$

In general $\mathcal{L}^2(\Gamma(\mathcal{C}_t), \mathscr{D}\phi)$ contains the trivial subspace $\mathbb{L}(\Gamma(\mathcal{C}_t), \mathscr{D}\phi) \in \mathcal{L}^2(\Gamma(\mathcal{C}_t), \mathscr{D}\phi))$ which consists of wave functional that vanish $\mathscr{D}\phi$-almost everywhere. This subspace is excluded from our formal measure space by defining the quotient space:

$$L^2(\Gamma(\mathcal{C}_t, \mathscr{D}\phi) \equiv \mathcal{L}^2(\Gamma(\mathcal{C}_t, \mathscr{D}\phi)/\; \mathbb{L}(\Gamma(\mathcal{C}_t), \mathscr{D}\phi)\,. \tag{1.4}$$

Since (1.3) defines the formal norm of the wave functional, it must be normalizable to unity at the initial time because it has a probabilistic interpretation of total probability. By definition, the expectation values $\mathbb{E}(\mathcal{O}; \Psi_t)$ in probability theory for any bounded operator $\mathcal{O}$ on $L^2(\Gamma(\mathcal{C}_t), \mathscr{D}\phi)$ and unbounded operator with respect to the wave functional Ψ_t is:

$$\mathbb{E}(\mathcal{O}; \Psi_t) \equiv \int_{\Gamma(\mathcal{C}_t)} \mathscr{D}\phi \; \Psi_t^*[\phi]\, \mathcal{O}\, \Psi_t[\phi] \equiv \langle \mathcal{O} \rangle_{\Psi_t}\,, \tag{1.5}$$

The expectation value of the identity operator $\mathrm{id}_{\Gamma^*(\mathcal{C}_t)}$ is equivalent to the formal norm in the quotient space L^2. The above definition also hold for unbounded operators $\mathcal{O}$ only if Ψ_t lies in the domain $D(\mathcal{O}) = \{\Psi_t \in L^2(\Gamma(\mathcal{C}_t), \mathscr{D}\phi) \mid \mathbb{E}(\mathcal{O}; \Psi_t) < \infty\}$. In the following, we consider Ψ_t to be normalizable wave functionals and normalized to unity on the initial hypersurface Σ_{t_i}. Suppose $\mathcal{U}$ is a measurable subset and let $\chi_{\mathcal{U}}$ the characteristic functional $\chi_{\mathcal{U}} : \Gamma(\mathcal{C}_t) \to \{0, 1\}$ that restrict the field configuration space $\mathcal{C}_t$ onto the subset $\mathcal{U}$. Then, the probability

$$\mathbb{P}(\mathcal{U}) \equiv \|\Psi_t\|^2_{\mathcal{U}} = \|\Psi_{t_i}\|^{-2} \int_{\Gamma(\mathcal{C}_t)} \mathscr{D}\phi\, \Psi_t[\phi]\, \chi_{\mathcal{U}} \Psi_t[\phi] \tag{1.6}$$

is the probability to find any instantaneous field configuration populating on the hypersurface Σ_t for $t \in I$ restricted within the subset $\mathcal{U} \subset L^2(\Gamma(\mathcal{C}_t), \mathscr{D}\phi)$.

1.2.2 Effective Configuration Space

So far we have constructed the formal measure spaces $(\Gamma(\mathcal{C}_t), \mathscr{D}\phi)$ as the configuration space and introduced wave functionals Ψ_t in the dual vector bundle $\Gamma^*(\mathcal{C}_t)$ that are normalizable $\|\Psi_t\|^2 < \infty$, for all $t \in I \subset \mathbb{R}$. The current construction of the configuration space $\Gamma(\mathcal{C}_t)$ is completely general; this means that it can contain field configurations that are not necessarily consistent and admissible to a semiclassical treatment. The purpose of this section is to construct an effective configuration space that accommodates semiclassical assumptions based on physical observables.

At least for a free theory, it is possible to construct a complete set of quantum observables based on two elementary observables. The first elementary observable is the smeared configuration field operator $\Phi[f]$, where $f \in \Gamma_c(\mathcal{C}_t)$ is an smooth smearing functions of compact support

$$\Phi[f] = \int_{\Sigma_t} \mathrm{d}\mu(\boldsymbol{x})\ f(\boldsymbol{x})\, \Phi(\boldsymbol{x}) \tag{1.7}$$

where $\mathrm{d}\mu(\boldsymbol{x})$ is the covariant measure on the hypersurface Σ_t. The canonical field operator $\Phi(\boldsymbol{x})$ is defined to act as a multiplication operation over its domain in $\Gamma^*(\mathcal{C}_t)$ by $\Phi[f]\,\Psi_t[\phi] = \phi[f]\,\Psi_t[\phi]$ for $\phi(\boldsymbol{x}) \in \mathbb{R}$. This also means that the self-adjoint domain of $\Phi[f]$ is given by all wave functional in $L^2(\Gamma(\mathcal{C}_t), \mathscr{D}\phi)$, such that $\Phi[f]\Psi_t$ is in $L^2(\Gamma(\mathcal{C}_t), \mathscr{D}\phi)$ for all admissible smearing functions. The statistical moments of the wave functional are functional of $\phi[f] \in \mathbb{R}$. In the case of a free quantum field, the wave functional Ψ_t is Gaussian, and therefore its statistical properties are completely determined by the first and second moments of $\phi[f]$. The first moment gives the mean value of the Gaussian wave functional

$$\langle \Phi[f] \rangle \equiv \mathbb{E}[\Phi[f]; \Psi_t] = \int_{\Gamma(\mathcal{C}_t)} \mathscr{D}\phi\ \Psi_t^*[\phi]\phi[f]\Psi_t[\phi]\,. \tag{1.8}$$

Similarly, the second moment determines its variance

$$\langle \sigma^2[f] \rangle \equiv \mathbb{E}[\mathrm{I}_\Gamma^*\,;\, (\Phi[f] - \langle \Phi[f] \rangle)\Psi_t] = \int_{\Gamma(\mathcal{C}_t)} \mathscr{D}\phi\ \Psi_t^*[\phi]\,(\phi[f] - \langle \Phi[f] \rangle)^2\,\Psi_t[\phi]\,. \tag{1.9}$$

Note that for brevity we denoted $\mathrm{I}_{\Gamma^*} \equiv \mathrm{id}_{\Gamma^*(\mathcal{C}_t)}$ and $\mathrm{I}_{\Gamma} \equiv \mathrm{id}_{\Gamma(\mathcal{C}_t)}$. In this chapter the notation $\langle\, \cdot\, \rangle \equiv \mathbb{E}[\,\cdot\,;\Psi_t]$ denotes the expectation value and $\Psi_t \in L^2(\Gamma(\mathcal{C}_t), \mathscr{D}\phi)$ unless further specifications.

The second elementary physical observable is the smeared momentum field operator $\Pi[f]$ conjugated to $\Phi[f]$. The smeared momentum operator is required to satisfy

$$[\Phi[f_1], \Pi[f_2]] = \mathrm{i}\,(f_1, f_2)\,, \tag{1.10}$$

where $(f_1, f_2) \equiv \int_{\Sigma_t} \mathrm{d}\mu(\boldsymbol{x}) f_1(\boldsymbol{x}) f_2(\boldsymbol{x}_2)$ which implies that quantum fluctuations follow the Heisenberg uncertainty principle, and the field operators and their conjugate momentum are required to satisfy the canonical commutation relation $[\Phi(\boldsymbol{x}), \Pi(\boldsymbol{y})] = \mathrm{i}\delta^3(\boldsymbol{x}-\boldsymbol{y})\,\mathrm{I}$, for $\boldsymbol{x} \neq \boldsymbol{y}$ and $\delta^3(\boldsymbol{x}-\boldsymbol{y})$ is the Dirac-delta distribution function. Thus, the smeared momentum operator derivative

$$\Pi[f] = \int_{\Sigma_t} \mathrm{d}\mu(\boldsymbol{x})\, f(\boldsymbol{x})\, \Pi(\boldsymbol{x}) = \frac{1}{\mathrm{i}} \int_{\Sigma_t} \mathrm{d}\mu(\boldsymbol{x})\, \left(f(\boldsymbol{x}) \frac{\delta}{\delta\phi(\boldsymbol{x})} \right) \tag{1.11}$$

is the functional generalization of a directional derivative along the direction of $f(\boldsymbol{x})$ within the configuration space. The self-adjoitn domain of $\Pi[f]$ also encompasses wave functionals $\Psi_t \in L^2(\Gamma(\mathcal{C}_t), \mathscr{D}\phi)$ with $\Pi[f]\Psi_t \in L^2(\Gamma(\mathcal{C}_t), \mathscr{D}\phi)$ for all smooth smearing function f with compact support on Σ_t. Further specification on the domain of $\Pi[f]$ will be the focus of our discussion in a later section.

Based on the canonical operators, we can now construct quantum observables and compare them with classical observables that constitute the classical background of the semiclassical framework. In classical field theory, local linear observables are continuous linear functionals on the configuration space, which are elements in $\Gamma_{\mathrm{c}}^{\infty}(\mathcal{C}_t^*)$. General classical observables are obtained as the minimal polynomial algebra generated by the linear observables, namely the symmetric algebra $\mathrm{Sym}(\Gamma_{\mathrm{c}}^{\infty}(\mathcal{C}_t^*))$. For any classical field configuration $\phi_0 \in \Gamma(\mathcal{C}_t)$, there exists a corresponding neighborhood $U_0 \in \Gamma(\mathcal{C}_t)$ that contains all possible quantum fluctuations of ϕ over the classical field ϕ_0. The local observable $\mathcal{O} \in U_0$ is the collection of local data solely consisting of the value of the field configuration ϕ evaluated at position $\boldsymbol{p} \in \Sigma_t$, together with all its derivatives up to order $k \in \mathbb{N}$, which takes the form $\mathcal{O} = \omega \circ j^k$, where $j^k(t,p)[\phi]$ denotes the k-th jet prolongation of ϕ at $(t,p) \in I \times \Sigma_t$, and ω is a functional on the jet

bundle $j^k\Gamma(\mathcal{C}_t)$, which maps the local data to produce a real number. The canonical quantization prescription allows us to map any local observable to a bounded operator on $L^2(\Gamma(C_t), \mathscr{D}\phi)$. But note that the definition of local observables in classical field theory is adapted to a covariant framework, while the quantization prescription in the functional Schrödinger picture requires a foliation of spacetime into hypersurfaces.

Suppose the background field configuration $\phi_0 \in \ker(P)$ is a solution to some wave operator, for P is the Klein-Gordon operator when considering free scalar field, we choose a set $\mathcal{A}_0$ that contains finitely many local quantum observables with support in $U_0 \subset \Gamma(\mathcal{C}_t)$. Our first objective is to characterize U_0 further: For any quantum observable $\mathcal{O} \in \mathcal{A}_0$, their expectation value with respect to some wave functional Ψ_t are perturbations over the classical observable $\mathcal{O}_0$ evaluated at the background configuration,

$$\langle \mathcal{O} \rangle_{U_0} \equiv \mathcal{O}_0 + \langle \mathcal{O}[\phi] \rangle_{U_0} \,. \tag{1.12}$$

where we assumed that $\|\Psi_t\|_{U_0} \approx 1$, such that $\langle \mathcal{O}_0 \rangle = \mathbb{E}[\,\mathcal{O}_0\,\mathrm{I}_{U_0}\,;\Psi_t] = \mathcal{O}_0$ with $\mathcal{O}_0\,\mathrm{I}_{U_0}$ being the corresponding classical observables $\mathcal{O}_0$ that defines U_0, multiplied with the identity operator defined within U_0. This means that the initial quantum states excite field configurations that are mostly populated within U_0, so that this is a valid initial state consistent with the semiclassical approximation.

Based on local observables, we can define two essential criteria that the effective semiclassical framework must satisfy. The first one is the short-distance cutoff. Let d denote the length dimension of $\mathcal{O}_0$, and l marks the short-distance cutoff below which a more fundamental description is needed. Then $\mathcal{O}_l = l^d$ denotes the short-distance limit corresponding to the local observable $\mathcal{O}$. Now consider a dimensionless ratio

$$\mathcal{R}_l(\mathcal{O}, \Psi_t; U_0) \equiv \frac{\langle \mathcal{O} \rangle}{\mathcal{O}_l} = \frac{1}{\mathcal{O}_l} \int_{\Gamma(\mathcal{C}_t)} \mathscr{D}\phi \; \Psi_t^* \chi_{U_0} \, \mathcal{O}[\phi] \, \Psi_t = \frac{1}{\mathcal{O}_l} \int_{U_0} \mathscr{D}\phi \; \Psi_t^* \mathcal{O}[\phi] \, \Psi_t$$

Depending on the length dimension d of $\mathcal{O}$, the effective semiclassical description of the quantum field is well above its short-distance cutoff defined by $\mathcal{O}_l$ when

$$\begin{aligned} &|\mathcal{R}_l(\mathcal{O}, \Psi_t; U_0)| > 1, \qquad \text{for } d > 0 \\ &|\mathcal{R}_l(\mathcal{O}, \Psi_t; U_0)| < 1, \qquad \text{for } d < 0 \end{aligned} \tag{1.13}$$

These two conditions can be combined to a single condition on the short distance cutoff that demands

$$|\mathcal{R}_l^{-s}(\mathcal{O}, \Psi_t; U_0)| < 1 \tag{1.14}$$

where $s \equiv \text{sgn}(d) \in \{-1, 1\}$. This condition is further fortified by taking its supremium over all the neighborhoods. This is because, for a given classical field configuration ϕ_0, there exist infinitely many different choices of neighborhood U_0 with respect to ϕ_0. The particular choice of U_0 must be made by selecting a neighborhood U_0 that gives the largest possible value of $\mathcal{R}_l^{-s}(\mathcal{O}, \Psi_t; U_0)$; and still required to be bounded below unity. This also implies that U_0 is taken to be the largest possible neighborhood within $\Gamma(\mathcal{C}_t)$. This leads to our formal definition of filtration seminorm:

$$N(\mathcal{O}, \Psi_t; U_0) \equiv \sup_{U_0 \subset \Gamma(\mathcal{C}_t)} |\mathcal{R}_l^{-s}(\mathcal{O}; U_0)| \tag{1.15}$$

Suppose ${l_{\mathcal{O}}}^d$ denotes the length scale characterizing $\mathcal{O}$, then $N(\mathcal{O}, \Psi_t; U_0)$ scales as $(l/l_{\mathcal{O}})^{|d|}$ for either sign of d. As a result, for any sensible quantum fluctuations within any background configuration $\phi_0 \in \ker(P)$ for all $t \in I$, the effective framework is valid and above the short distance cutoff if the filtration seminorm satisfies

$$\max_{\mathcal{O} \in \mathcal{A}_0} N(\mathcal{O}, \Psi_t; U_0) < 1 \tag{1.16}$$

where the maximum over the set $\mathcal{A}_0$ must be taken because the validity must be guaranteed for all local observables $\mathcal{O} \in \mathcal{A}_0$. Any observable in $\mathcal{A}_0$ violating Eq. (1.16) indicates the necessity of a more fundamental framework characterized by a shorter distance cutoff $l_1 < l$, including $l_1 = 0$. This results in a set of $\mathcal{A}_0'$ that can, in principle, be described by an effective field theory with a short-distance cut-off l.

While (1.16) provides the condition that our effective framework is above the short-distance cutoff scale, it remains insufficient to guarantee the validity of the effective framework, as it does not imply that admissible fluctuations respect the

classical observables that constitute the background. By the same line of reasoning, we can construct a filtrating seminorm by considering

$$\mathcal{R}_0(\mathcal{O}, \Psi_t; U_0) = \frac{\langle \mathcal{O} \rangle}{\mathcal{O}_0} \tag{1.17}$$
$$N(\mathcal{O}, \Psi_t; U_0) \equiv \sup_{U_0 \subset \Gamma(\mathcal{C}_t)} |\mathcal{R}_0(\mathcal{O}, \Psi_t; U_0)|$$

such that the classical background with respect to the local observable $\mathcal{O} \in \mathcal{A}_0$ is stable provided that

$$\max_{\mathcal{O} \in \mathcal{A}_0} N(\mathcal{O}, \Psi_t; U_0) \leq \delta \tag{1.18}$$

where δ is assumed to be in the open interval of $(0, 1)$. The value $\delta = 0$ is excluded since it corresponds to a trivial quantum fluctuation relative to $\mathcal{A}_0$, while $\delta = 1$ is also excluded because this corresponds to quantum fluctuations that generate expectation values $\langle \mathcal{O} \rangle$ with the same magnitude as the classical observable that constitutes the classical background. So provided a local set of quantum observables in $\mathcal{A}_0$ and a quantum state Ψ_t, δ serves two different purposes: On one hand, it defines the tolerance of error accumulated in the semiclassical approaches due to the deformation of the classical background due to quantum effects. On the other hand, it provides the meaning of a resolution scale relative to $\mathcal{A}_0$, and quantifies the extent to which the background configuration can be distinguished from fluctuations based on the local quantum observables in $\mathcal{A}_0$. It is possible to develop the latter interpretation for future works considering actual measurement processes, and we leave this for discussion in the outlook.

1.2.3 Symmetric and Self-Adjointness of Operators

So far we have discussed the construction of an effective configuration space based on the criteria: a short distance cutoff and the stability of the classical background based on the expectation values of a chosen set of local physical observables. Up to this point, these expectation values of observables are assumed to be generated from a self-adjoint operator. This is, however, not necessarily the case when the effective configuration space is compact, i.e., it contains boundaries at a finite distance from the origin ϕ_0 of

the neighborhood U_0. Such boundaries can influence the spectral properties of these local operators and may prevent the realization of self-adjointness within the compact effective field configuration space. A particular example is the functional momentum operator $\mathcal{P}$. For this reason, in this section, we analyze the spectral properties of fundamental local observables within the compact domain and demonstrate that they can indeed admit a self-adjoint extension to the effective configuration space. This requires showing first that the operator is closable, and then identifying its possible self-adjoint realizations consistent with the imposed boundary conditions.

Functional Momentum Operator

Let $U \subseteq U_0$ denote a subset of $\Gamma(\mathcal{C}_t)$ in accordance with Eq. (1.16) and (1.18), which consists of quantum fluctuations around a stable classical background describing some effective field theory well above the short distance cutoff. Consider the neighborhood U that is bounded by two sections ϕ_{L} and ϕ_{H} in $\Gamma(\mathcal{C}_t)$ which construct its the configuration space geometric relative to $\mathbb{R}$ along Σ_t. On each Σ_t, the neighbourhood $U = \cup_{\boldsymbol{x}\in\Sigma_t} U_{\boldsymbol{x}}$ and $U_{\boldsymbol{x}} = [\phi_{\mathrm{L}}(\boldsymbol{x}), \phi_{\mathrm{H}}(\boldsymbol{x})] \subset \mathbb{R}$ for all position $\boldsymbol{x} \in \Sigma_t$.

Let $D(\mathcal{P}) = \mathcal{C}^{\infty}_{U}(\Gamma(\mathcal{C}_t), \mathbb{C})$ be the domain of $\mathcal{P}$ which is the space of smooth complex-valued functions with compact support; and let $D(\mathcal{P}^1) = C^1_U(\Gamma(\mathcal{C}_t))$ be the domain of $\mathcal{P}_1$ is the space of once continuously differentiable functions with compact support. Both $D(\mathcal{P}) = \mathcal{C}^{\infty}_{U}(\Gamma(\mathcal{C}_t), \mathbb{C})$ and $D(\mathcal{P}^1) = C^1_U(\Gamma(\mathcal{C}_t))$ are subjected to boundary conditions on ∂U and $\mathcal{P}[f]$ is the functional generalization of directional derivatives in the direction of $f \in \mathcal{C}^{\infty}_{\mathrm{c}}(\Sigma_t)$:

$$\mathcal{P}_{\phi}[f]\Psi[\phi] \equiv \int_{\Sigma_t} \mathrm{d}\mu(\boldsymbol{x})\; f(\boldsymbol{x})\, \mathcal{P}_{\phi(\boldsymbol{x})}\Psi[\phi] \tag{1.19}$$

where $\mathcal{P}_{\phi(\boldsymbol{x})} \equiv -\mathrm{i}\delta/\delta\phi(\boldsymbol{x})$ contains the functional derivative with respect to $\phi(\boldsymbol{x})$. Let us introduce the approximate identity

$$I_{\epsilon}[\phi] = \prod_{\boldsymbol{x}\in\Sigma_t} i_{\epsilon}(\phi(\boldsymbol{x})) \tag{1.20}$$

that is assumed to be in $D(\mathcal{P})$, and i_{ϵ} is a smooth approximated distribution identity $\{i_{\epsilon}(x)\}$, which are real positive infinitely differentiable functions with support in

$\Delta U = (-1, 1)$ so that $\int_{-\infty}^{\infty} i_\epsilon(\phi(\boldsymbol{x}))\, \mathrm{d}\phi(\boldsymbol{x}) = 1$ for all $\boldsymbol{x} \in \Sigma_t$ and converges to the Dirac-delta distribution in the limit $\epsilon \to 0$. Then I_ϵ gives the functional generalization of the Dirac-delta distribution at the limit $\epsilon \to 0$: Let us consider any functional $F[\phi]$ and define

$$F_\epsilon[\psi] = \int_U \mathscr{D}\phi\ I_\epsilon[\psi - \phi] F[\phi]\,. \tag{1.21}$$

Then the absolute differences between $F_\epsilon[\psi]$ and $F[\psi]$ is

$$\begin{aligned} |F_\epsilon[\psi] - F[\psi]| &\leq \int_U \mathscr{D}\phi\ I_\epsilon[\phi - \psi]\, |F[\psi] - F[\phi]| \\ &\leq \left(\sup_{S_U} |F[\psi] - F[\phi]| \right) \int_U \mathscr{D}\phi\ I_\epsilon[\phi - \psi] \\ &\leq \sup_{S_U} |F[\psi] - F[\phi]|\,, \end{aligned} \tag{1.22}$$

where the supremum is taken over the set $S_U \equiv \{\psi \in U : \sup_{\Sigma_t} |\psi - \phi| < \epsilon\}$. The first line follows from the triangle inequality, then the properties of the approximate identity, and finally, in the third line, follows from the definition of the supremum as the least upper bound estimate. So in the limit $\epsilon \to 0^+$, ψ smoothly approximates ϕ, with accuracy determined by how close i_ϵ converges to the Dirac-delta distribution. As a consequence, the right-hand side of the above inequality converges to zero and $F_\epsilon \to F \in L^2(U, \mathscr{D}\phi)$.

Since the functional approximate identity I_ϵ is in the domain $D(\mathcal{P})$, we can evaluate $\mathcal{P}$ on the one-parameter family of the functional Ψ_ϵ:

$$\begin{aligned} \mathcal{P}_\phi[f] \Psi_t^\epsilon[\phi] &= \int_U \mathscr{D}\varphi\ \left(\mathcal{P}_\phi[f] I_\epsilon[\phi - \varphi] \right) \Psi[\varphi] \\ &= \int_U \mathscr{D}\varphi\ I_\epsilon[\phi - \varphi]\ \left(\mathcal{P}^1_\varphi[f]\, \Psi[\varphi] \right) + \mathcal{B}^\epsilon_{\partial U}[\Psi_t, f] \end{aligned} \tag{1.23}$$

where on the second line we used the Leibniz rule of functional derivative. The boundary term $\mathcal{B}^\epsilon_{\partial U}[\Psi_t, f]$ must vanish, so that it is consistent with (1.16) and (1.18)

for a free field theory. This, as a consequence, further restricts the domain of $\mathcal{P}_\phi$ for every point $\boldsymbol{x} \in \Sigma_t$ explicitly by:

$$\mathcal{B}^\epsilon_{\partial U}[\Psi_t, f] = -\mathrm{i}\int_{\Sigma_t} \mathrm{d}^3\boldsymbol{x}\, f(\boldsymbol{x}) \int_{U\setminus U(\boldsymbol{x})} \mathscr{D}\varphi\, \Big[I_\epsilon[\phi-\varphi]\,\Psi_t[\varphi]\Big]\Big|_{\partial U(\boldsymbol{x})} \equiv 0 \quad (1.24)$$

where $U \setminus U(x) \equiv \cup_{\boldsymbol{p}\in\Sigma_t, \boldsymbol{p}\neq\boldsymbol{x}} U(\boldsymbol{p})$ denotes the neighborhood that is comprised of all the neighborhood $U(\boldsymbol{p})$ for $\boldsymbol{p} \in \Sigma_t$ except $U(\boldsymbol{x})$ at the given point $\boldsymbol{x}$.[2] Since $\mathcal{B}^\epsilon_{\partial U} = 0$, we are left with

$$\mathcal{P}_\phi[f]\Psi^\epsilon_t[\phi] = \int_U \mathscr{D}\phi\, I_\epsilon[\phi-\varphi]\, \big(\mathcal{P}^1_\varphi[f]\Psi[\varphi]\big) \quad (1.25)$$

Altogether with our previous result, we have shown that $\Psi^\epsilon \to \Psi \in L^2(U, \mathscr{D}\phi)$ and $\mathcal{P}[f]\Psi^\epsilon[\phi] \to \mathcal{P}^1[f]\Psi[\phi] \in L^2(U, \mathscr{D}\phi)$ as $\epsilon \to 0^+$. This shows that the closure of the graph of $\mathcal{P}$ contains the graph of $\mathcal{P}^1$, so $\mathcal{P}$ is closable.

Symmetric and Self-adjoint Extension

After we have shown that the momentum operator is closable on a neighborhood U, we will now demonstrate that $\mathcal{P}$ admits a symmetric extension, and then also infinitely many self-adjoint extensions. Suppose $\mathcal{O}$ is a densely defined operator on $L^2(\Gamma(\mathcal{C}_t), \mathscr{D}\phi)$, then it is called **symmetric** (or Hermitian) if $\mathcal{O} \subset \mathcal{O}^*$, that means the domain $D(\mathcal{O}) \subset D(\mathcal{O}^*)$ and $\mathcal{O}\Psi = \mathcal{O}^*\Psi$ for all $\Psi \in D(\mathcal{O})$. Equivalently, $\mathcal{O}$ is symmetric if and only if

$$\langle \mathcal{O}\Psi, \Phi\rangle = \langle \Phi, \mathcal{O}\Psi\rangle \quad (1.26)$$

[2] Specifically, the functional integral that integrates over the neighborhood $U \setminus U(\boldsymbol{x})$ is defined as follow

$$\int_{U\setminus U(x)} \mathscr{D}\phi = \prod_{\boldsymbol{p}\in\Sigma_t, \boldsymbol{p}\neq\boldsymbol{x}} \int_{\phi_L(\boldsymbol{p})}^{\phi_H(\boldsymbol{p})} \mathrm{d}\phi(\boldsymbol{p})$$

for all $\Psi, \Phi \in D(\mathcal{O})$[3]. On the other hand, $\mathcal{O}$ is called **self-adjoint** if $\mathcal{O} = \mathcal{O}^*$, that means $\mathcal{O}$ is symmetric and the domains

$$D(\mathcal{O}) = D(\mathcal{O}^*). \tag{1.27}$$

First of all, to show that $\mathcal{P}[f]$ is symmetric, let us consider the set $AC(U)$ of all absolutely continuous functionals on U with values in $\mathbb{C}$. Define the domain of $\mathcal{P}$ as

$$D(\mathcal{P}) = \{\Phi \in AC(U) : \Phi|_{\partial U} = 0\}. \tag{1.28}$$

The functional momentum operator $\mathcal{P}$ is densely defined and $\mathcal{P}$ is symmetric if the adjoint $\mathcal{P}^*$ satisfies

$$\langle \mathcal{P}[f]\, \Psi, \Phi\rangle = \langle \Psi, \mathcal{P}^*[f]\Phi\rangle \tag{1.29}$$

for $\Psi \in D(\mathcal{P}^*)$. Suppose $U_1 \subset U$, and $\mathcal{J}^\epsilon_{U_1} \in D(\mathcal{P})$ is a smooth approximation of the indicator functional that is the product of local indicator functions $j^\epsilon_{U_1}(\phi(\boldsymbol{x}))$

$$\mathcal{J}^\epsilon_{U_1}[\phi] = \prod_{\boldsymbol{x}\in\Sigma_t} j^\epsilon_{U_1}(\phi(\boldsymbol{x})) \tag{1.30}$$

and $j^\epsilon_{U_1}$ is constructed from smooth approximation of the identity function i^ϵ, so that by construction $j^\epsilon_{U_1}$ is compactly support within $U_1(\boldsymbol{x})$

$$\lim_{\epsilon\to 0^+} j^\epsilon_{U_1}(\phi(\boldsymbol{x})) = \lim_{\epsilon\to 0^+}\left[i^\epsilon(\phi^{U_1}_H(\boldsymbol{x})) - i^\epsilon(\phi^{U_1}_L(\boldsymbol{x}))\right] = \begin{cases} 1 & \text{if } \phi(\boldsymbol{x}) \in U_1(\boldsymbol{x}), \\ 0 & \text{otherise}. \end{cases}$$

with $\partial U = \cup_{\boldsymbol{x}\in\Sigma_t}\partial U(\boldsymbol{x})$ for each $\partial U_1(\boldsymbol{x}) = \{\phi^{U_1}_L(x), \phi^{U_1}_H(x)\}$ for all $\boldsymbol{x} \in \Sigma_t$. So at the limit $\epsilon \to 0$, $\mathcal{J}^\epsilon_{U_1}$ reduces the neighborhood of the functional integral from U to U_1:

$$\lim_{\epsilon\to 0^+}\langle \mathcal{J}^\epsilon_{U_1}, \mathcal{P}[f]\Psi\rangle = \lim_{\epsilon\to 0^+}\int_U \mathscr{D}\phi\ \mathcal{J}^\epsilon_{U_1}[\phi]\, F[\phi] = \int_{U_1}\mathscr{D}\phi\ F[\phi], \tag{1.31}$$

[3]Only in this section, we will borrow the Greek symbol Φ to denote a wave functional instead of the instantaneous field operator

for any functional $F[\phi]$. Consider $\Psi = \mathcal{J}^{\epsilon}_{U_1} \in D(\mathcal{P}^*)$ in (1.29), the right side becomes

$$\lim_{\epsilon\to 0^+}\langle \mathcal{J}^{\epsilon}_{U_1}, \mathcal{P}^*[f]\,\Phi\rangle = \int_{U_1} \mathscr{D}\phi\ \mathcal{P}^*[f]\,\Phi[\phi] \tag{1.32}$$

On the left-hand side of (1.29), using the Leibniz rule we obtain

$$\begin{aligned}&\lim_{\epsilon\to 0^+}\langle \mathcal{P}[f]\mathcal{J}^{\epsilon}_{U_1}, \Phi\rangle \\ &\qquad = \frac{1}{\mathrm{i}}\int_{\Sigma_t} \mathrm{d}^3x\ f(\boldsymbol{x})\left[\int_{U_1}\mathscr{D}\phi\ \frac{\delta}{\delta\phi(\boldsymbol{x})}\Phi[\phi] - \int_{U}\mathscr{D}\phi\,\frac{\delta}{\delta\phi(\boldsymbol{x})}\left(\mathcal{J}^{\epsilon}_{U_1}\Phi[\phi]\right)\right]\end{aligned} \tag{1.33}$$

The last term on the second line is a boundary term evaluated on ∂U. This is zero because by definition $U_1 \subset U_0$, so $\partial U \cap U_1 = \emptyset$. As a result, comparing (1.32) and (1.33) in the limit $\epsilon \to 0^+$, fiberwise we have

$$\int_{U_1}\mathscr{D}\phi\ \mathcal{P}^*[f]\,\Phi[\phi] = \frac{1}{\mathrm{i}}\int_{\Sigma_t}\mathrm{d}\mu(\boldsymbol{x})f(\boldsymbol{x})\int_{U_1\setminus U_1(\boldsymbol{x})}\mathscr{D}\phi\ \Phi[\phi]\Big|_{\partial U_1(x)} \tag{1.34}$$

which means that Φ is absolutely continuous and $\mathcal{P}^*[f]\Phi[\phi] = (f, -\mathrm{i}\delta_\phi)\Phi[\phi]$ for $\Phi \in D(\mathcal{P}^*)$ and $\delta_\phi \equiv \delta/\delta\phi$ with $(f, -\mathrm{i}\delta_\phi) \equiv -\mathrm{i}\int_{\Sigma_t}\mathrm{d}\mu(\boldsymbol{x})\ f(\boldsymbol{x})(\delta/\delta\phi(\boldsymbol{x}))$. This concludes that $D(P^*) = AC(U)$ and $\mathcal{P}^* = -i\delta_\phi$ is symmetric.

While $\mathcal{P}$ is symmetric, it is not essentially self-adjoint because $D(\mathcal{P}^*) \subset D(\mathcal{P})$, but self-adjointness requires $D(\mathcal{P}) = D(\mathcal{P}^*)$ as indicated in (1.27). It is easy to show that a symmetric operator is not essentially self-adjoint even if it satisfies (1.26). Suppose $\mathcal{P} = (f, -\mathrm{i}\delta_\phi)$ on $L^2(U, \mathscr{D}\phi)$ and $D(\mathcal{P}) = \{\Psi \in AC(U) : \Psi|_{\partial U} = 0\}$; while $D(\mathcal{P}^*) = \{\Phi \in AC(U)\}$. Then, for $\Psi \in D(\mathcal{P})$ and $\Phi \in D(\mathcal{P}^*)$, we compute the differences

$$\Delta(\mathcal{P}[f]) \equiv \langle \mathcal{P}[f]\Psi, \Phi\rangle - \langle \Psi, \mathcal{P}^*[f]\Phi\rangle \tag{1.35}$$

The differences $\Delta(\mathcal{P}[f]) \equiv 0$ follows from (1.26) if $\Delta(\mathcal{P}[f])$ is symmetric. If $\mathcal{P}[f]$ is symmetric, the above condition is automatically satisfied just by imposing the boundary condition $\Psi[\phi]|_U = 0$:

$$\begin{aligned}\Delta(\mathcal{P}(f)) &= \mathrm{i}\int_{\Sigma_t} \mathrm{d}\mu(\boldsymbol{x}) f(\boldsymbol{x}) \int_U \mathscr{D}\phi \, \frac{\delta}{\delta\phi(\boldsymbol{x})}\Big(\Psi^*[\phi]\Phi[\phi]\Big) \\ &= \mathrm{i}\int_{\Sigma_t} \mathrm{d}\mu(\boldsymbol{x}) f(\boldsymbol{x}) \int_{U\setminus U(\boldsymbol{x})} \mathscr{D}\phi \, \Big(\Psi^*[\phi]\Phi[\phi]\Big)\Big|_{\partial U(\boldsymbol{x})} = 0 \end{aligned} \tag{1.36}$$

So (1.26) holds without imposing any boundary conditions on the wave functionals $\Phi \in D(\mathscr{P}^*)$ in the domain of the corresponding adjoint operator. This means that the boundary condition enforced by the domain of the functional momentum operator $\Psi \in D(\mathcal{P})$ is so strong, such that $\Delta(\mathcal{P}[f]) = 0$ it is not required to impose any boundary conditions on those wave functionals $\Phi \in D(\mathcal{P}^*)$. This demonstrates that $D(\mathcal{P}^*) \subset D(\mathcal{P})$ and shows that the functional momentum operator $\mathcal{P}$ defined this way is symmetric but not necessarily self-adjoint.

To seek self-adjoint extensions of $\mathscr{P}[f]$, we need to extend the set of functional in $D(\mathscr{P})$ by allowing more general boundary conditions. To do so, assume there exists a self-adjoint extension to $\mathcal{P}$ that we denote as $\mathscr{P}$. In the domain $D(\mathscr{P})$ we exclude the set of functionals that possess the strict boundary conditions $\Psi|_{\partial U}= 0$, so that the domain of $\mathscr{P}$excludes the domain of $\mathcal{P}$, $\Psi \in D(\mathscr{P})\setminus D(\mathcal{P})$. Again, consider the residue

$$\Delta(\mathscr{P}(f)) = \langle \mathscr{P}[f]\,\Psi, \Psi\rangle - \langle \Psi, \mathscr{P}^*[f]\Psi\rangle \equiv 0$$

where the last equality is given by requiring $\mathscr{P}$ is symmetric. By the same procedure, we obtain the boundary term that is required to vanish if the differences $\Delta(\mathscr{P}(f)) \equiv 0$:

$$\int_{\Sigma_t} \mathrm{d}\mu(\boldsymbol{x}) f(\boldsymbol{x}) \int_{U\setminus U(\boldsymbol{x})} \mathscr{D}\phi \; |\Psi[\phi]|^2\Big|_{\partial U(\boldsymbol{x})} = 0 \tag{1.37}$$

This condition must hold equally on all $\boldsymbol{x} \in \Sigma_t$, meaning that

$$\int_{U\setminus U(x)} \mathscr{D}\phi \, |\Psi[\phi]|^2\big|_{\partial U(\boldsymbol{x})} = \prod_{\boldsymbol{p}\in\Sigma_t, \boldsymbol{p}\neq\boldsymbol{x}} \int_{U(\boldsymbol{p})} \mathrm{d}\phi(\boldsymbol{p}) \, |\Psi[\phi]|^2\big|_{\partial U(\boldsymbol{x})} = 0 \tag{1.38}$$

for all $\boldsymbol{x} \in \Sigma_t$ and let $\partial U(\boldsymbol{p}) = \{\phi_H(\boldsymbol{p}), \phi_L(\boldsymbol{p})\}$. Given that $\Psi \notin D(\mathcal{P})$, we excluded the possibility that $\Psi[\phi]|_{\partial U} = 0$, so $\Delta(\Pi(f)) = 0$ holds if and only if there exists complex-valued functions $\alpha(\boldsymbol{x})$ for all $\boldsymbol{x} \in \Sigma_t$ with unit modulus. Since field configurations ϕ are elements of the infinite-dimensional effective configuration space, they can be decomposed as $\phi = \int_{\Sigma_t} \mathrm{d}^3x \; |\boldsymbol{x}\rangle\langle\boldsymbol{x}|\phi\rangle \equiv \int_{\Sigma_t} \mathrm{d}^3x \, \phi(\boldsymbol{x}) \, e_{\boldsymbol{x}}$ where $e_{\boldsymbol{x}} \equiv |\boldsymbol{x}\rangle$ is the set of basis vector denoting all $\boldsymbol{x} \in \Sigma_t$. Using this decomposition, we can evaluate the field ϕ at the boundary $\partial U(\boldsymbol{x})$ explicitly in (1.38) and rewrite it as

$$\Psi(\zeta_L(\boldsymbol{x})) - \alpha(\boldsymbol{x}) \, \Psi(\zeta_H(\boldsymbol{x})) = 0 \, . \tag{1.39}$$

The function $\zeta_a(\boldsymbol{x})$ for $a = \{L, H\}$ is the field configuration ϕ evaluated at the boundary $\partial U(\boldsymbol{x})$ only locally at point $\boldsymbol{x}$. Specifically,

$$\zeta_a(\boldsymbol{x}) \equiv \phi|_{\phi_a(\boldsymbol{x})} = \int_{\Sigma_t} \mathrm{d}^3\boldsymbol{x}' \; \phi(\boldsymbol{x}') e_{\boldsymbol{x}'} \Big|_{\phi_a(\boldsymbol{x})} = (\mathcal{X}_{\boldsymbol{x}}, \phi) + \phi_a(\boldsymbol{x}) \, e_{\boldsymbol{x}} \, , \tag{1.40}$$

and $(\mathcal{X}_{\boldsymbol{x}}, \phi)$ by construction excludes the contribution of the position $\boldsymbol{x}$ from the spatial integral:

$$(\mathcal{X}_{\boldsymbol{x}}, \phi) \equiv \int_{\Sigma_t} \mathrm{d}^3x' \, \phi(\boldsymbol{x}') e_{\boldsymbol{x}'} - \lim_{\epsilon \to 0} \int_{\Sigma_t} \mathrm{d}^3x' \; (i_\epsilon(\boldsymbol{x}' - \boldsymbol{x}) \phi(\boldsymbol{x}') e_{\boldsymbol{x}'}) \tag{1.41}$$

As a consequence, the conditions (1.38) and (1.39) are required to hold for any functional in $D(\mathscr{P})$ with the same function α such that $\Delta(\mathscr{P}(f))$ vanishes. Now, consider $\Pi_\alpha[f] = (f, -\mathrm{i}\delta_\phi)$ with the domain

$$D(\Pi_\alpha) = \left\{ \Psi \in AC(U) : \Psi(\zeta_L(\boldsymbol{x})) = \alpha(\boldsymbol{x}) \, \Psi(\zeta_H(\boldsymbol{x})), \; |\alpha(\boldsymbol{x})| = 1, \; \forall \, \boldsymbol{x} \in \Sigma_t \right\} .$$

It is clear that $D(\mathscr{P}) \subset D(\Pi_\alpha)$. Since Π is symmetric and $\mathscr{P}$ is by assumption the self-adjoint extension of Π, we have $\mathscr{P} = \Pi_\alpha$ for some function $\alpha : \Sigma_t \to \mathbb{C}$ with $|\alpha| = 1$.

Now, we will see that the symmetric extension of Π_α can lead to a self-adjoint extension. Let $\Psi \in D(\Pi_\alpha)$ and $\Phi \in D(\Pi_\alpha^*)$, then $\Delta(\mathcal{P}[f])$ is

$$\Delta(\Pi[f]) = \mathrm{i} \int_{\Sigma_t} \mathrm{d}^3\boldsymbol{x} \int_{U\setminus U(\boldsymbol{x})} \mathscr{D}\phi \left(\Phi^*[\phi]\Psi[\phi]\right)\Big|_{\partial U(\boldsymbol{x})} \tag{1.42}$$

which is required to vanish $\forall \boldsymbol{p} \in \Sigma_t$ and $\boldsymbol{p} \neq \boldsymbol{x}$, meaning that the integrand vanishes:

$$\int_{U\setminus U(\boldsymbol{x})} \mathscr{D}\phi \left(\Phi^*[\phi]\Psi[\phi]\right)\big|_{\partial U(\boldsymbol{x})} = \prod_{\boldsymbol{p}\in\Sigma_t, \boldsymbol{p}\neq\boldsymbol{x}} \int_{U(\boldsymbol{p})} \mathrm{d}\phi(p) \left(\Phi^*[\phi]\Psi[\phi]\right)\big|_{\partial U(\boldsymbol{x})} = 0\,. \tag{1.43}$$

This indicates that on each position $\boldsymbol{x} \in \Sigma_t$, the following relation holds for some function $\alpha : \Sigma_t \to \mathbb{C}$ and $|\alpha| = 1$:

$$\alpha^*(\boldsymbol{x})\Phi^*(\zeta_H(\boldsymbol{x}))\Psi(\zeta_H(\boldsymbol{x})) = \Phi^*(\zeta_L(\boldsymbol{x}))\Psi(\zeta_L(\boldsymbol{x}))\,. \tag{1.44}$$

Since $\Psi \in D(\mathcal{P}_\alpha)$, inserting $\Psi(\zeta_H(\boldsymbol{x})) = \alpha(\boldsymbol{x})\Psi(\zeta_L(\boldsymbol{x}))$ reveals

$$\alpha^*(\boldsymbol{x})\Phi^*(\zeta_H(\boldsymbol{x})) = \Phi^*(\zeta_L(\boldsymbol{x}))\,. \tag{1.45}$$

Therefore the general boundary conditions motivated by $D(\Pi_\alpha)$ must impose the same boundary condition to $D(\Pi_\alpha^*)$, such that the domain $D(\Pi_\alpha) = D(\Pi_\alpha^*)$. Consequently, we conclude that all symmetric extensions of the momentum operator Π_α admit infinitely many self-adjoint extensions, which are indexed by a complex value function $\alpha(\boldsymbol{x})$ with $|\alpha(\boldsymbol{x})| = 1$ on Σ_t.

Hamilton Operator

In this section, we will extend our study to consider the Hamilton operator of a free quantum field and the conditions under which the Hamiltonian could admit a self-adjoint extension. In almost all circumstances, the potential term in the Hamilton operator is self-adjoint, and therefore the operator of interest is the kinetic part of this Hamiltonian, which is given by the functional generalization of the Laplace operator.

Let us introduce the quadratic form $\mathcal{Q} : D(\Pi) \times D(\Pi) \to \mathbb{C}$ on the form domain of $D(\Pi)$. For $\Phi, \Psi \in D(\Pi)$, $\mathcal{Q}$ is defined by

$$\mathcal{Q}(\Phi, \Psi) \equiv \langle \Pi\Phi, \Pi\Psi \rangle \tag{1.46}$$

such that $\mathcal{Q}(\,\cdot\,, \Psi)$ and $\mathcal{Q}(\Phi, \,\cdot\,)$ is conjugate linear and linear respectively, and $\mathcal{Q}(\Phi, \Psi) = \mathcal{Q}(\Psi, \Phi)$ if $\mathcal{Q}$ is symmetric. Physically, since $\mathcal{Q}$ is associated with the kinetic part of the Hamilton operator, for any healthy theory with physical degrees of freedom, $\mathcal{Q}$ cannot be negative, so formally $\mathcal{Q}(\Psi, \Psi) = \|\Pi\Psi\|^2 \geq 0$. and satisfies the Cauchy–Schwarz inequality $|\mathcal{Q}(\Phi, \Psi)| \leq \|\Pi\Phi\| \, \|\Pi\Psi\|$. Previously, we have shown that Π is closed, so the quadratic form $\mathcal{Q}$ will inherit this property and therefore is closed positive. Then it follows from the Kato's representation theorem [36] that the closed positive quadratic form $\mathcal{Q}$ guarantees the existence of a unique self-adjoint opeartor $\mathcal{T}_\phi$ associated with $\mathcal{Q}$, satisfying:

$$\mathcal{Q}(\Phi, \Psi) = \langle \Phi, \mathcal{T}_\phi \Psi \rangle, \tag{1.47}$$

with the domain $D(\mathcal{T}_\phi) \subseteq D(\Pi)$. To identify the domain of $\mathcal{T}_\phi$, we define the inner product on $D(\Pi) \subset L^2(\Gamma(\mathcal{C}_t), \mathscr{D}\phi)$ by

$$\langle \Phi, \Psi \rangle_{D(\Pi)} = \mathcal{Q}(\Phi, \Psi) + \langle \Phi, \Psi \rangle. \tag{1.48}$$

Let $(D(\Pi))^*$ be the space of bounded conjugated linear functional on $D(\Pi)$, then let $\jmath$ be the linear embedding of $L^2(\Gamma(\mathcal{C}_t), \mathscr{D}\phi)$ into $(D(\Pi))^*$ by

$$L^2(\Gamma(\mathcal{C}_t), \mathscr{D}\phi) \ni \Psi \xrightarrow{\jmath} \langle\, \cdot, \Psi \,\rangle \in (D(\Pi))^* \tag{1.49}$$

which is bounded due to the Cauchy-Schwarz inequality

$$|(\jmath(\Phi))(\Psi)| \leq \|\Psi\| \|\Phi\| \leq \|\Psi\|_{D(\Pi)} \|\Phi\| \tag{1.50}$$

Let id be the identity map that embeds $D(\Pi)$ in $L^2(\Gamma(\mathcal{C}_t), \mathscr{D}\phi)$, we have the following sequence of embedding

$$D(\Pi) \overset{\text{id}}{\to} L^2(\Gamma(\mathcal{C}_t), \mathscr{D}\phi) \overset{\jmath}{\to} (D(\Pi))^* \tag{1.51}$$

leading to the following chain of inclusion:

$$D(\Pi) \subset L^2(\Gamma(\mathcal{C}_t), \mathscr{D}\phi) \subset (D(\Pi))^* \tag{1.52}$$

Define the mapping $\tilde{\Pi} : L^2(\Gamma(\mathcal{C}_t)), \mathscr{D}\phi) \to (D(\Pi))^*$ by

$$(\tilde{\Pi}^*\Phi)(\Psi) \equiv \langle \Phi, \Pi\Psi \rangle \ , \tag{1.53}$$

then by the definition of adjoint operator $D(\Pi^*) = \{\Phi : \tilde{\Pi}^*\Phi \in L^2(\Gamma(\mathcal{C}_t), \mathscr{D}\phi)\}$, and Π equals to Π^* is restricted to the domain $D(\Pi^*)$. Now, let $\tilde{\mathcal{T}} : D(\Pi) \to D(\Pi)^*$ be the nature map by $\langle \tilde{\mathcal{T}}\Phi, \Psi \rangle \equiv \mathcal{Q}(\Phi, \Psi)$, then we have

$$D(\mathcal{T}) = \{\Phi \in D(\Pi) : \tilde{\mathcal{T}}\Phi \in L^2(\Gamma(\mathcal{C}_t), \mathscr{D}\phi)\} \tag{1.54}$$

and $\mathcal{T}$ equals to $\tilde{\mathcal{T}}$ restricted to the domain $D(\mathcal{T})$. Now suppose $\Phi, \Psi \in D(\Pi)$, then

$$[\tilde{\Pi}^*(\Pi\Phi)](\Psi) = \mathcal{Q}(\Phi, \Psi) = \langle \Pi\Phi, \Pi\Psi \rangle = (\tilde{\mathcal{T}}\Phi)(\Psi) \tag{1.55}$$

so that $\tilde{\mathcal{T}} = \tilde{\Pi}^*\Pi$ such that

$$\begin{aligned} D(\mathcal{T}) &= \{\Phi \in D(\Pi) : \tilde{\mathcal{T}}\Phi \in L^2(\Gamma(\mathcal{C}_t), \mathscr{D}\phi)\} \\ &= \{\Phi \in D(\Pi) : \Pi^*(\Pi\Phi) \in L^2(\Gamma(\mathcal{C}_t), \mathscr{D}\phi)\} \\ &= \{\Phi \in D(\Pi) : \Pi\Phi \in D(\Pi^*)\} \\ &= D(\Pi^*\Pi) \end{aligned} \tag{1.56}$$

where $\mathcal{T}$ equals to $\tilde{\mathcal{T}}$ restricted to the domain $D(\mathcal{T})$. The first equality is just the quoted result on the domain of $\mathcal{T}_\varphi$, the second equality follows from $\bar{\mathcal{T}}_\varphi = \bar{\mathcal{P}}^*\mathcal{P}$. As a result, the self-adjoint operator associated with the closed positive quadratic form $\mathcal{Q}$ is given by $\mathcal{T} = \Pi^*\Pi$.

1.3 Dynamical aspects

1.3.1 Momentum Operator

From the previous section, we have shown that it is always possible to construct a momentum operator Π and its quadratic form $\mathcal{Q}$ with infinitely many self-adjoint extensions on a kinematic level in an effective configuration field space subjected to boundaries at a finite distance. This possibility, however, does not necessarily imply compatibility with the dynamics imposed by the Schrödinger equation for any wave functional $\Psi_t[\phi] \in D(\Pi)$.

In this section, we present the dynamic analysis to supplement the kinematic statements. We proceed in three steps: first, we investigate, for Gaussian wave-functionals, under which criterion the Hamilton operator $\mathcal{H}$ admits a self-adjoint extension on the kinematic level. Second, we introduce the dynamics provided by the functional Schrödinger equation and examine the corresponding solution space. Third, we show that only static spacetimes provide the possibility for such self-adjoint extensions that are respected by the dynamics.

We begin with determining the self-adjoint domain $D(\Pi)$ of a Gaussian state $\Psi_t[\phi]$ in $L^2(U, \mathscr{D}\phi)$. Consider $\Psi_t[\phi] \in AC(U)$ takes the form

$$\Psi_t[\phi] = \mathcal{N}_t \mathcal{F}_t[\phi] \tag{1.57}$$

where $\mathcal{F}_t = \exp\left(-(1/2)\mathcal{K}_2[\phi]\right)$ and $\mathcal{K}_2[\phi]$ is a bikernel functional $\mathcal{K}_2 : U \times U \to \mathbb{C}$ while $\mathcal{N}_t \in \mathbb{C}$ is the normalization factor that will be determined by solving the functional Schrodinger equation. Then, the essential criteon for $\Psi_t[\phi]$ to live in the domain $D(\Pi)$ follows from (1.38)

$$\int_{U\setminus U(\boldsymbol{x})} \mathscr{D}\phi \; |\mathcal{F}_t(\zeta_L(\boldsymbol{x}))| = \int_{U\setminus U(\boldsymbol{x})} \mathscr{D}\phi \; |\mathcal{F}_t(\zeta(\boldsymbol{x}))|^2 \tag{1.58}$$

where $\mathcal{F}[\phi]|_{\partial U(\boldsymbol{x})} = \mathcal{F}_t(\zeta_a(\boldsymbol{x}))$ for $a = \{L, H\}$ indicates that the Gaussian wave functional is evaluated at the boundary $\partial U(\boldsymbol{x})$. In particular, we consider (1.38) because the functional integral by construction completely eliminate the possibility to recast the boundary elements $\partial U(\boldsymbol{x}) = \{\phi_L(\boldsymbol{x}), \phi_H(\boldsymbol{x})\}$ as a functional of $\phi(\boldsymbol{x}')$ for

$\boldsymbol{x}' \neq \boldsymbol{x}$. This is an important consistency requirement since the boundary elements are, by definition, cutoff values imposed by how the effective configuration space is defined.

It should be noted that although (1.58) holds true for the choice $\phi_H(\boldsymbol{x}) = \phi_L(\boldsymbol{x}) = \phi_\Lambda(\boldsymbol{x})$, this is equivalent to choosing a trivial configuration space $U = \{\emptyset\}$ because $\partial U(\boldsymbol{x}) = \{\phi_\Lambda(\boldsymbol{x}), \phi_\Lambda(\boldsymbol{x})\}$ for all $\boldsymbol{x} \in \Sigma_t$ and $\phi_\Lambda(\boldsymbol{x}) \in \mathbb{R}$. For non-trivial choices of U and $\Psi \in D(\Pi)$, consider the symmetric boundary conditions $\phi_\Lambda(\boldsymbol{x}) = \phi_H(\boldsymbol{x}) = -\phi_L(\boldsymbol{x})$ for all $\boldsymbol{x} \in \Sigma_t$. This leads to the functional integral being parity even by mapping $\phi(\boldsymbol{x}') \to -\phi(\boldsymbol{x}')$ for all $\boldsymbol{x}' \in \Sigma_t$ and $\boldsymbol{x}' \neq \boldsymbol{x}$:

$$\int_{U\setminus U(\boldsymbol{x})} \mathscr{D}\phi = \prod_{\boldsymbol{x}'\in\Sigma_t, \boldsymbol{x}'\neq\boldsymbol{x}} \int_{-\phi_\Lambda(\boldsymbol{x}')}^{\phi_\Lambda(\boldsymbol{x}')} \mathrm{d}\phi(\boldsymbol{x}') \longrightarrow \prod_{\boldsymbol{x}'} \int_{+\phi_\Lambda(\boldsymbol{x}')}^{-\phi_\Lambda(\boldsymbol{x}')} (-\,\mathrm{d}\phi(\boldsymbol{x}')) = \int_{U\setminus U(\boldsymbol{x})} \mathscr{D}\phi$$

where in the last equality sign we have reabsorbed the negative sign into the integral individually for each $\boldsymbol{x}' \in \Sigma_t$ and $\boldsymbol{x}' \neq \boldsymbol{x}$. Note that the mapping $\phi(\boldsymbol{x}') \to -\phi(\boldsymbol{x}')$ also preserves $\mathcal{F}(\zeta_a(\boldsymbol{x}))$ because the arguments within the exponential is also parity even. Consider

$$\begin{aligned} \zeta_a^{\otimes 2}(\boldsymbol{x}) &= \left(\phi_a(\boldsymbol{x})\, e_{\boldsymbol{x}} + (\mathcal{X}_{\boldsymbol{x}}, \phi)\, e_{\boldsymbol{x}'}\right)^{\otimes 2} \\ &= \phi_a(\boldsymbol{x})\, e_{\boldsymbol{x}} \otimes \phi_a(\boldsymbol{x}) e_{\boldsymbol{x}} + \phi_a(\boldsymbol{x}) e_{\boldsymbol{x}} \otimes (\mathcal{X}_{\boldsymbol{x}'}, \phi) \\ &\quad + (\mathcal{X}_{\boldsymbol{x}}, \phi) \otimes \phi_a(\boldsymbol{x})\, e_{\boldsymbol{x}} + (\mathcal{X}_{\boldsymbol{x}'}, \phi) \otimes (\mathcal{X}_{\boldsymbol{x}'}, \phi) \end{aligned} \tag{1.59}$$

Mapping $\phi(\boldsymbol{x}') \to -\phi(\boldsymbol{x}')$ for all $\boldsymbol{x}'$ and $\boldsymbol{x} \neq \boldsymbol{x}'$, and use the fact that $\phi_L(\boldsymbol{x}) = -\phi_H(\boldsymbol{x})$ for all $\boldsymbol{x} \in \Sigma_t$, we obtain $\zeta_L^{\otimes 2}(\boldsymbol{x}) \longrightarrow \zeta_H^{\otimes 2}(\boldsymbol{x})$. Accordingly, the entire functional under the mapping $\phi(\boldsymbol{x}) \to -\phi(\boldsymbol{x}')$ is given by

$$\int_{U\setminus U(\boldsymbol{x})} \mathscr{D}\phi\, |\mathcal{F}_t(\zeta_L(\boldsymbol{x}))|^2 \longrightarrow \int_{U\setminus U(\boldsymbol{x})} \mathscr{D}\phi\, |\mathcal{F}_t(\zeta_H(\boldsymbol{x}))|^2\,, \tag{1.60}$$

which concludes that (1.58) can be satisfied if $\partial U(\boldsymbol{x}) = \{-\phi_\Lambda(\boldsymbol{x}), \phi_\Lambda(\boldsymbol{x})\}$ for all $\boldsymbol{x} \in \Sigma_t$. Accordingly, there exists infinitely many self-adjoint extensions of $\mathcal{P}_\alpha$ provided the domain

$$D(\mathcal{P}_\alpha) = \{\Psi_t \in AC(U) : \Psi(\zeta_H(\boldsymbol{x})) = \alpha(\boldsymbol{x})\Psi(\zeta_L(\boldsymbol{x})), \\ \partial U(\boldsymbol{x}) = \{-\phi_\Lambda(\boldsymbol{x}), \phi_\Lambda(\boldsymbol{x})\},\ \forall \boldsymbol{x} \in \Sigma_t\}\,. \tag{1.61}$$

As a consequence, the requirement that the canonical momentum operator must be self-adjoint imposes a strong criterion on the choice of U. That is, it is not enough to consider arbitrary neighborhood U, but the criterion (1.16) and (1.18) will determine the boundary $\partial U(\boldsymbol{x})$ for all $\boldsymbol{x} \in \Sigma_t$, such that the neighborhood U contains field configurations that describes a physical theory.

1.3.2 Hamilton Operator

The immediate follow-up question is whether the Hamilton operator for a free scalar field admits similar self-adjoint extensions. If so, then on what condition does the Hamilton operator admit a self-adjoint extension? The answer to this question is mainly concerned with the spectrum of the kinetic operator $\Pi^*\Pi$. Consider $\Psi_t \in D(\Pi)$, in order for the kinetic operator $\Pi^*\Pi$ to be self-adjoint, it requires $\Pi\Psi_t[\phi] \in D(\Pi)$ with the same $\alpha(\boldsymbol{x})$ with unit modulus. For brevity, let us define $\chi_t[\phi] \equiv -i(f, \delta_\phi)\Psi_t[\phi]$, $\Pi\Psi_t[\phi] \in D(\Pi)$ implies that the following relation must be satisfied for $|\chi_t[\phi]|^2$:

$$\int_{\Sigma_t} \mathrm{d}\mu(\boldsymbol{x})\, f(\boldsymbol{x}) \int_{U\setminus U(\boldsymbol{x})} \mathscr{D}\phi\ |\chi_t[\phi]|^2\Big|_{\partial U(\boldsymbol{x})} = 0\,, \tag{1.62}$$

which is equivalent to the following two possibilities imposed on χ_t:

$$\chi_t(\zeta_H(\boldsymbol{x})) = \alpha(\boldsymbol{x})\chi_t(\zeta_L(\boldsymbol{x}))\,, \tag{1.63}$$

$$\chi_t(\zeta_H(\boldsymbol{x})) = \alpha^*(\boldsymbol{x})\chi_t^*(\zeta_L(\boldsymbol{x}))\,, \tag{1.64}$$

such that $\Pi^*\Pi$ admit self-adjoint extension. Since Ψ_t is Gaussian,

$$\chi_t[\phi] = i(f, \delta_\phi \mathcal{K}_2)[\phi]\, \Psi_t[\phi]\,. \tag{1.65}$$

Combined with the fact that $\Psi \in D(\Pi)$, the first condition (1.63) can be recast into a requirement for $\mathcal{K}_2$:

$$\Big[(f,\delta_\phi\mathcal{K}_2)(\zeta_H(\boldsymbol{x})) - (f,\delta_\phi\mathcal{K}_2)(\zeta_L(\boldsymbol{x}))\Big]\Psi_t(\zeta_H(\boldsymbol{x})) = 0\,. \tag{1.66}$$

We can evaluate the functional derivative explicitly

$$\begin{aligned}(f,\delta_\phi\mathcal{K}_2)(\zeta_H(\boldsymbol{x})) &= \left[\int_{\Sigma_t} \mathrm{d}^3x\; f(\boldsymbol{x})\,\frac{\delta}{\delta\phi(\boldsymbol{x})}\mathcal{K}_2[\phi,\phi;t]\right]\Big|_{\phi=\zeta_H(\boldsymbol{x})}\\ &= \int_{\Sigma_t}\mathrm{d}^3x\int_{\Sigma_t}\mathrm{d}^3x'\; f(\boldsymbol{x})\,K_2(\boldsymbol{x}',\boldsymbol{x};t)\,\phi(\boldsymbol{x}')\Big|_{\phi=\zeta_H(\boldsymbol{x})}\\ &= \int_{\Sigma_t}\mathrm{d}^3\boldsymbol{x}\, f(\boldsymbol{x})\,\Big\{K_2(\boldsymbol{x},\boldsymbol{x};t)\,\phi_H(\boldsymbol{x}) + (\mathcal{X}_{\boldsymbol{x}},K_2'[\phi])\Big\},\end{aligned} \tag{1.67}$$

where the last term in the third line is

$$(\mathcal{X}_{\boldsymbol{x}},K_2'[\phi]) = \int_{\Sigma_t}\mathrm{d}\mu(\boldsymbol{x}')\,K_2(\boldsymbol{x},\boldsymbol{x}';t)\,\phi(\boldsymbol{x}')\Big[\,\mathrm{id}_U - i_\epsilon(\phi(\boldsymbol{x})-\phi_\Lambda(\boldsymbol{x}))\Big]\,, \tag{1.68}$$

Inserting the above expression into (1.66), reduce to the conditions on ϕ for all $\boldsymbol{x}\in\Sigma_t$, K_2 and Ψ_t:

$$(\phi_H(\boldsymbol{x})-\phi_L(\boldsymbol{x}))K_2(\boldsymbol{x},\boldsymbol{x};t)\Psi_t = 0\,. \tag{1.69}$$

First of all, $\Psi_t(\zeta_H(\boldsymbol{x}))=0$ are already excluded from the domain of $D(\Pi)$ from the previous kinematic constructions. The second possibility that $K_2(\boldsymbol{x},\boldsymbol{x};t)=0$ for all $\boldsymbol{x}\in\Sigma_t$ is also excluded because $K_2(\boldsymbol{x},\boldsymbol{x};t)=0$ is the trivial solution that does not correspond to any physical Gaussian wave functionals. This leaves us with the only possibility $\phi_L(\boldsymbol{x})=\phi_H(\boldsymbol{x})$ for all $\boldsymbol{x}\in\Sigma_t$, which indicates a trivial configuration space $U=\{\emptyset\}$.

Since the first condition covers only trivial solutions, we consider the second condition instead. Using $\Psi_t(\zeta_H(\boldsymbol{x})) = \alpha^*(\boldsymbol{x})\Psi_t^*(\zeta_L(\boldsymbol{x}))$, we find

$$0 = \big[\,(f,\delta_\phi)\mathcal{K}_2(\zeta_H(\boldsymbol{x})) + ((f,\delta_\phi)\mathcal{K}_2(\zeta_L(\boldsymbol{x})))^*\,\big]\;\Psi_t(\zeta_H(\boldsymbol{x}))\,. \tag{1.70}$$

Inserting the explicit form of the functional derivative term, we have

$$0 = \int_{\Sigma_t} \mathrm{d}\mu(\boldsymbol{x})\, f(\boldsymbol{x}) \Big[2\mathrm{Im}K_2(\boldsymbol{x},\boldsymbol{x};t)\phi_H(\boldsymbol{x}) - \int_{\Sigma_t} \mathrm{d}\mu(\boldsymbol{x}')\, f(\boldsymbol{x}')\, \mathrm{Re}K_2(\boldsymbol{x},\boldsymbol{x}';t)(\mathcal{X}_{\boldsymbol{x}}, \phi(\boldsymbol{x}')) \Big] \Psi_t(\zeta_H(\boldsymbol{x}))\,, \tag{1.71}$$

where we have used the fact that $\phi_H(\boldsymbol{x}) = -\phi_L(\boldsymbol{x})$ because $\Psi_t[\phi] \in D(\Pi)$. Again, we integrate out all possible $\phi(\boldsymbol{x}')$ by the consistency requirement that the boundary elements $\partial U(\boldsymbol{x}) = \{\phi_L(\boldsymbol{x}), \phi_H(\boldsymbol{x})\}$ for all $\boldsymbol{x} \in \Sigma_t$ is not a functional of $\phi(\boldsymbol{x}')$ for all $\boldsymbol{x}' \in \Sigma_t$ and $\boldsymbol{x}' \neq \boldsymbol{x}$. The necessary requirement for self-adjoint extensions can be further condensed by multiplying both sides with $\Psi_t(\zeta_H(\boldsymbol{x}))$ before we integrate over all possible $\phi(\boldsymbol{x}')$. So the second term in (1.71) at each point $\boldsymbol{x} \in \Sigma_t$ becomes

$$\int_{\Sigma_t} \mathrm{d}^3\boldsymbol{x}'\, f(\boldsymbol{x}')\, \mathrm{Re}K_2(\boldsymbol{x},\boldsymbol{x}';t) \int_{U\setminus U(\boldsymbol{x})} \mathscr{D}\phi\ (\mathcal{X}_{\boldsymbol{x}}, \phi(\boldsymbol{x}'))\, |\Psi_t(\zeta_H(\boldsymbol{x}))|^2 = 0\,, \tag{1.72}$$

which vanishes at all $\boldsymbol{x}' \in \Sigma_t$ for $\boldsymbol{x}' \neq \boldsymbol{x}$. This property follows from $\Psi_t \in D(\Pi)$, that the momentum operator admits a self-adjoint extension for all points $\boldsymbol{x}' \in \Sigma_t$ and $\boldsymbol{x}' \neq \boldsymbol{x}$ because

$$\int_{U\setminus U(\boldsymbol{x})} \mathscr{D}\phi\ (\mathcal{X}_{\boldsymbol{x}}, \phi(\boldsymbol{x}'))\, |\Psi_t(\zeta_H(\boldsymbol{x}))|^2 \propto \int_{U\setminus U(\boldsymbol{x})} \frac{\delta}{\delta\phi(\boldsymbol{x}')} |\Psi_t(\zeta_H(\boldsymbol{x}))|^2 = 0 \tag{1.73}$$

As such, we are left with the necessary condition

$$\mathrm{Im}K_2(\boldsymbol{x},\boldsymbol{x};t)\phi_H(\boldsymbol{x}) \int_{U\setminus U(\boldsymbol{x})} \mathscr{D}\phi\ |\Psi_t(\zeta_H(\boldsymbol{x}))|^2 = 0\,. \tag{1.74}$$

This suggests three possible criteria: the first criterion is that the following term vanishes for all $\boldsymbol{x} \in \Sigma_t$,

$$\int_{U\setminus U(\boldsymbol{x})} \mathscr{D}\phi\ |\Psi_t(\zeta_H(\boldsymbol{x}))|^2 = 0, \tag{1.75}$$

which is only possible either $\Psi_t(\zeta_H(\boldsymbol{x})) = 0$ or the functional integration over $|\Psi_t(\zeta_H(\boldsymbol{x}))|^2$ is zero. The condition that $\Psi_t(\zeta_H(\boldsymbol{x})) = 0$ can be met only if $\Psi_t[\phi]$ is compactly supported within U. But since U is compact and $\Psi_t \in D(\Pi)$, the condition $\Psi_t(\zeta_H(\boldsymbol{x})) = 0$ cannot be met in this case. The second possibility is that $\phi_H(\boldsymbol{x}) = -\phi_L(\boldsymbol{x}) = \phi_\Lambda(\boldsymbol{x}) = 0$ for all $\boldsymbol{x} \in \Sigma_t$. This results in the trivial scenario where $U = \{\emptyset\}$. Since we are not interested in a trivial configuration space, we consider $\phi_\Lambda(\boldsymbol{x}) \neq 0$ and reject this possibility. Given that $U \neq \{\emptyset\}$, we are left with the possibility $\mathrm{Im}K_2(\boldsymbol{x}, \boldsymbol{x}; t) = 0$ for all $\boldsymbol{x} \in \Sigma_t$, which will mark the criterion for $\Pi^*\Pi$ to admit self-adjoint extensions.

Subsequent analysis is to investigate under what circumstances the imaginary part of the bikernel function vanishes for the Gaussian wave functional $\Psi_t \in D(\Pi)$. In its most general form, all $\Psi_t[\phi]$ that can be associated with physical systems are solutions to the functional Schrodinger equation

$$i\partial_t \Psi_t[\phi] = H_t[\Pi, \Phi]\Psi_t[\phi]\,, \tag{1.76}$$

where the Hamilton operator $H_t[\Pi, \Phi]$ in the foliation can be decomposed into

$$H_t[\Pi, \Phi] = H_\perp[\Pi, \Phi] + H_\parallel[\Pi, \Phi] \tag{1.77}$$

for which the Hamiltonian can be further decomposed into a kinetic term $A[\Pi]$ and a potential term $V[\Phi]$

$$H_\perp[\Pi, \Phi] = \frac{1}{2}\left(A[\Pi] + V[\Phi]\right)\,,. \tag{1.78}$$

Individual terms in $H_\perp[\Pi, \Phi]$ for free quantum fields are explicitly

$$A[\Pi] = \int_{\Sigma_t} \mathrm{d}\mu(x)\; N_\perp(\boldsymbol{x}) f(\boldsymbol{x})\, \frac{\Pi^2(\boldsymbol{x})}{\det q(\boldsymbol{x})} \tag{1.79}$$

$$V[\Phi] = \int_{\Sigma_t} \mathrm{d}\mu(x)\; N_\perp(\boldsymbol{x}) f(\boldsymbol{x})\, \Phi(\boldsymbol{x})(-\Delta + m^2 + \zeta R)\Phi(\boldsymbol{x}) \tag{1.80}$$

where $\mathrm{d}\mu(\boldsymbol{x}) = \sqrt{q}(\boldsymbol{x})\mathrm{d}^3\boldsymbol{x}$ is the covariant measure on Σ_t; ζ is the coupling parameter to the Ricci scalar curvature R, $\Delta = -\partial_i(N_\perp\sqrt{q}q^{ij}\partial_j)$ is the Laplace operator induced

on Σ_t, and we assume that Δ acting on $\phi(\boldsymbol{x})$ can only yields real eigenvalues, which that the self-adjointness of Φ passes on to $\mathcal{V}[\Phi]$. On the other hand,

$$H_{\parallel} = \int_{\Sigma_t} \mathrm{d}\mu(\boldsymbol{x})\, f(\boldsymbol{x}) N^i(\boldsymbol{x}) \nabla_i \Phi(\boldsymbol{x}) \Pi(\boldsymbol{x}) \tag{1.81}$$

contains the off-diagonal part, and it is not particularly important because the Hamiltonian can be diagonalized by a local coordinate transformation, such that the off-diagonal part can always be eliminated. What always remains, therefore, is the diagonal part of H.

As a result, to conclude our analysis on the condition for self-adjointness of H, we are required to consider only the kinetic operator $A[\Pi]$, determining whether or not H admits self-adjoint extensions. To this end, we will show that for a general $\mathcal{K}^{(2)}$ that satisfies the Schrodinger equation, the Hamiltonian is a complex functional of ϕ in a dynamical spacetime, and it cannot admit any self-adjoint extension, even though they exist for Π. To see this, for a Gaussian state $\Psi_t[\phi]$ in a dynamical spacetimes, the bikernal functional $\mathcal{K}^{(2)}$ must satisfy:

$$\begin{aligned} &-\mathrm{i}\partial_t \mathcal{K}_2^{(2)} \\ &= \int_{\Sigma_t} \mathrm{d}\mu(\boldsymbol{x})\, f(\boldsymbol{x}) \left[\frac{N_\perp}{4} \left(\frac{\Pi(\boldsymbol{x}) \mathcal{K}_2[\phi]}{\sqrt{\det q}(\boldsymbol{x})} \right)^2 - N^i \nabla_i \Phi(\boldsymbol{x}) \frac{\Pi(\boldsymbol{x}) \mathcal{K}^{(2)}[\phi]}{\sqrt{\det q}(\boldsymbol{x})} \right] + V[\Phi] \end{aligned} \tag{1.82}$$

where the bikernel functional also determines the evolution of the normalization factor $\mathcal{N}_t$:

$$\mathrm{i}\partial_t \ln \mathcal{N}_t = -\frac{1}{2} \int_{\Sigma_t} \mathrm{d}\mu(\boldsymbol{x}) f(\boldsymbol{x}) N_\perp \frac{\Pi^2(\boldsymbol{x}) \mathcal{K}^{(2)}[\phi]}{\det q(\boldsymbol{x})} \,. \tag{1.83}$$

Since the spacetime is dynamical, the Hamilton operator is time-dependent and thus cannot admit a self-adjoint extension. We can show this by the proof of contradiction. Recall that the criterion for the self-adjoint domain of $\mathcal{H}$ is given by $\mathrm{Im}\, K_2(\boldsymbol{x}, \boldsymbol{x}; t) = 0\ \forall \boldsymbol{x} \in \Sigma_t$. Now consider the general solution to (1.83) is

$$|\mathcal{N}_t|^2 = |\mathcal{N}_0|^2 \exp\left[\mathrm{i} \int_{t_0}^{t} \mathrm{d}\tau \int_{\Sigma_t} \mathrm{d}\mu(\boldsymbol{x})\, \mathrm{Im} K_2(\boldsymbol{x}, \boldsymbol{x}; t) \right] \tag{1.84}$$

where $\mathcal{N}_0$ is the integration constant determined at the initial time t_0. Assume $\mathcal{H}$ admits a self-adjoint extension so that $\mathrm{Im}\, K_2(\boldsymbol{x}, \boldsymbol{x}; t) = 0$ holds for all $\boldsymbol{x} \in \Sigma_t$ at all time t, such that $|\mathcal{N}_t|^2 = |\mathcal{N}_0|^2$ for all t. Since $\mathcal{H}$ admits a self-adjoint extension, it ensures norm conservation:

$$\partial_t \|\Psi_t\|^2 = |\mathcal{N}_0|^2 \int_U \mathscr{D}\phi\, \partial_t \,\mathrm{Re}\mathcal{K}^{(2)}[\phi]\, \exp\left(-\mathrm{Re}\,\mathcal{K}^{(2)}[\phi]\right) \equiv 0 \tag{1.85}$$

This identity is true only for all $\boldsymbol{x} \in \Sigma_t$ at all time if and only if $\partial_t \mathrm{Re}\mathcal{K}_2^{(2)}[\phi]$ for $\mathrm{Re}\mathcal{K}^{(2)}[\phi] \neq 0$, or otherwise (1.85) is false. However, the requirement that $\partial_t \mathrm{Re}\mathcal{K}_2^{(2)}[\phi] = 0$ and $\mathrm{Im}K_2(\boldsymbol{x}, \boldsymbol{x}; t) = 0$ for all $\boldsymbol{x} \in \Sigma_t$ and $t \in I$ is possible only if $\mathcal{K}^{(2)}[\phi]$ is time independent. This is possible only if the Schrödinger equation is time-independent, which reduces to the time-independent Schrödinger equation $H[\Pi, \Phi]\Psi[\phi] = E\,\Psi[\phi]$, where $E \in \mathbb{R}$ [21], which is equivalent to saying that all terms in (1.82) and (1.83) are time independent, including the spacetime metric. This, however, indicate that the spacetimes must be static in order to meet the criterion that $\partial_t \mathrm{Re}\mathcal{K}_2^{(2)}[\phi] = 0$ and $\mathrm{Im}K_2(\boldsymbol{x}, \boldsymbol{x}; t) = 0$ for all $\boldsymbol{x} \in \Sigma_t$ for all $t \in I$. As a result, we conclude that it is, by consistency, impossible to meet the criterion for the Hamilton operator to admit a self-adjoint extension, provided that the spacetime is dynamical. On the contrary, this also proves that the Hamilton operator can admit infinitely many self-adjoint extensions, but only in static spacetime like the Minkowski spacetime.

At last, we provide an equivalent interpretation of our result from the viewpoint that the lack of self-adjoint extension for the Hamiltonian operator in dynamic spacetime manifests as having non-vanishing probability flux leaving the given field configuration space U through its boundaries ∂U. This can be seen from reformulating the time derivative of the norm in terms of the Schrodinger equation

$$\partial_t \|\Psi_t\|^2 = i \int_U \mathscr{D}\phi \left[(\Psi_t^*[\phi] H^\dagger)\Psi_t[\phi] - \Psi_t^*[\phi](H\Psi_t[\phi])\right]. \tag{1.86}$$

The time derivative is assumed to commute with the functional integral because the neighborhood U is imposed only by the physical cut-off condition such that ∂U is

time-independent. Insert the Hamiltonian, and the time derivative of the norm can be expressed in terms of three different contributions

$$\partial_t \|\Psi_t\|^2 = \int_U \mathscr{D}\phi \, \Big(\operatorname{div} j_t[\phi] + s_t[\phi] + b_t[\phi] \Big) \tag{1.87}$$

where $s_t[\phi] = \operatorname{Im} V[\Phi] = 0$ is the source terms that represent probability sinks, which is zero for a free theory because the potential operator $V[\Phi]$ is self-adjoint. The term $b[\phi]$ is the off-diagonal term that is captured by the imaginary part of $H_{\|}$. Again, this contribution is ignored for now without any loss of generality to the implications of our results because the Hamiltonian can always be diagonalized by a local coordinate transformation. The most important term is the first term that characterizes the divergence of the probability density current $j_t[\phi]$:

$$\operatorname{div} j_t[\phi] \equiv \int_{\Sigma_t} \mathrm{d}\mu(\boldsymbol{x}) \, f(\boldsymbol{x}) \, \frac{N}{h(\boldsymbol{x})} \frac{\delta j_{t,\boldsymbol{x}}[\phi]}{\delta \phi(x)} \tag{1.88}$$

$$j_{t,\boldsymbol{x}}[\phi] \equiv \frac{1}{i} \left(\Psi_t[\phi] \frac{\delta}{\delta \phi(x)} \Psi_t^*[\phi] - \Psi_t^*[\phi] \frac{\delta}{\delta \phi(x)} \Psi_t[\phi] \right) \tag{1.89}$$

where $j_{t,\boldsymbol{x}}[\phi]$ is the local probability density current in the instantaneous configuration space $U(\boldsymbol{x})$. This particular expression reveals that

$$\partial_t \|\Psi_t\|^2 = \int_{\Sigma_t} \mathrm{d}\mu(\boldsymbol{x}) \, f(\boldsymbol{x}) \int_{U \setminus U(\boldsymbol{x})} \mathscr{D}\phi \;\; j_{t,\boldsymbol{x}}[\phi] \Big|_{\partial U(\boldsymbol{x})} , \tag{1.90}$$

where we have again reabsorbed all the time-dependent factors into $f(\boldsymbol{x})$ for clarity The expression indicates that the time derivative of the norm is given by the probability density current penetrating through the boundary $\partial U(\boldsymbol{x})$ contributed from all $\boldsymbol{x} \in \Sigma_t$. This is consistent with our previous finding that the Hamiltonian admits a self-adjoint extension if the Gaussian wave functional is characterized by a purely real bi-local kernel function $\operatorname{Im} K_2(\boldsymbol{x}, \boldsymbol{y}; t)$, which is only possible if the wave functional satisfies the time-independent Schrodinger equation. As a result, in dynamical spacetimes, the Hamiltonian does not admit a self-adjoint operator, and this is quantitatively described by the amount of probability density current leaving the instantaneous field configuration U through ∂U.

It should be noted that this condition also imposes strict conditions on the imaginary part of the bi-local kernel function in dynamic spacetime. In the absence of ghosts, the total probability cannot be increasing but only decreasing. In other words, the probability density current is only allowed to leave the field configuration space but not enter it from outside. This implies that any theory containing only physical degrees of freedom must impose certain conditions on the imaginary part of the bi-local kernel function.

1.4 Contractive Evolution

So far we have discussed the spectrum of $\mathcal{H}$ that generates the time-evolution. We learned that $\mathcal{H}$ is not necessarily self-adjoint. In this section, we will examine the consequences of this result and its implications for the associated evolution group following the treatment in [36–39]. This will allow us to generalize the Stone's correspondence in quantum mechanics, where a self-adjoint Hamilton operator corresponds to a unitary evolution one-parameter time evolution group, into a functional version in quantum field theory.

Let us consider a one-parameter family of evolution operators $\{\mathcal{E}(t,t_0)\}_{t\in I}$ acting on $L^2(\Gamma(\mathcal{C}_{t_0}),\mathscr{D}\phi)$, where $\mathcal{C}_{t_0}$ denotes the configuration space at the initial time $t_0 \in I$. This family of map satisfies $\mathcal{E}(t_0,t_0) = \mathrm{id}_{\Gamma^*(\mathcal{C}_{t_0})}$ and $\mathcal{E}(t,s)\mathcal{E}(s,t_0) = \mathcal{E}(t,t_0)$ for all $t,s \in I$, and the map $t \mapsto \mathcal{E}(t,t_0)\Psi_{\text{in}}$ is continuous for each normalizable initial wave functional $\Psi_{\text{in}} \in L^2(\Gamma(\mathcal{C}_{t_0}),\mathscr{D}\phi)$. In what follow, we restrict to a special family of evolution operators, known as the contractive evolution operator, which satisfy the condition

$$\inf\Big\{C \geq 0 : \mathbb{E}^{1/2}\left(\mathrm{id}_{\Gamma^*(\mathcal{C}_t)}\,;\,\mathcal{E}(t,t_0)\Psi_{\text{in}}\right) \leq C\,,\ \forall\,\Psi_{\text{in}} \in L^2(\Gamma(\mathcal{C}_{t_0}),\mathscr{D}\phi)\Big\} \leq 1\,,$$

or using the supremum $\sup_{\Psi\neq 0}(\|\mathcal{E}(t,t_0)\Psi\|/\|\Psi\|) \leq 1, \forall\,\Psi \in L^2(\Gamma(\mathcal{C}_{t_0}),\mathscr{D}\phi)$. Contractive evolution families arise naturally in effective field theories and provide a necessary generalization of the correspondence between unitary evolution groups and self-adjoint generators of time translations.

In the case of contracting evolution semigroups, which includes unitary representations of evolution groups, we can obtain the generator for $\mathcal{E}(t+\delta t,t)$ with $[t,t+\delta t] \subset I$ as follows. Let us consider a general generator for infinitesimal time translation,

$$T_t(\delta t) \equiv \frac{\mathrm{id}_{\Gamma^*(\mathcal{C}_t)} - \mathcal{E}(t+\delta t,t)}{\delta t}\,, \tag{1.91}$$

and introduce the domain

$$D(T_t) \equiv \{\Psi_t \in L^2(\Gamma(\mathcal{C}_t),\mathscr{D}\phi) : \lim_{\delta_t\to 0^+} T_t(\delta t)\Psi_t \text{ exists}\} \tag{1.92}$$

so that the infinitesimal generator T_t is defined by $T_t\Psi_t \equiv \lim_{\delta t\to 0^+} T_t(\delta t)\Psi_t$ for all $\Psi_t \in D(T_t)$. Then T_t generates the time evolution $\mathcal{E}(t,t_0)$ in the form of the time-ordered exponential

$$\mathcal{E}(t,t_0) \;=\; \mathcal{T}\exp\left(-\int_{t_0}^{t} \mathrm{d}\tau\, T_\tau(\Phi,\Pi)\right). \tag{1.93}$$

where T_τ is a functional of the canonical fields Φ and its conjugate momentum operator Π. We first show that $D(T_t)$ is dense in $L^2(\Gamma(\mathcal{C}_t),\mathscr{D}\phi)$. For any $\Psi_t \in L^2(\Gamma(\mathcal{C}_t),\mathscr{D}\phi)$ and set

$$\Psi^{(s)}(\phi) \equiv \int_{[0,s]} \mathrm{d}\tau\, \mathcal{E}(t+\tau,t)\Psi_t(\phi) \tag{1.94}$$

for $[t,t+s]\subset I$. For any $r>0$ with $(t+s+r)\in I$, consider $\mathcal{E}(t+r,t)\,\Psi^{(s)}$, and define $\Psi_{t+\tau+r} = \mathcal{E}(t+r,t)\,\Psi_{t+\tau}$,

$$\begin{aligned} T_t(r)\Psi^{(s)} &= -\frac{1}{r}\int_0^s \mathrm{d}\tau\,(\Psi_{t+\tau+r}-\Psi_{t+\tau}) \\ &= -\frac{1}{r}\left(\int_s^{r+s}\mathrm{d}\tau\,\Psi_{t+\tau} - \int_0^s \mathrm{d}\tau\,\Psi_{t+\tau}\right) \end{aligned} \tag{1.95}$$

Taking the limit $r\to 0$

$$\lim_{r\to 0} T_t(r)\Psi^{(s)} = \left(\mathrm{id}_{\Gamma^*(\mathcal{C}_t)} - \mathcal{E}(s+t,t)\right)\Psi_t \tag{1.96}$$

So for each $\Psi_t \in L^2(\Gamma(\mathcal{C}_t),\mathscr{D}\phi)$ and for each admissible $s>0$, $\Psi^{(s)}\in D(T_t)$. Since the sequence converges by $\{s^{-1}\Psi^{(s)}\}_{s\in I}\to\Psi_t$ at the limit $s\to 0$, and lies in the domain $D(T_t)$, $D(T_t)$ is dense in $L^2(\Gamma(\mathcal{C}_t),\mathscr{D}\phi)$. It is worth stressing that the evolution equation is required in this derivation since, in general, the dynamical content of the theory is given by a one-parameter family of time-ordered exponentials which need not form a semi-group. However, if $\Psi_t\in D(T_t)$, then $T_{s+t}\,\mathcal{E}(s+t,t)\,\Psi_t = \mathcal{E}(s+t,t)\,T_t\,\Psi_t$ so that $\mathcal{E}(s+t,t) : D(T_t)\to D(T_{s+t})$ and

$$\partial_s\Psi_{s+t} = -T_{s+t}\Psi_{s+t} = -(T_t\Psi_t)_{s+t} \tag{1.97}$$

We can use this to show that T_t is also closed. Let $\{\Psi_t^n\}_{n\in\mathbb{N}}$ be a sequence of wave functionals with $\Psi_t^n \in D(T_t)$ for all $n \in \mathbb{N}$, which coverages by $\{\Psi_t^n\}_{n\in\mathbb{N}} \to \Psi_t \in L^2(\Gamma(\mathcal{C}_t), \mathscr{D}\phi)$ and $T_t\Psi_t^n \to \Xi_t$. Then

$$\begin{aligned} T_t(r)\Psi_t &= \lim_{n\to\infty} \frac{1}{r}\left(\Psi_t^{(n)} - \mathcal{E}(r+t,t)\Psi_t^{(n)}\right) \\ &= \lim_{n\to\infty} \frac{1}{r}\int_0^r \mathrm{d}t\ \mathcal{E}(r+t,t)T_t\Psi_t^{(n)} \end{aligned} \tag{1.98}$$

where we have considered the evolution equation $\mathcal{E}(r+t,t)\Psi_t^n = \Psi_t - (T_t\Psi_t^n)^{(r)}$ together with (1.97). Thus,

$$\lim_{r\to 0} T_t(r)\Psi_t = \lim_{r\to 0}\frac{1}{r}\int_0^r T_t\Xi_t \mathrm{d}t = \Xi_t \tag{1.99}$$

Therefore $\Psi_t \in D(T_t)$ and $T_t\Psi_t = \Xi_t$. Altogether, this shows that T_t is closed and densely defined, This allows to perform a generalized spectral analysis, which is essential to relax the strict correspondence of Stone's theorem between self-adjointness and unitarity. Now we turn to the necessary properties attributed to the generator.

1.4.1 Accretive Generators

While the contraction property replaces unitarity, it remains to investigate what supplants properties relate to self-adjointness and the infinitesimal generators. Let $E_s \in \mathbb{C}$ lie in the spectrum of the infinitesimal generator T_s and $s \in I = (0,\infty)$. Introduce a specific infinitesimal generator $\gamma_s \equiv -\partial_s$ and define $G_s(t) \equiv \exp(-t\gamma_s)$. Then the Laplace transform $\mathcal{L}$ of $G_s(t)$ formally gives

$$\mathcal{L}[G_s(t)](E_s) = \int_0^\infty \mathrm{d}t\ e^{-t\gamma_s}e^{-tE_s} = -\frac{1}{E_s\,\mathrm{id}_{D(T_s)} + \gamma_s}. \tag{1.100}$$

Suppose $\mathrm{Re}\,E_s > 0$ and $\Psi_s = \mathcal{E}(s,0)\Psi_0$, and since $\|G_s(t)\| \leq 1$ by assumption, the operator

$$\mathcal{S}\Psi_s \equiv \mathcal{L}[G_s(t)\Psi_s](E_s) = \int_0^\infty \mathrm{d}t\ e^{-tE_s}(e^{t\gamma_s}\Psi_s) \tag{1.101}$$

is a bounded linear operator of norm less than or equal to $(\mathrm{Re}\, E_s)^{-1}$. For positive δt,

$$\begin{aligned}\gamma_s(\delta t)\,\mathcal{S}\Psi_s &= \frac{1}{\delta t}\Big(\mathcal{L}\big[\,(G_s(t)-G_s(t+\delta t))\,\Psi_s\big](E_s)\Big)\\ &= -\frac{1}{\delta t}\int_0^\infty \mathrm{d}t\; e^{-tE_s}\left(e^{-(t+\delta t)\gamma_s}-e^{-t\gamma_s}\right)\Psi_s \qquad (1.102)\\ &= \left(\frac{1-\mathrm{e}^{\delta t E_s}}{\delta t}\right)\mathcal{L}[\Psi_t](E_s)+\frac{\mathrm{e}^{\delta t E_s}}{\delta t}\int_0^{\delta t}\mathrm{e}^{tE_s}\,\Psi_t\ ,\end{aligned}$$

where the third equality holds after shifting $t\to t-\delta t$ in the second Laplace transform, and $\Psi_t\equiv G_s(t)\Psi_s$. In the limit $\delta t\to 0$,

$$\lim_{\delta t\to 0}\gamma_s(\delta t)\,\mathcal{S}\Psi_s=\Psi_s-E_s\mathcal{S}\Psi_s \qquad (1.103)$$

Hence, $\mathcal{S}\Psi_s\in D(\gamma_s)$ and $\gamma_s\mathcal{S}\Psi_s=\Psi_s-E_s\mathcal{S}\Psi_s$, which imples $(E_s\mathrm{id}_{D(T_s)}+\gamma_s)\mathcal{S}\Psi_s=\Psi_s$. Furthermore, for $\Psi_s\in D(T_s)$, we have $\gamma_s\mathcal{S}\Psi_s=\mathcal{S}\gamma_s\Psi_s$ such that $[\gamma_s,\mathcal{S}]=0$ on $D(T_t)$ because

$$\begin{aligned}\gamma_s\mathcal{S}\Psi_s &= \gamma_s\int_0^\infty \mathrm{d}t\; e^{-E_S t}e^{-t\gamma_s}\Psi_s\\ &= \int_0^\infty \mathrm{d}t\; e^{-E_S t}\gamma_s e^{-t\gamma_s}\Psi_s=\int_0^\infty \mathrm{d}t\; e^{-E_S t}e^{-t\gamma_s}\gamma_s\Psi_s \qquad (1.104)\end{aligned}$$

where we have considered the fact that $\mathrm{e}^{-\delta t E_s}\Psi_t$ and $\gamma_s\mathrm{e}^{-\delta t E_s}\Psi_t$ are integrable by the condition on the spectrum of γ_s, and the fact that γ_s is closed. As a consequence, for $\Psi_s\in D(T_s)$, the following holds:

$$\mathcal{S}(E_s\mathrm{id}_{D(T_s)}+\gamma_s)\Psi_s=(E_s\mathrm{id}_{D(T_s)}+\gamma_s)\mathcal{S}\Psi_s=\Psi_s \qquad (1.105)$$

which implies that $\mathcal{S}=(E_s\mathrm{id}_{D(T_s)}+\gamma_s)^{-1}$ holds in the strong sense.

Apart from the restrictive adaptation needed to include time-ordered exponentials as evolution operators, the above reasoning follows the proof of the necessity part of the Hille-Yosida theorem [19]. The spectral properties of T_s are also sufficient to guarantee that T_s generates a contracting family of evolution operators. Let E_s be real positive and define on $D(T_s)$: $\vartheta_{E_s}\equiv E_s(\,\mathrm{id}_{D(T_s)}-E_s(E_s\mathrm{id}_{D(T_s)}+\gamma_s)^{-1}\,)$. The derivation proceeds in three steps: first, we will prove that ϑ_{E_s} approximates γ_s by

$\vartheta_{E_s}\Psi_s \to \gamma_s\Psi_s$ that as $E_s \to \infty$ for any wave functional in $D(T_s)$. Then we will show that the semigroups $\exp(-t\vartheta_{E_s})$ are contractive; Finally, we construct $G_s(t)$ as the strong limit of these semigroups.

For $\Psi_s = \mathcal{E}(s,0)\Psi_0$ in $D(T_s)$, we have

$$\vartheta_{E_s}\Psi_s = \frac{E_s}{(E_s \mathrm{id}_{D(T_s)} + \gamma_s)}\gamma_s\Psi_s \tag{1.106}$$

Moreover, from the necessity part discussed above, $\|(E_s\,\mathrm{id}_{D(T_s)} + \gamma_s)^{-1}\| \leq E_s^{-1}$ for all real positive E_s, so

$$\begin{aligned} -E_s^{-1}\vartheta_{E_s}\Psi_s &= \frac{E_s}{E_s\,\mathrm{id}_{D(T_s)} + \gamma_s}\Psi_s - \Psi_s \\ &= -\frac{1}{E_s\,\mathrm{id}_{D(T_s)} + \gamma_s}\gamma_s\Psi_s \overset{E_s\to\infty}{\longrightarrow} 0\,, \end{aligned} \tag{1.107}$$

since $\|E_s^{-1}\vartheta_{E_s}\Psi_s\| = \|(E_s\,\mathrm{id}_{D(T_s)}+\gamma_s)^{-1}\gamma_s\Psi_s\| \leq E_s^{-1}\|\gamma_s\Psi_s\|$ by the above bound. It follows that the family $\{(E_s\,\mathrm{id}_{D(T_s)} + \gamma_s)^{-1} : E_s > 0\}$ is uniformly bounded in norm, and since $D(T_s)$ is dense, $(E_s\,\mathrm{id}_{D(T_s)} + \gamma_s)^{-1}\Psi_s \to \Psi_s$ for all $\Psi_s \in L^2(\Gamma(\mathcal{C}_s), \mathscr{D}\phi)$. As a result,

$$\vartheta_{E_s}\Psi_s = \frac{E_s}{E_s\,\mathrm{id}_{D(T_s)} + \gamma_s}\gamma_s\Psi_s \overset{E_s\to\infty}{\longrightarrow} \gamma_s\Psi_s\,. \tag{1.108}$$

Since ϑ_{E_s} is bounded, the associated semigroups can be defined by power series. Since

$$\begin{aligned} \left\|e^{-t\vartheta_{E_s}}\right\| &= \left\| e^{-tE_s}e^{+tE_s^2(E_s\mathrm{id}_{D(T_s)}+\gamma_s)^{-1}} \right\| \\ &\leq e^{-tE_s}\sum_{n\in\mathbb{N}}\frac{(tE_s^2)^n}{n!}\left\|(E_s\,\mathrm{id}_{D(T_s)} + \gamma_s)^{-1}\right\|^n \leq 1\,, \end{aligned}$$

where the first equality follows from the definition of ϑ_{E_s}, the second follows from the triangle inequality and the last from the bound on $\|(E_s\,\mathrm{id}_{D(T_s)} + \gamma_s)^{-1}\|$ due to contractivity. Let $E_s, {E_s}', t$ be real positive, and $\Psi_s \in D(T_s)$, then

$$\left(e^{-t\vartheta_{E_s}} - e^{-t\vartheta({E_s}')}\right)\Psi_s = \int_0^t \mathrm{d}x\, \frac{\mathrm{d}}{\mathrm{d}x}\left(e^{-x\vartheta_{E_s}} e^{-(t-x)\vartheta({E_s}')}\Psi_s\right) .$$

Using the fact that $\{\vartheta_{E_s}\}_{E_s>0}$ is a commuting family of infinitesimal generators, such that $e^{-t\vartheta_{E_s}}$ commutes with $e^{-(t-x)\vartheta_{E_s'}}$

$$\begin{aligned}\left\|\left(e^{-t\vartheta_{E_s}} - e^{-t\vartheta_{{E_s}'}}\right)\Psi_s\right\| &\leq \int_0^t \mathrm{d}x\, \left\|e^{-x\vartheta_{E_s}} e^{-(t-x)\vartheta_{{E_s}'}}\right\| \left\|\vartheta_{{E_s}'}\Psi_s - \vartheta_{E_s}\Psi_s\right\| \\ &\leq t\left\|\vartheta_{{E_s}'}\Psi_s - \vartheta_{E_s}\Psi_s\right\| .\end{aligned}$$

The last inequality follows from the contraction property of the semigroups generated by ϑ_{E_s}. Since we have already shown that $\vartheta_{E_s}\Psi_s$ converges to $\gamma_s\Psi_s$ as $E_s \to \infty$, it follows that $(e^{-t\vartheta_{E_s}}\Psi_s)_{E_s>0}$ is a Cauchy sequence in this limit for any real positive t and $\Psi_s \in D(T_s)$. Let us therefore define $G_s(t)\Psi_s \equiv \lim_{E_s\to\infty} e^{-t\vartheta_{E_s}}\Psi_s$, since the properties of contraction semigroups are preserved under the strong limit, $G_s(t)$ constitutes a semigroup of contracting evolution operators. The above inequality shows that $G_s(t)$ is a strongly continuous contraction semigroup.

Let $\tilde{\gamma}_s$ denote the infinitesimal generator of $G_s(t)$, and it is necessary to show that $\tilde{\gamma}_s$ equal to γ_s. For all $t > 0$ and $\Psi_s \in D(T_s)$,

$$\Psi_s - e^{-t\vartheta_{E_s}}\Psi_s = \int_0^t \mathrm{d}x\, e^{-x\vartheta_{E_s}}\vartheta_{E_s}\Psi_s ,$$

and therefore

$$\Psi_s - G_s(t)\Psi_s = \int_0^t \mathrm{d}x\, G_s(x)\gamma_s\Psi_s$$

since $\vartheta_{E_s}\Psi_s$ converges to $\gamma_s\Psi_s$ in the limit $E_s \to \infty$. Now, in the limit $t \to 0^+$, the left-hand side converges to $\tilde{\gamma}_s\Psi_s$ and the right-hand side to $\gamma_s\Psi_s$. Thus $\tilde{\gamma}_s\Psi_s$ converges to $\gamma_s\Psi_s$. Therefore $D(\tilde{\gamma}_s) \supset D(\gamma_s)$ and $\tilde{\gamma}_s$ restricted to the domain $D(\gamma_s)$ agrees with γ_s. It remains to show that both domains coincide. For real positive E_s,

the inverse of $(E_s\mathrm{id}_{D(T_s)} + \tilde{\gamma}_s)$ exists by the necessity part of the statement shown above, and the inverse of $(E_s\mathrm{id}_{D(T_s)} + \gamma_s)$ exists by hypothesis. Hence, $(E_s\mathrm{id}_{D(T_s)} + \tilde{\gamma}_s)D(\tilde{\gamma}_s) = L^2(\Gamma(\mathcal{C}_s), \mathscr{D}\phi)$, and, as well, $(E_s\mathrm{id}_{D(T_s)} + \gamma_s)D(\gamma_s) = L^2(\Gamma(\mathcal{C}_s), \mathscr{D}\phi)$, so indeed $D(\tilde{\gamma}_s) = D(\gamma_s)$.

The above derivation requires constructing the resolvent of the infinitesimal generator of the evolution operator in order to establish the spectral properties that are necessary and sufficient to generate a one-parameter family of contracting evolution operators. If Ψ_0 lies in the domain of T_τ for $\tau \in I := [0, t]$, then the contraction property implies, within $\mathrm{Dom}(T_\tau)$

$$-\partial_t \|\Psi_t\| = \mathbb{E}(-T_t^*; \Psi_t) + \mathbb{E}(-T_t; \Psi_t) \tag{1.109}$$

Thus, the contraction property requires that $\mathrm{Re}(\mathbb{E}(-T_t; \Psi_t))$ be semi-positive definite. Such a densely defined infinitesimal generator is called accretive.

Identifying the infinitesimal generator with the Hamilton operator $\mathcal{H}$ links this analysis to the previous discussion. Although the spectrum is complex-valued, if the spectrum admits a suitable sign in the imaginary part, the evolution can be described by evolution operators that keep the probabilistic feature of the theory intact. In the spirit of Stone's theorem, we conclude that one-parameter families of evolution operators in general admit contractive representations generated by accretive operators. The correspondence between unitarity and self-adjointness therefore appears as the special cases.

1.4.2 Initial Data

Statements in the previous section concerning the dynamical content of the theory were derived under the assumption of the time-evolved data as input. Consequently, these statements do not extend to wave functionals on Cauchy hypersurfaces. The purpose of this section is to bridge this gap by explicitly formulating the initial-value problem.

Let I be a half-open, left-closed interval of the extended real numbers, and denote its minimum element by $t_0 \equiv \partial I = 0$. Consider a small subset of the interval $J \equiv [\partial I, \delta t] \subset I$, where $\delta t > 0$ is arbitrarily small, so that the quantum state

$\Psi_\tau \equiv \mathcal{E}(\tau,0)\Psi_0$ is continuous on J and smooth on the interior of J. Then the integrated evolution equation becomes

$$\Psi_{\delta t} = \Psi_0 - \int_J \mathrm{d}s\; T_s \Psi_s \;. \tag{1.110}$$

By the mean value theorem for definite integrals, there exists a real number $m \in (0, \delta t)$ in the interior of J such that $\Psi_{\delta t} = \Psi_0 - \delta t\, T_m \Psi_m$. We can write $m = \alpha \delta t$ with $\alpha \in (0,1)$. Since m is a positive fraction of δt, it follows that $\Psi_{\delta t} = \Psi_0 - \delta t\, T_{0^+}\Psi_0 + \mathcal{O}(\alpha)$, where 0^+ denotes the interior points of J that are arbitrary close to the minimum element t_0. The remaining term $\mathcal{O}(\alpha)$ represents the order of approximation. This can be seen explicitly by iterating the integrated evolution equation:

$$\Psi_{\delta t} = \Psi_0 - \delta t\, T_{m_1}\Psi_0 + m_1 \delta t\, T_{m_1} T_{m_2}\Psi_0 + O(\alpha^2)\,, \tag{1.111}$$

where the second-order approximation is associated with the products $\alpha_1\alpha_2$ of the parameters $m_a = \alpha_a \delta t$ for $a \in \mathbb{N}$, with $m_1 > m_2$ in $(0, \delta t)$ guaranteed by the mean value theorem. In the limit $\alpha_1 \to 0^+$, we find $\Psi_{\delta t} = \Psi_0 - \delta t\, T_{0^+}\Psi_0$. Since the sequence $\{\alpha_a\}_{a\in\mathbb{N}}$ is strictly decreasing by the mean value theorem, the definition of the time-ordered evolution operator ensures that the above result holds to arbitrary precision. Thus the infinitesimal evolution operator $(\mathrm{id}_{D(T_{0^+})} - \delta t\, T_{0^+})$ is, to linear order of δt, a member of a one-parameter family of strongly continuous semigroups: the existence of an identity is obvious, the composition law holds at linear order in δt and continuity is given by hypothesis.

1.5 Applications in Friedmann Spacetimes

In this section, we will apply our previous analysis to a cosmological setting in combination with numerical simulations of quantum fluctuations[4]. The accompanying numerical analysis demonstrates how quantum fluctuations interact with gravitational fields and amplify in their magnitude, then eventually identify a spacetime region where the semiclassical framework inevitably breaks down. We consider two particular setups: a radiation-dominated universe, which is commonly used in modeling the early universe or as an approximation to gravitational collapse within a massive star during black hole formation. On the other hand, the de Sitter spacetimes approximate inflation during the slow-roll approximation.

Let us consider a conformally flat Friedmann-Lemaitre-Robertson-Walker spacetime with the following line element: $\mathrm{d}s^2 = a^2(\eta)\ (-\mathrm{d}\eta^2 + \mathrm{d}\mathbb{E})$, where $\mathrm{d}\mathbb{E} = \delta_{ij}\,\mathrm{d}x^i\mathrm{d}x^i$ denotes the line element of the three-dimensional Euclidean space, and $a(\eta)$ is the scale factor as a function of conformal time η. In this setup, we consider the ground state Gaussian wave functional Ψ_t that satisfies the Schrodinger equation, with the corresponding probability density functional given by

$$\rho_\eta[\phi] \equiv |\Psi_\eta[\phi]|^2 = |\mathcal{N}_\eta|^2 \exp\left(-\mathrm{Re}\mathcal{K}_\eta^{(2)}[\phi]\right) \tag{1.112}$$

where $\mathcal{K}_\eta^{(2)}[\phi] = \int_{\Sigma_t} \mathrm{d}\mu(\boldsymbol{x})\ \mathrm{d}\mu(\boldsymbol{y})\ \phi(\boldsymbol{x})\ K_2(\boldsymbol{x},\boldsymbol{y};\eta)\ \phi(\boldsymbol{y})$ fully determines the Gaussian statistics of the probability density distribution $\rho_\eta[\phi]$ with the following mean and variance:

$$\langle\Phi(\boldsymbol{x})\rangle = \int_U \mathscr{D}\phi\ \phi(\boldsymbol{k})\,\rho_\eta[\phi] = 0 \tag{1.113}$$

$$\langle\Phi(\boldsymbol{x})\Phi(\boldsymbol{y})\rangle = \int_U \mathscr{D}\phi\ \phi(\boldsymbol{x})\phi(\boldsymbol{y})\,\rho_\eta[\phi] = \mathrm{Re}\,K_2^{-1}(\boldsymbol{x},\boldsymbol{y};t) \tag{1.114}$$

As a quick reminder $\langle\ \cdot\ \rangle \equiv \mathbb{E}(\mathcal{O},\Psi_\eta)$ is the expectation value of the observables operator $\mathcal{O}$ with respect to the wave functional Ψ_η; the variance is obtained from the usual approach using the generation functionals [21]. Due to spatial symmetries of

[4]The source codes and documentations for the numerical simulations are available at `https://github.com/khchoi-lmu-physik/grf_qftcs`

the Friedmann background, it is convenient to work in momentum space for various practical reasons that will be clear soon. The two-point correlation function of the Gaussian state can be computed explicitly by recasting $\mathcal{K}^{(2)}[\phi]$ in terms of its Fourier modes:

$$\mathcal{K}^{(2)}_{\eta}[\phi] = \int_{\mathbb{K}}\int_{\mathbb{P}} \frac{\mathrm{d}^3k}{(2\pi)^3}\frac{\mathrm{d}^3p}{(2\pi)^3}\; \phi(\boldsymbol{k})\, \sigma^{-2}(k;\eta)\delta^3(\boldsymbol{k}-\boldsymbol{p})\phi(-\boldsymbol{p})\,, \tag{1.115}$$

such that the variance of the Gaussian state in the momentum space is $\langle\Phi(\boldsymbol{k})\Phi(-\boldsymbol{p})\rangle = \sigma^2(k;\eta)\,\delta^3(\boldsymbol{k}-\boldsymbol{p})$ where

$$\sigma^2(k;\eta) = \det q(\eta)\; \mathrm{Re}\tilde{K}_2^{-1}(k;\eta)\,. \tag{1.116}$$

and the kernel function $\tilde{K}_2(k;\eta) = \int_{\Sigma_t}\mathrm{d}^3x\, e^{-\mathrm{i}\boldsymbol{k}(\boldsymbol{x}-\boldsymbol{y})}K^{(2)}(\boldsymbol{x},\boldsymbol{y};\eta)$ satisfies the Schrodinger equation and can be identify with the mode function $u(k,\eta)$ that solves the Klein-Gordon equations [20, 23]:

$$\tilde{K}_2(k,\eta) = -\frac{\mathrm{i}\,\partial_\eta \ln u^*(k,\eta)}{N_\perp\sqrt{\det q(\eta)}}\,, \tag{1.117}$$

where the mode function $u(k,\eta)$ is normalized with respect to the Wronski determinant [20, 40]

$$u(k,\eta)\partial_\eta u^*(k,\eta) - u^*(k,\eta)\partial_\eta u(k,\eta) = \frac{\mathrm{i}\,N_\perp}{\sqrt{\det q(\eta)}} \tag{1.118}$$

As a result, one can recast the variance of the Gaussian state as a function of the mode function, $\sigma^2(k,\eta) = |u(k,\eta)|^2$, and this allows to rewrite the two-point correlation function into the well-known form of the power spectrum [40]

$$\langle\Phi(\boldsymbol{x})\Phi(\boldsymbol{y})\rangle = \int_0^\infty P(k)\;\frac{\sin(kr)}{kr}\frac{\mathrm{d}k}{k} \tag{1.119}$$

where $r = |\boldsymbol{x}-\boldsymbol{y}|$ and the power spectrum of the quantum fluctuations is $P(k) = (2\pi^2)^{-1}k^3\sigma^2(k;\eta)$. Since $\sigma^2(k;\eta)$ is given by the mode function, solving the Klein-

Gordon equation for the quantum scalar field in the Friedmann universe also completely determines the statistics of the ground state wave functional.

We will now turn to the consistency requirements in constructing the effective configuration space. At the bare minimum, this concerns the canonical field operator $\Phi[f] \in \mathcal{A}$, and it must satisfy (1.16) and (1.18) with respect to the boundaries set by the semiclassical approximation. Let l_p be a short distance cutoff given by the inverse of Planck mass $m_p^{-1} = l_p$ that represents the smallness parameters for perturbation expansion, $\phi = \phi_0 + m_p^{-1}\,\delta\phi$. To quantify the validity of the effective field theory at short distances, we consider $|\Phi[f]| \in \mathcal{A}_0$ and compute the dimensionless ratio $\mathcal{R}_l(|\Phi[f]|)$ in accordance with (1.16) in order to qualify the validity of the perturbative expansion:

$$\mathcal{R}_l(|\Phi[f]|) = \frac{1}{V[f]} \int_{\Sigma_t} \mathrm{d}^3\boldsymbol{x}\, f(x)\, \frac{|\Phi(\boldsymbol{x})|}{m_p} = \frac{|\Phi[f]|}{m_p V[f]} \tag{1.120}$$

where $V[f] = \int_{\Sigma_t} \mathrm{d}^3\boldsymbol{x}\, f(x)$ is the total coordinate volume given by the support of f. Let U be the neighborhood with an origin given by the classical background ϕ_0, the filtering semi-norm is given by

$$N(\mathcal{O}, \Psi_t; U) = \frac{1}{m_p V[f]} \int_U \mathscr{D}\phi\, |\phi[f]| \rho_\eta[\phi] = \frac{\langle |\Phi[f]| \rangle}{m_p V[f]}\,. \tag{1.121}$$

Since we consider Gaussian state and require $\Psi_t \in D(\Pi)$, the boundary of the effective configuration space is symmetric, hence $\partial U = \cup_{\boldsymbol{x}} \partial U(\boldsymbol{x})$ and for each point $\boldsymbol{x} \in \Sigma_\eta$ at any conformal time η , $\partial U(\boldsymbol{x}) = \{-\phi_\Lambda(\boldsymbol{x})\phi_\Lambda(\boldsymbol{x})\}$. A key requirement is that the boundary of the effective configuration space be uniform for all $\boldsymbol{x} \in \Sigma_\eta$, i.e. $\phi_\Lambda(\boldsymbol{x}) = \phi_\Lambda(\boldsymbol{x}')$ for all $\boldsymbol{x} \neq \boldsymbol{x}'$ for all η. This condition is strictly required by the strong equivalent principle. Finally, we restrict our analysis to consider initial data of the Gaussian state that is valid under the semiclassical approximation, which requires $\Psi_{\eta_0}[\phi]|_{\partial U} \approx 0$ at the initial time η_0. Take the maximum of $N(\mathcal{O}, \Psi_t; U)$, therefore, requires us to choose the largest possible neighborhood U, where the boundaries $\phi_\Lambda(\boldsymbol{x}) = m_p$ is set by the Planck mass for all $\boldsymbol{x} \in \Sigma_\eta$.

While the condition $N(\mathcal{O}, \Psi_t; U) = 1$ marks the complete breakdown of the perturbative method, the semi-classical framework becomes unreliable before this limit

has been reached. This is because admissible fluctuations satisfying (1.121) do not necessarily preserve the stability of the classical background configuration as required in (1.18). It is therefore important to impose (1.18) simultaneously. In the absence of a classical background, we have $\phi_0 = 0$ such that $\phi = m_p^{-1}\delta\phi$. So, for a free theory, there is no classical counterpart against which the quantum scalar field can directly compare. Nevertheless, the semiclassical framework assumes the spacetime geometry remains insensitive to the energy-momentum tensor sourced by the quantum fluctuations. By dimensional analysis, this consistency requirement demanding background stability (1.18) further restricts the size of the neighborhood to the subset $U_1 \subset U_0$ determined by the ratio $\mathcal{R}_0(\,|\Phi[f]|\,, \Psi_\eta)$ using the Ricci scalar R as the reference classical observables, $\mathcal{O}_0 = R^{1/2}$.

1.5.1 Quantum Field Simulation

Although the analytical estimation of (1.16) and (1.18) is difficult due to the nature of the functional integration over a compact configuration space instead of an infinite one, it can be conceptually straightforward to evaluate numerically. Let ϕ_{sim} denote the Gaussian random field realization that is statistically consistent with, and thus, emulates the random variable ϕ of the probability density distribution of the Gaussian state $\rho_\eta[\phi]$. So the ensemble average over all random field realizations ϕ_{sim} produces the Gaussian statistics of $\rho_\eta[\phi]$ as described in (1.113) and (1.114). To estimate (1.16) and (1.18) numerically, we will proceed in two steps: First, to obtain $|\Phi[f]|$, we compute the spatial average of each simulated Gaussian random field ϕ_{sim}, via $N^{-3}\sum_{i,j,k=0}^{N}|\phi_{\text{sim}}(x_i, x_j, x_k)|$ where N is the total number of pixels contained within the simulation, and assuming that the support f is given by the entire simulation volume. Then, we perform repeated sampling over many Gaussian random field realizations ϕ_{sim} in order to consider all possible values ϕ can take, which therefore replaces the functional integral over the effective configuration space by ensemble averaging of ϕ_{sim}. This gives

$$\langle|\phi_{\text{sim}}|\rangle_{\text{S}} = \left\langle N^{-3}\sum_{i,j,k=0}^{N}|\phi_{\text{sim}}(x_i, x_j, x_k)|\right\rangle\,, \tag{1.122}$$

where $\langle\cdot\rangle_S$ is the ensemble average of all random field simulations performed. Since ϕ_{sim} follows the same Gaussian statistics as $\rho_\eta[\phi]$, $|\phi_{sim}|$ follows a half-normal distribution (See e.g. Figure 1.2), such that

$$\sigma^2(|\phi_{sim}|) = \left\langle (|\phi_{sim}| - \mu(|\phi_{sim}|))^2 \right\rangle_S = \frac{2}{\pi}\langle|\phi_{sim}|\rangle_S^2 \tag{1.123}$$

is the variance of the random field simulation. At the technical level, ϕ_{sim} represents a discrete random field defined in the position space with finite extent. Equivalently, ϕ_{sim} is obtained by performing the inverse discrete Fourier transform of the prescribed power spectrum multiplied with a stochastic field in the momentum space[5]. This implies that there exists a spatial resolution limit for the random fields: it can resolve microscopic details of fluctuations on scales smaller than a single pixel, nor capture macroscopic variation on scales larger than the simulation size.

Contracting Radiation-Dominated Universe

We now consider two distinct cosmological setups: a contracting radiation-dominated universe and an expanding de Sitter spacetime. The former presents a straightforward example to demonstrate the breakdown of the semiclassical framework through the amplification of quantum fluctuations due to the violent gravitational collapse of relativistic matter. Specifically, for a contracting radiation-dominated universe, the scale factor is given by $a(\eta) = a_0\eta$ with $\eta \in (-\infty, 0)$, $a_0 \in \mathbb{R}$, and we set $a_0 = 1$ for simplicity. Let $u(k,\eta)$ be the mode function of a massive scalar field and define the auxiliary field by $v(k,\eta) = a(\eta)u(k,\eta)$. By the least action principle, they satisfy the Klein-Gordon equation generally for a general scale factor $a(\eta)$ by [40–42]

$$\partial_\eta^2 v(k,\eta) + \left(k^2 - m^2a^2(\eta) + \frac{\partial_\eta^2 a(\eta)}{a(\eta)}\right) v(k,\eta) = 0 \tag{1.124}$$

For a contracting radiation dominated universe with $a(\eta) \propto \eta$, the equation of motion simplifies to $\partial_\eta^2 v(k,\eta) + k^2 v(k,\eta) = 0$ and the factor $m^2a^2(\eta) = 0$ is negligible for either a massless scalar field or in the massless limit of a massive scalar

[5] A more detailed discussion of the fast generation of Gaussian random fields is discussed in the Section 2.2.1

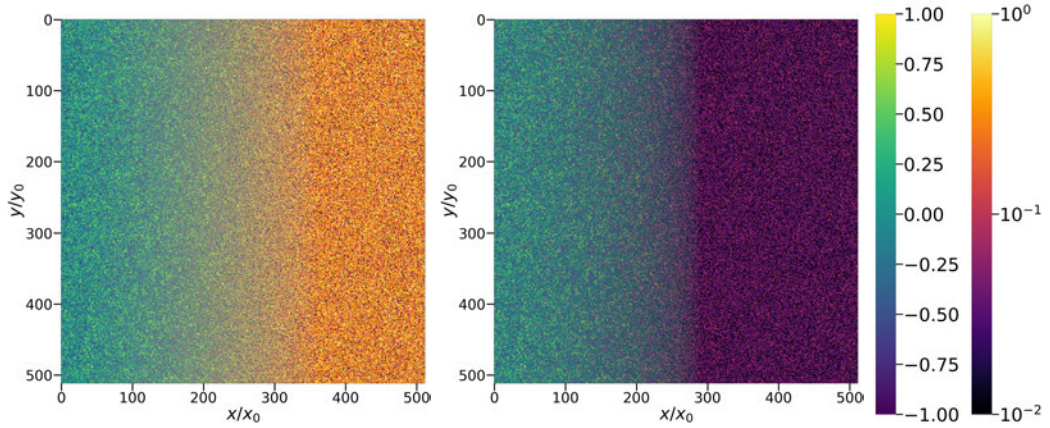

Figure 1.1. Gaussian random field simulations of quantum fluctuations in a radiation-dominated universe within a volume of scale $L \sim (k_0/2\pi)^{-3}$ determined by k_0. The random fields are evaluated on the x-y-plane at $z = L/2$ at conformal times $\eta = 10\eta_0$ (left) and $\eta = \eta_0$ (right). In each panel, it shows the normalized amplitude (left) and the magnitude (right). As quantum fields evolve from the low-curvature region at $10\eta_0$ into the high-curvature region to η_0, the spacetimes dynamics amplify quantum fluctuations by at least two orders of magnitude with consistent spatial correlation. In particular, quantum fluctuations that are outside the domain of validity, $|\varphi_{\rm sim}| > \varphi_\Lambda = 1$, are excited everywhere and marked by the brightest spots at $\eta = \eta_0$. This hints, at a preliminary level, at a substantial unitarity loss in our semiclassical system at the time scale $\eta = \eta_0$, indicating the breakdown of the semiclassical approximation in the effective field theory.

field ($k^2/a^2(\eta) \gg m^2$). For demonstration purposes, we restrict to consider a massless scalar field, so that the equation of motion for the mode function $u(k,\eta)$ admits the following solution:

$$u(k,\eta) = \frac{e^{ik\eta}}{\sqrt{2k}\, a_0 \eta}\,. \tag{1.125}$$

Using that relation that $\sigma^2(k,\eta) = |u(k,\eta)|^2$, the variance of the Gaussian wave functional is found to be $\sigma^2(k,\eta) = (2k\eta^2 a_0^2)^{-1}$. This indicates that the quantum field has a consistent spatial correlation across all conformal time η, which is illustrated intuitively in Figure 1.1. In the Gaussian random field simulation of quantum fluctuations, it has adopted a simple set of parameters given by $k_0 = |\eta_0|^{-1} = 1$ and $m_p = 1$.

We will now examine the reliability of the semiclassical approximation using (1.16) and (1.18). As a proof of concept, we select the Hubble parameter $H_0(\eta) = 1/\eta$ as the

classical observables since $R^{1/2} = H_0(\eta)$. Then we compare it with the expectation value of $|\Phi(f)|$ under the criteria (1.16) and (1.18). In a radiation-dominated universe, we expect (1.18) to hold consistently over time because $\sigma \propto 1/\eta$ has the same scaling as $H_0 = 1/\eta$. This means that (1.18) is satisfied and remains constant for all conformal time η of a massless scalar field, provided that the initial data is valid within the semiclassical approximation.

While the condition (1.18) holds for all time, the same does not hold for (1.16). As shown in Figure 1.1 and 1.2, the contraction of the radiation-dominated universe significantly amplifies the magnitude of quantum fluctuations. At last, this amplification becomes so strong that it drives a significant probability flux leaving the effective configuration space with boundaries marked by the semiclassical domain $|\phi_\Lambda| = 1$. This dynamics can be seen from the flattening behavior of the probability density distribution as shown in Figure 1.2.

It becomes more evident from Figure 1.1 that the quantum fields begin to excite fluctuations of extreme magnitudes $\phi_{\text{sim}} > 1$. These fluctuations are represented by the brightest spot in Figure 1.1, and they started to populate everywhere at $\eta = \eta_0$. Beyond this point, the criterion (1.16) is no longer satisfied, and the semiclassical framework breaks down. This is further supported by the divergence of the spatially averaged standard deviation of ϕ_{sim} as $\eta \to 0$, which can be seen from Figure 1.2.

It is important to note that the condition $\max N(|\Phi(f)|, \Psi_\eta; U_0) < 1$ cannot be restored at any later time η_1 by restricting the analysis to an even smaller neighborhood U_1. In fact, such a restriction can only lead to a more severe unitarity loss because the contraction of the validity domain excludes an even larger portion of the total probability. This, consequently, can only further invalidate the existing framework. Given that the standard deviation of quantum fluctuations diverges as $1/\eta^2$ in a radiation-dominated universe, we expect the following chain of inequalities upon contracting the neighborhood by $U_2 \subseteq U_1 \subseteq U_0$ for $|\eta_1| > |\eta_2|$:

$$\ldots \leq \|\Psi_{\eta_2}\|_{U_2} \leq \|\Psi_{\eta_2}\|_{U_1} \leq \|\Psi_{\eta_1}\|_{U_1} \leq \|\Psi_{\eta_1}\|_{U_0} \tag{1.126}$$

Thus, ultimately at some later time $\eta_f \to 0$, the only possible neighborhood is the set of measure zero with a zero norm.

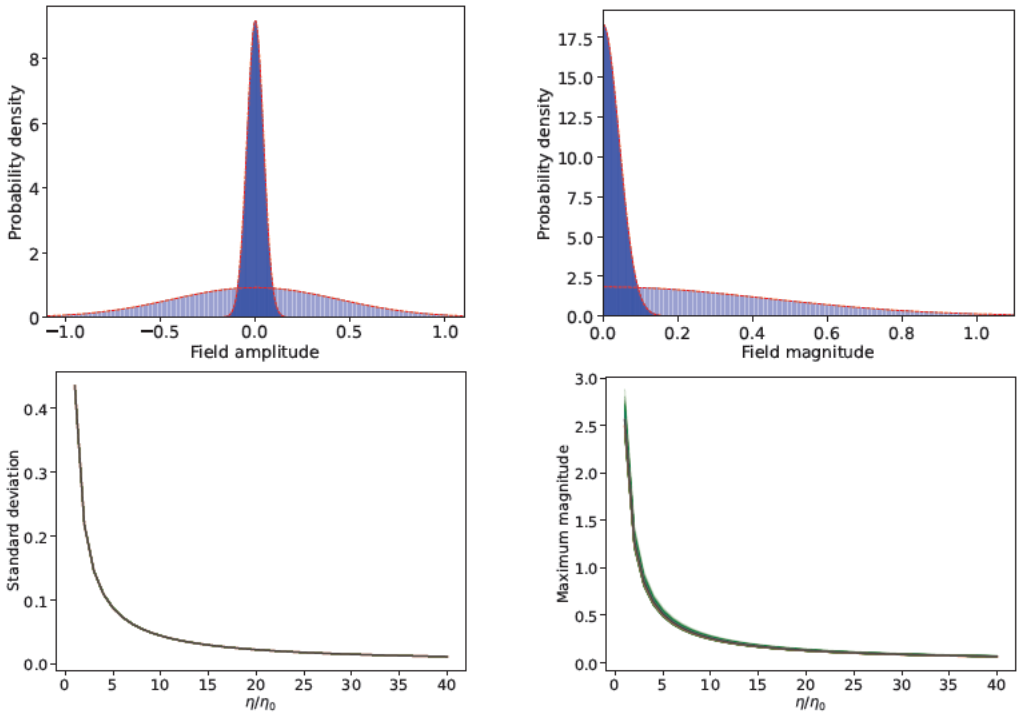

Figure 1.2. Statistics of the Gaussian random field in the radiation-dominated universe. The top row shows the probability density distribution of the Gaussian random field in Figure 1.1 at conformal times $\eta = 10\eta_0$ and $\eta = \eta_0$. The left panel shows the amplitude normalized by three times its standard deviation, while the right panel shows the magnitude. As the system evolves from $\eta = 10\eta_0$ to $\eta = \eta_0$, the initially narrow distribution flattens, indicating the amplification of quantum fluctuations when fields enter spacetime regions with intense dynamics. This amplification causes a probability flux to leak beyond the domain of validity marked by the boundary $|\varphi_\Lambda| = 1$, signaling a strong unitarity loss as time progresses beyond $\eta = \eta_0$. The bottom row reinforces this interpretation by tracking the standard deviation of the random field and its maximum magnitude across 200 simulations during the time interval $\eta/\eta_0 \in [1, 40]$ with a step size of $\Delta\eta/\eta_0 = 1$. The red, green, and black curves represent the evolution in Figure 1.1, individual simulations, and their averages, respectively, and all are overlapping. This demonstrates that the semiclassical framework breaks down at high confidence when $\eta \leq \eta_0$, since the standard deviation diverges consistently across all random field simulations.

de Sitter Universe

In contrast to the collapsing radiation-dominated universe, the de Sitter spacetime requires a more careful selection of initial data. The de Sitter spacetime is characterized by a scale factor $a(\eta) = (-a_{\text{dS}}\eta)^{-1}$ for $\eta \in [-\infty, 0)$ and a_{dS} is the time-independent

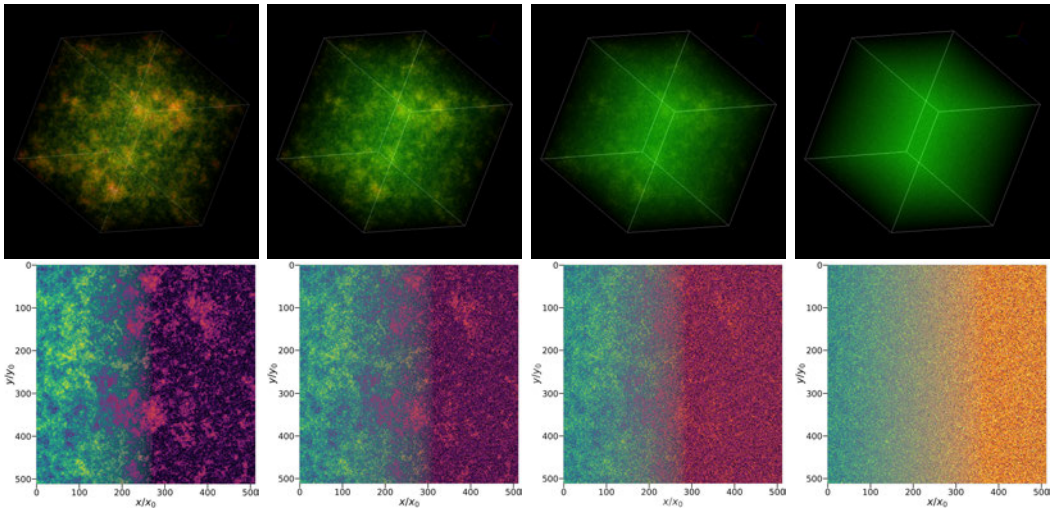

Figure 1.3. Gaussian random field simulations of quantum fluctuations in the de Sitter spacetime within a volume of scale k_0^{-3} at conformal times $\eta/\eta_0 = \{10, 2, 1, 0.2\}$ (from left to right, with $\eta < 0$ and $\eta_0 < 0$). The top row displays the normalized magnitude of a three-dimensional volume-rendered random field, where stronger signals appear more opaque and weaker signals more transparent. It demonstrates an initial homogeneous isotropic configuration at $\eta = 0.2\eta_0$ developing large-scale structures as the system evolves into the future. The bottom row further illustrates this by showing the random field evaluated on the x-y-plane at $z = 1/2k_0$ at the same conformal times. Each panel shows the normalized amplitude (left) and the magnitude (right). In contrast to the radiation-dominated universe (Figure 1.1), as the system evolves forward in time, large-scale structures form while quantum fluctuations are diminished. This indicates that any field configurations admissible in the far future originate from the distant past, where extreme fluctuations are dominant, marked by the brightest spots. This suggests that, in order to comply with the semiclassical approximation, any semiclassical effective framework must restrict its initial quantization to a smaller time domain.

Hubble parameter, set to be $a_{\text{dS}} = 10^{-2}$ for convenient conceptual illustrations. The mode function $u_k(\eta)$ satisfying the Klein-Gordon equation in de Sitter spacetime can be expressed in terms of the Hankel functions:

$$u_k(\eta) = a_{\text{dS}} \frac{\sqrt{\pi}\eta^{3/2}}{2} \left(c_1 H_\nu^{(1)}(k\eta) + c_2 H_\nu^{(2)}(k\eta) \right) \tag{1.127}$$

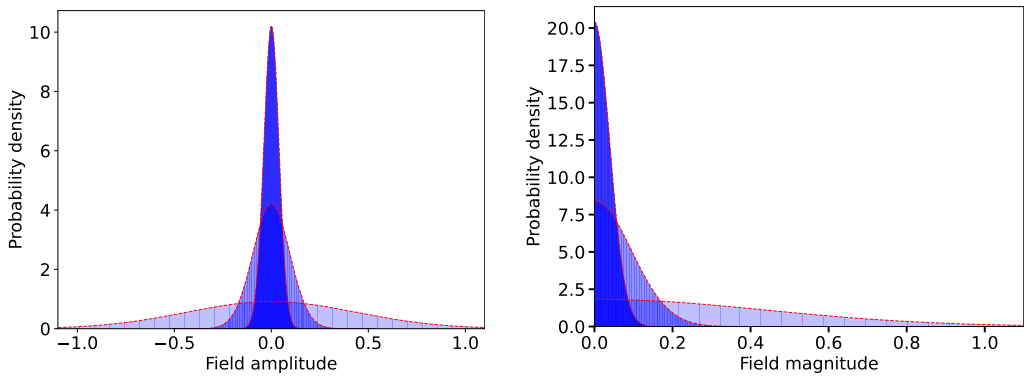

Figure 1.4. Shown is the probability density distribution of the random field in Fig. 1.3 at conformal times $\eta/\eta_0 = \{10, 2, 0.2\}$ (from flattest to steepest) in de Sitter spacetime. The left panel shows the amplitude normalized by three times its standard deviation, while the right panel shows the magnitude. As the system evolves from $\eta = 10\eta_0$ to $\eta = 0.2\eta_0$, the distribution bulges at its mean. This indicates that the effective framework in an expanding de Sitter spacetime is highly reliable, with an approximately unitary evolution as the probability of exciting fluctuations beyond the semiclassical domain remains minimal for all late times. Nevertheless, although the effective framework remains robust in the future, the flattening of the distribution at the early time constrains the time domain for initial quantization to be within the range of validity set by the consistency requirements (1.18) and (1.16).

where $v^2 = (9/4) - 12(m^2/R + \zeta)$. Adopting the Bunch-Davis vacuum we take $c_1 = 0$ and $c_2 = 1$ [43, 44], then the variance becomes

$$\sigma^2(k,\eta) = \left| a_{\rm dS} \frac{\sqrt{\pi}}{2} \eta^{3/2} H_\nu^{(2)}(k\eta) \right|^2 . \tag{1.128}$$

For a minimally coupled massless scalar field, we have $v = 3/2$, which simplifies the Hankel function

$$u_k(\eta) = \frac{\eta a_{\rm dS} e^{-ik\eta}}{\sqrt{2k}} \left(1 - \frac{\mathrm{i}}{k\eta}\right) \tag{1.129}$$

This results in the variance $\sigma^2(k,\eta)$, which transits from $1/k$ to $1/k^3$ as the conformal time η evolves from $-\infty$ to 0. This suggests the formation of large, spatially correlated structures, which is illustrated in Figure 1.3 for their formation effectively begins after $\eta = 2\eta_0$ (second panel from the left).

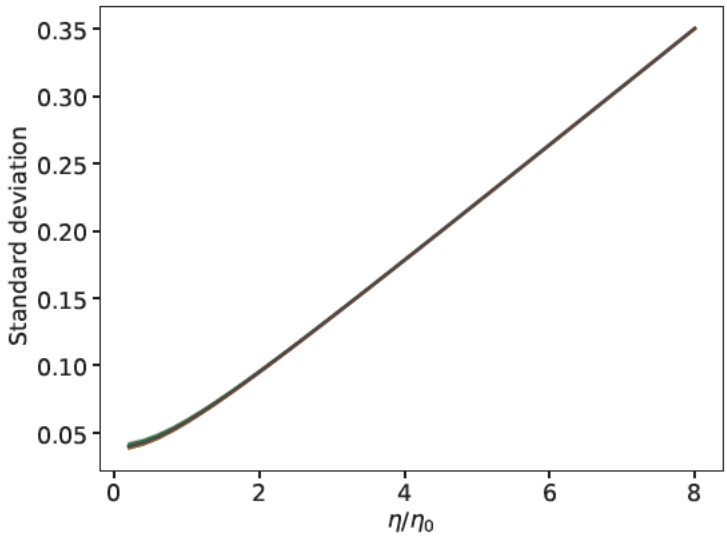

Figure 1.5. Standard deviation of the probability density distribution in de Sitter spacetime across 200 random field simulations during the conformal time interval $\eta/\eta_0 = [0.2, 8]$, with a time step of $\Delta\eta/\eta_0 = 0.2$. The red, green, and black curves represent the evolution of Fig. 1.3, individual simulations, and their averages, respectively, and are all overlapping. As conformal time evolves backward into the past, the standard deviation scales linearly, with the consistency requirement (1.18) breaking down at $\eta \sim 3\eta_0$ and (1.16) at $\eta \sim 25\eta_0$. This indicates that fluctuations are extreme at early times, suggesting that not all initial times are suitable for setting initial conditions.

Again, to assess the reliability of the semiclassical framework, we apply criterion (1.18) and choose the Hubble parameter $|H_0|$ as the classical observable. In this case, the criterion (1.18) is given by $\eta \max N(|\Phi(f)|, \Psi_\eta; U_0) < \delta$, for $\delta = 1/4$ as an example.

So, in strong contrast to a collapsing radiation-dominated universe, the expansion of the de Sitter universe suppresses the magnitude of quantum fluctuations. This suppression is clearly visible in Figure 1.3, and is further demonstrated by the decrease in standard deviation over time as shown in Figure 1.5, alongside the narrowing of the probability distribution in Figure 1.4 that indicates a low probability to excite fluctuations of the order of the short distance cut-off scale.

It follows from Fig. 1.5 that the condition $\eta \max N(|\Phi(f)|, \Psi_\eta; U_0) < 1/4$ can be consistently fulfilled for all $\eta/\eta_0 \leq 2$ as $\eta/\eta_0 \to 0$. However, in de Sitter spacetimes, potential issues arise not at the late times, but at the early times when fluctuations

show greater variance in their magnitude Figure 1.5, which means fluctuations were significantly more violent in the past. Physically, this implies that while the field configurations are highly reliable at arbitrary late times, it is not sensible to extrapolate them arbitrarily far back into the past within the semi-classical framework. This underlines the inconsistency of utilizing arbitrary initial data from the distant past, since such data fulfills neither (1.16) nor (1.18). Therefore, only initial data prepared after a certain time scale, those respects the semiclassical assumption for a given length scale $1/k_0$, should be selected. Once equipped with valid initial conditions, the subsequent time evolution in de Sitter spacetime can be modeled under the effective semiclassical framework with excellent accuracy into the future.

1.6 Conclusion

In this chapter, we developed a diagnostic framework for assessing the range of validity of effective field theories operating in semiclassical spacetime backgrounds. This framework is based on local geometric criteria of the effective configuration field space, which addresses the short-distance limitations of the theory and the stability of the classical observables that constitute the semiclassical framework. Boundaries of effective configuration field space correspond either to quantum fluctuations that merely shift the classical background configuration on scales much larger than the effective short-distance cut-off, or to quantum fluctuations triggering sizable backreactions on smaller scales. The location of these boundaries also depends on the set of observables chosen by the observers. Relative to this set, these boundaries establish the domain that guarantees the consistency of the effective description and the validity of the semiclassical approximation (1.16) and (1.18). In particular, (1.18) measures the magnitude of backreactions and is thus indicative of the background stability. In general, probability fluxes penetrating these boundaries and leaking into regions beyond the effective field configuration space correspond to excitations of quantum fluctuations that are outside the spectrum of fluctuations permitted by the effective field theory. Consequently, dynamical aspects of the effective description are governed by a contractive evolution semigroup, rather than a unitary representation of time translations.

To quantize the effective field theory, we showed that the basic observables, in our case, the canonical field operator and its conjugate momentum, enjoy self-adjoint extensions on a specific Hilbert space. At the kinematical level, the canonical momentum field operator admits infinitely many self-adjoint extensions. By the standard functional calculus, this property extends to the Hamiltonian operator, again at the kinematic level. However, at the dynamical level, in general, the solution space of the functional Schrödinger equation has no nontrivial intersection with the domains on which the Hamiltonian admits self-adjoint extensions. Important exceptions are static spacetimes. Provided that the theory is free of ghosts, the evolution must be contractive. The loss of unitarity, usually a sacrosanct requirement for a consistent and fundamental probabilistic framework, has a well-understood reason: The existence of boundaries in effective field configuration space, through which probability can be leaked.

Of course, the loss of unitarity is vital for the existence of a more fundamental description. There are spacetimes that, when populated with quantum fluctuations, preserve the semiclassical approximation because potentially harmful excitations are too rare to impact the large-scale background geometry. Intuitively, these can be imagined as almost static or mildly dynamical spacetimes. Contrary to these, there are spacetimes that support the excitation of free quantum fluctuations that trigger background instabilities and invalidate the semiclassical approximation at the global level.

In order to demonstrate the framework developed in this work, we complement our formal analysis with numerical experiments. As a proof of concept, with the aid of our numerical experiments, we identify regions in cosmological spacetimes where freely evolving quantum fluctuations violate unitarity to an extent that the semiclassical approximation is locally invalidated. As a concrete example, we consider a collapsing universe filled with radiation. This spacetime geometry borders on a future singularity. As can be expected, there is a substantial probability flux in its vicinity penetrating the configuration field boundaries, thereby exciting fluctuations that destabilize the background, leading to a breakdown of the semiclassical approximation (Fig.1.2). In contrast, and as another example, we consider quantum fluctuations populating de Sitter spacetime: In this case, the semiclassical approximation holds towards the future (given appropriate initial conditions), but ceases to hold in the past. This indicates that semiclassicality further restricts acceptable initial conditions by limiting the time domain where initial quantization is performed. This is crucial because, even if regular initial conditions are chosen by hand, the semiclassical approximation can immediately break down once the system evolves outside the allowed time domain.

Chapter 2

Rare Events Statistics of Spatial Correlated Random Fields

The results presented in this chapter are based on a collaborative work with James Creswell, Florian Kuhnel and Dominik Schwarz. It is currently under review in Physical Review D. The preprint is available at `https://arxiv.org/abs/2501.17936`

2.1 Introduction

In the standard model of structure formation, galaxies and their clusters grow from over dense region in the primordial density field through gravitational instability. The largest and the rarest of these overdensities are capable of collapsing into massive objects at the high redshift Universe [45–47]; and in the extreme case, they may even satisfy the necessary conditions to form primordial black holes. Their observational relevance have recently increased substantially as well due to the discovery of massive galaxies at high redshift, which are more massive and abundant than expected from the standard model of star formation in ΛCDM cosmology [48–64]. Even more striking are the strong evidence of supermassive black holes at high redshift [65–71] whose mere existence places tight constraints on their possible origins. Since primordial density distributions are quantum fluctuations stretched to the macroscopic scale during inflation [41, 72], the observed population of large overdensities directly constrains inflationary physics by its mechanism for generating primordial non-Gaussianity.

The theoretical framework for studying such rare events and providing predictive power for their population is extreme value theory [73, 74]. Classical extreme value theory, however, is derived under the assumptions that poorly match applications to many physical scenarios including cosmology. Analytic studies of extreme value theory assume statistically independent and identically distributed random variables, typically in the asymptotic limit that involves a sequence of infinitely many events.

Correlations, on the contrary, are ubiquitous in many physical systems, as well as the leading causes of the formation of interesting patterns and long-range structures. Especially in cosmology, overdensities do not evolve in isolation, but gravity causes accretion of surrounding material if the initial overdensities are large enough to source a gravitational field that overcomes its surrounding radiation pressure. For this reason, matter perturbation and any other relevant quantities can only be accurately modeled with spatially correlated random fields, with their correlation structure prescribed by the power spectrum [75]. For rare events, in particular, their statistics are expected to deviate strongly from the independent case, because the probability of finding a rare event can be significantly enhanced in the vicinity of another if strong spatial correlations are present.

For these reasons, the purpose of this chapter is to extend extreme value theory and its toolkits to describe statistically dependent random events in the context of three-dimensional random fields with Gaussian and exponential statistics. On one hand, Gaussian random fields provide the canonical description of primordial fluctuations consistent with observation in the Cosmic Microwave Background (CMB) on the megaparsec scale [45, 46, 76–80]. Exponential random fields, on the other hand, mimic the proposed long tail behaviors that lead to the largest overdensities in the primordial density fluctuation at a sufficiently small scale [81–85]. Nevertheless, in contrast to Gaussian random fields, spatially correlated exponential random fields are rarely studied, and a general analytical formulation is still lacking. As we will show later, existing extreme value theory can be generalized to describe the statistics of rare events in spatially correlated random fields, provided that there exists a notion of correlation length that defines a minimal neighborhood size. Beyond that, we propose to use weighted principal component analysis to measure non-sphericity within a local cluster that contains a rare event and show how spatial correlations influence their geometry.

Let us start with the definition of an extreme value. Suppose $X_1, X_2, ..., X_n \in \mathbb{R}$ is a sequence of random variables sampled from $n \in \mathbb{N}$ measurements. The extreme values of this sample of size n is defined by taking either the minimum $M_1 = \min(X_1, X_2, ..., X_n)$ or the maximum $M_n = \max(X_1, X_2, ..., X_n)$ of the given sequence. In this chapter we consider particularly the statistics of M_n relevant to the context of cosmology. Let $z \in \mathbb{R}$ be a threshold value and $M_n \leq z$, so $X_i \leq z$ for all $i \in n$ because M_n is the maximum of the sequence. This means that the

probability $\mathbb{P}(M_n \leq z)$ to find $M_n \leq z$ is given by the joint probability distribution of finding all events $X_i \leq z$ for all $i \in n$. The analytic expression for $\mathbb{P}(M_n \leq z)$ is not known generally, even if the individual probability distribution $F(X)$ (or the cumulative distribution function) is known. So most analytic studies are restricted to consider $\{X_1, X_2, ..., X_n\}$ that are statistically independent and identically distributed. In this context, the probability to find $X_i \leq z$ for all $i \in n$ are equals: $F(X_1 \leq z) = F(X_2 \leq z) = \cdots = F(X_n \leq z)$. Then the maximum $M_n \leq z$ for any value of $n \in \mathbb{N}$ is given by the joint distribution function:

$$\begin{aligned} G(z) \equiv \mathbb{P}(M_n \leq z) &= \mathbb{P}(X_1 \leq z, ..., X_n \leq z) \\ &= \prod_{i=1}^{n} \mathbb{P}(X_i \leq z) = F^n(z) \end{aligned} \tag{2.1}$$

where in the last line we used the property that X_i is independently distributed for all $i \in n$. From this we can also determine the probability density function $g(z)$ of extreme values by taking the derivative with respect to z:

$$g(z) = \frac{\partial G(z)}{\partial z} = n(F(z))^{n-1} f(z) \tag{2.2}$$

For a given value of z, the probability $G(z)$ decreases in the power of n. This means that $G(z)$ will always shift to the right with increasing observation sample size n as illustrated in Figure 2.1. Suppose we take the asymptotic limit $n \to \infty$ (or sufficiently large n) and set $x_0 = \sup\{x : F(x) < 1\} \leq \infty$, and $\lim_{n\to\infty} M_n = x_0$, then ultimately $G(z) = \lim_{n\to\infty} F^n(z) = 0$ for $F(x) < 1$ and $G(z) = 1$ for $F(x) = 1$. This means that the distribution of extreme values eventually degenerates into a binary output at the asymptotic limit that is sensitive to only $F(z) = 1$ and $F(z) < 1$. This can be improved by introducing a linear normalization that rescales M_n by

$$\tilde{M}_n = \frac{M_n - b_n}{a_n}\,. \tag{2.3}$$

with sequences of constants $\{a_n > 0\}$ and $\{b_n\}$ for $a_n, b_n \in \mathbb{R}$ for all n. Suppose there exists a choice of a_n and b_n that could stabilize M_n, then by the Fisher–Tippett–Gnedenko theorem [74, 83, 86, 87] $G(z)$ can converges weakly to a non-

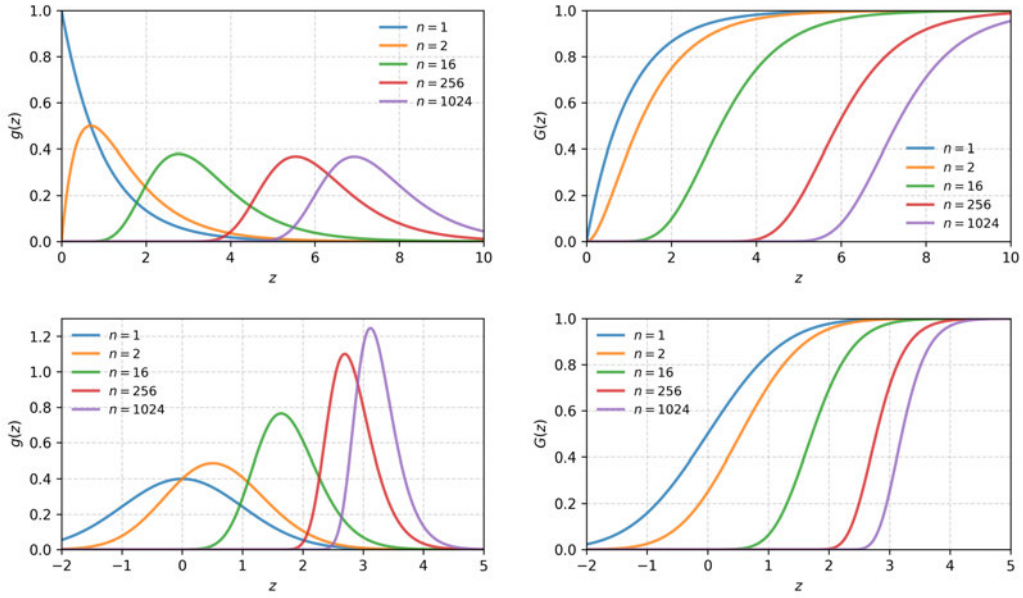

Figure 2.1. Demonstration of probability density distribution $g(z)$ (left) and the probability distribution $G(z)$ (right) of extremes using exponential distribution (top) with unit rate parameter, and Gaussian distribution (bottom) with zero mean and unit variance. As n increases, both $g(z)$ and $G(z)$ shift to the right.

degenerate distribution function at the limit $n \to \infty$, and $G(z)$ belongs to one of the following three possible classes of extreme value distribution:

$$\text{Gumbel (Type I)} \qquad G(z) = e^{e^{-z}}, \quad -\infty < z < \infty \tag{2.4}$$

$$\text{Frecht (Type II)} \qquad G(z) = \begin{cases} 0, & z \leq \mu \\ e^{-z^{-\alpha}}, & z > \mu \end{cases} \tag{2.5}$$

$$\text{Weibull (Type III)} \qquad G(z) = \begin{cases} 1, & z < \mu \\ e^{-z^{\alpha}}, & z \geq \mu \end{cases}, \tag{2.6}$$

where $z = (x - \mu)/\beta$ with $\mu, \beta \in \mathbb{R}$ being the location and scale parameter; α is a real positive shape parameter for type II and III extreme distribution. On the intuitive level, the tail property of the parent probability distribution determines to which extreme value distribution it converges, because extreme values populate the tail distribution of the probability distribution at a sufficiently large n. Probability density distributions with exponentially decaying tails converge asymptotically to the Gumbel (Type I) class;

For those with a heavy polynomial tail, they converge to the Frecht (Type II) class; Finally, distributions with a finite upper bound for maxima or a finite lower bound for minima converge to the Weibull (Type III) class.

For illustrative purposes, let us demonstrate how the exponential distribution $f(z) = \lambda e^{-\lambda z}$ for $\lambda > 0$ and $\lambda \in \mathbb{R}$ converges to the Gumbel distribution. The maximum value from a sequence of n random events sampled from an exponential distribution function is the product of the distribution function: $G_\lambda(z) = (\,1-e^{-\lambda z}\,)^n$, for $z \in [0, \infty]$, such that the corresponding density function is given by $g_\lambda(z) = \lambda n(1 - e^{-\lambda z})^{n-1} e^{-\lambda z}$, illustrated in Figure 2.1 for $\lambda = 1$ with different values of n. Let us expand $G(z)$ in series using binomial theorem:

$$G(z) = F_\lambda^n(z) = (1 - e^{-\lambda z})^n = 1 - ne^{-\lambda z} + \frac{n(n-1)}{2!} e^{-2\lambda z} + \cdots \tag{2.7}$$

For large n, including the asymptotic limit, the binomial series reduces to a double exponential function $G_\lambda(z) = e^{-ne^{-\lambda z}}$ that depends on n. To stabilize this distribution, we consider sequences of constants $\{a_n\} > 0$ and $\{b_n\}$ such that the double exponential function equals to Gumbel distribution by $ne^{-\lambda(a_n z + b_n)} = e^{-z}$. This means that $G_\lambda(z)$ can converge to the Gumbel distribution at the asymptotic limit for a particular choice of the sequence of constants $a_n = \lambda^{-1}$ and $b_n = \lambda^{-1} \ln n$ that normalizes z [1].

2.1.1 Generalized Extreme Value Distribution

In the applications of extreme value distribution, it is intuitive to proceed with adopting one of the three families and then to estimate the relevant parameters of that distribution. There is a major weakness in this approach: It is first required to choose which of the three families is the most appropriate for the data at hand. Once such a decision is made, any subsequent inferences assume this choice is correct and do not allow for the uncertainty such a selection involves, even if this uncertainty may be significant.

[1] Finally, by the same procedure, it can be shown that the Gaussian distribution gives a double exponential form and converges to the Gumbel distribution for large n by choosing the following sequence of constants [88]: $a_n = \sqrt{2 \ln n}$ and $b_n = \sqrt{2 \ln n} - (\ln \ln n + \ln 4\pi)/(2\sqrt{2 \ln n})$.

A better analysis that eliminates this uncertainty can be made by combining the three classes of extreme value distribution into a single family of models known as the generalized extreme value family of distribution [73, 74]:

$$G(z) = \exp\left\{-\left[1+\zeta(\frac{z-\mu}{\sigma})\right]^{-1/\zeta}\right\}, \tag{2.8}$$

which is defined on the set $\{z : 1+\zeta(z-\mu)/\sigma > 0\}$. This model has three parameters: the location parameter $\mu \in (-\infty, \infty)$; the shape parameter $\zeta \in (-\infty, \infty)$; the scale parameter $\sigma > 0$, and $\mu, \zeta, \sigma \in \mathbb{R}$. The generalized extreme value distribution reduces to the Frechet and Weibull families when $\zeta > 0$ and $\zeta < 0$, respectively. At the limit $\zeta \to 0$, the generalized extreme value family reduces to the Gumbel family with distribution function

$$G(z) = \exp\left\{-\exp\left[-\left(\frac{z-\mu}{\sigma}\right)\right]\right\} \tag{2.9}$$

This unification of three families allows statistical inference of ζ from the data themselves for determining the most appropriate type of tail behavior without subjective prior judgment to adopt a particular extreme value family. This concludes the introduction to the extreme value theory, and in the following section, we will restrict our studies of rare events to three-dimensional random fields in the context of cosmology.

2.2 Statistics of rare events in random fields

2.2.1 Fast generation of random fields

Before we consider the extreme value of a random field, let us first introduce the analytic aspect of a discrete random field and how spatially correlated random fields are generated. While the generation of a Gaussian random field follows strictly from [75], the generation of an exponential random field E involves two steps: First, we generate a spatially-correlated Gaussian random field via the discrete convolution algorithm as in [75, 89]; Then, this Gaussian random field is converted into an exponential random field by a nonlinear transformation that preserves the power spectrum.

Consider a simulation cube of length L with periodic boundary conditions and equally spaced grid positions $x(\boldsymbol{m}) = (L/M)\boldsymbol{m}$, where $\boldsymbol{m}$ is an integer triplet with

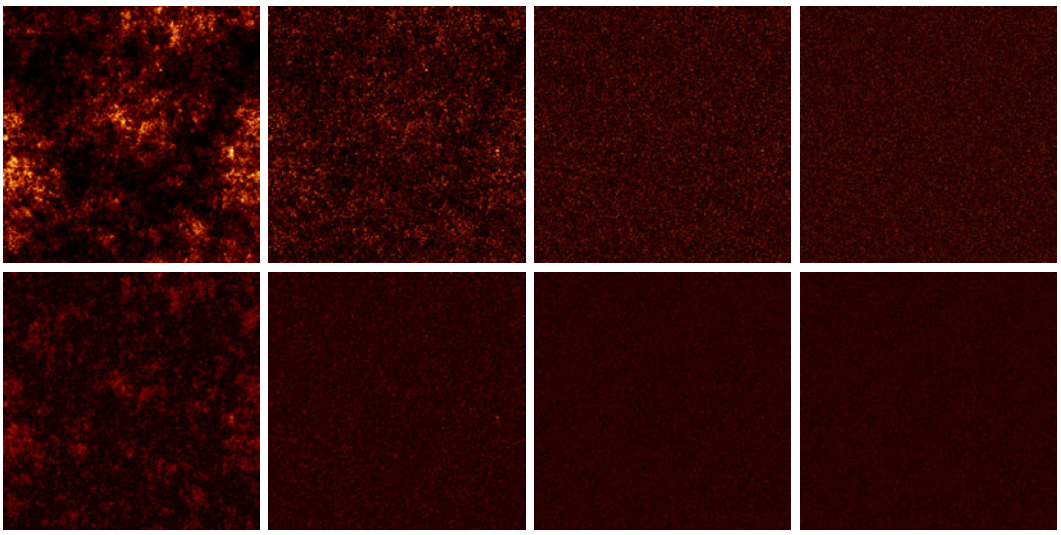

Figure 2.2. Illustration of two-dimensional slices from a three-dimensional random field simulation. The bottom row shows Gaussian random fields F with zero mean, unit variance, and a power spectrum of $P(k) \propto k^n$. From right to left, the spatial correlation increases with decreasing spectral indices $n = 0, -1, -2, -3$, respectively. The top row shows the corresponding exponential random fields E obtained by the nonlinear transformation $F \to E$ via (2.14), which preserves the power spectrum. Note that the exponential random fields exhibit not only stronger signal amplitudes but also larger clustering size, which corresponds to an increased correlation length defined in (2.15).

components $m_i \in [0, M)$. Each spatial grid point $\boldsymbol{m}$ assigns a value $\zeta(\boldsymbol{m})$ that is randomly sampled from a zero-mean normal distribution $\zeta(\boldsymbol{m}) \sim \mathcal{N}(0, 1)$ with unit variance $\sigma = 1$. Since the spatial sampling processes are statistically independent, this generates a spatially uncorrelated Gaussian random field $\zeta_0(\boldsymbol{m})$, with the two-point correlation function of ζ_0 given by

$$\langle \zeta_0(\boldsymbol{m}_1)\zeta_0(\boldsymbol{m}_2)\rangle = M^3\delta_{\mathrm{k}}(m_1, m_2) \tag{2.10}$$

where δ_{k} is the Kronecker delta. Spatial averaging of the discrete field $\langle\, \cdot \,\rangle$ is performed by discrete sums over all lattice sites. Let F be a Gaussian random field with a non-trivial power spectrum $P(k)$, then the discrete Fourier transform is

$$F(\boldsymbol{m}) = \sum_{\boldsymbol{\kappa}} \exp\left(\frac{\mathrm{i}2\pi}{M}\boldsymbol{\kappa}\cdot\boldsymbol{m}\right) T(k)\zeta(\boldsymbol{k}) \tag{2.11}$$

where $T(k) = [(2\pi/L)^3 P(k)]^{1/2} \in \mathbb{R}$ is the dimensionless transfer function, and $\boldsymbol{\kappa} = \boldsymbol{k}L/2\pi$ is the dimensionless wave vector with components $\kappa_i \in [-N/2, N/2)$ for $i = 1, 2, 3$. The complex-valued function $\zeta(\boldsymbol{k}) = \exp[i\varphi(\boldsymbol{k})]$ is a stochastic field with each randomized phase $\varphi(\boldsymbol{k})$ drawn independently from a uniform distribution $\varphi(\boldsymbol{k}) \sim U[-\pi, \pi]$. To understand this, consider the spatial uncorrelated case by setting $T(k) = 1$, then $\zeta(\boldsymbol{k})$ equals to the Fourier amplitude of a spatial uncorrelated Gaussian random field $\zeta_0(\boldsymbol{m}) \propto \sum_{\boldsymbol{\kappa}} \exp(\mathrm{i}2\pi\boldsymbol{\kappa}\cdot\boldsymbol{m}/M)\zeta(\boldsymbol{k})$. This equality means that a spatially uncorrelated Gaussian random field can be generated either from direct spatial sampling in the real space, or by sampling a randomized phase from a uniform distribution in the Fourier space. In our study we obtain $\zeta(\boldsymbol{k})$ by the former approach using discrete Fast Fourier transform of $\zeta_0(\boldsymbol{m})$ by

$$\zeta(\boldsymbol{k}) = \frac{1}{M^3}\sum_{\boldsymbol{m}} \exp\left(-\frac{\mathrm{i}2\pi}{M}\boldsymbol{\kappa}\cdot\boldsymbol{m}\right)\zeta_0(\boldsymbol{m})\,. \tag{2.12}$$

As a result, supply (2.11) with the stochastic field $\varphi(\boldsymbol{k})$ and the power spectrum $P(k)$, we obtain a spatially correlated Gaussian random field F. This field F is then mapped to an exponential random field E in two steps: First, we map $F(\boldsymbol{m})$ into a

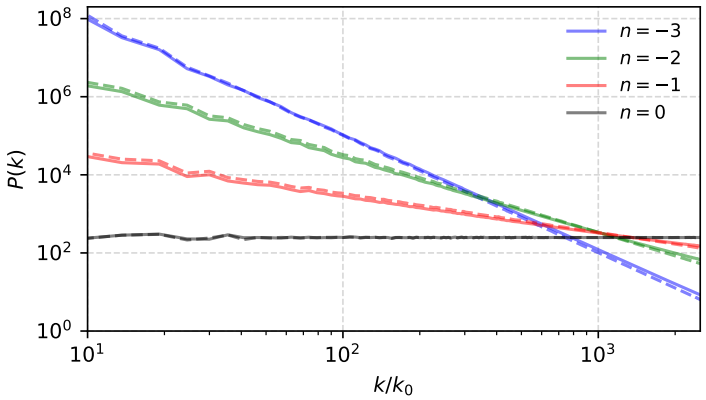

Figure 2.3. The power spectrum of the exponential (solid line) and Gaussian (dashed line) random field for spectral indices of $n = -3, -2, -1, 0$ in logarithmic scale. We can see that the solid and dashed lines are largely overlapping for all n in consideration, which shows that the power spectrum of the Gaussian random field is preserved after performing the nonlinear transformation in Equation (2.14).

uniform distribution $U(\boldsymbol{m}) \in [0, 1]$ by taking the cumulative distribution function of $F(\boldsymbol{m})$:

$$U[F](\boldsymbol{m}) = \text{erf}\left(\frac{F(\boldsymbol{m}) - \mu[F]}{\sqrt{2}\sigma[F]}\right) \tag{2.13}$$

where $\mu[F] = 0$ and $\sigma[F] = 1$ are the mean and the standard deviation of F, respectively. The next step is to map $U[F](\boldsymbol{m})$ to an exponential field $E(\boldsymbol{m})$ by taking the inverse cumulative distribution function $E(\boldsymbol{m}) = -\lambda^{-1} \ln[1 - (1/2)(1 + U[F](\boldsymbol{m}))]$. Altogether, this two-step process defines a nonlinear mapping $F(\boldsymbol{m}) \rightarrow E(\boldsymbol{m})$ by:

$$E(\boldsymbol{m}) = -\frac{1}{\lambda} \ln\left\{1 - \frac{1}{2}\left[1 + \text{erf}\left(\frac{F(\boldsymbol{m}) - \mu[F]}{\sqrt{2}\sigma[F]}\right)\right]\right\} \tag{2.14}$$

The question is whether this nonlinear mapping preserves spatial correlation by preserving the power spectrum. While this is non-trivial to prove analytically because of the nonlinearity of the transformation, it is straightforward to show numerically that this nonlinear mapping at least preserves the power spectrum of the form $P(k) \propto k^n$

with spectral indices $n = 0, -1, -2, -3$. This can be seen from Figure 2.3, that the power spectrum obtained from the Gaussian random field and the exponential random field it generates are almost perfectly aligned.

2.2.2 Correlation Length

So far we have discussed spatial correlation described in terms of the power spectrum. We will now consider the application of extreme values theory in random fields, with its primary interest in the analysis of large overdensities in primordial density fluctuations. Conventional analytic framework for the detection of overdensities in Gaussian random fields [47, 76] is performed by identifying peaks over threshold through extremum constraints, i.e.: the gradient of the field is zero and the second derivative is negative definite. The primary assumption of this approach is that the underlying Gaussian random field (or any other statistics) is smooth. This implies that the random field can infinitely resolve to arbitrary infinitesimal details, such that any local maxima can be expanded into a Taylor series and safely truncated at the second order on a sufficiently small scale. This natural assumption encounters several critical issues when generalizing to discrete random fields that have a realistic resolution limit that defines the smallest length scale of the effective theory. First of all, for any discrete random field characterized by the power spectrum $P(k) \propto k^n$ with spectral index of $n > -3$ at large k, finite differences of neighboring pixels are a poor approximation of the spatial derivative. Second, Taylor series obtained from the finite differences method of discrete random field do not generally converge, except when there exists a strong spatial correlation so that the finite differences can accurately approximate the spatial derivative [2]. Since the primary assumption of peak theory [47, 76] of continuous field does not necessarily comply with discrete random fields, analytic results derived from smooth random fields using extremum constraint are incompatible with discrete random fields [3].

[2] As a simple example, for the spectral index $n = 0$ of a Gaussian white noise, the finite differences are again a white noise of the same mean and variance. Such Taylor series therefore do not converge.

[3] A common approach to circumvent the resolution problem is to smooth the random field by convoluting it with a smooth window function. This changes the power spectrum at large k, and such modification needs to be consistent with the physics of that scale. This is important because the local extremum is sensitive to the largest k resolvable, meaning that the peak density is also sensitive to this modification.

For this reason, the natural alternative for accurate peak detection for random fields of finite resolution is to take the local maximum of the field. At the bare minimum, we need to consider at least a set of cubes with size $3 \times 3 \times 3$, and local maxima are detected if the central pixel is the maximum among all pixels of the cube. This is the extreme value of 27 events identically drawn from the same distribution. So the need for peak detection for a discrete random field naturally encompasses the notion of block maxima in extreme value theory. It is also unnecessary to restrict to a cube $3 \times 3 \times 3$, but any cube of arbitrary length $N_{\mathrm{B}} \in [1, M]$. While this leaves N_{B} as a hyperparameter to be determined, this generalization is essential because, at the bare minimum, the box size must be at least greater than the characteristic length scale of spatial correlation l_0 for the underlying random field to tell if the sampled maximum is truly a local maximum that represents a peak. For example, consider white noise with zero spatial correlation. It would still require at least an extension of size $\sqrt{3}$ to tell whether the pixel in consideration is a peak or not.

For the above reason, the notion of correlation length is essential to determine the optimal value for N_{B}, such that it captures accurately the peaks and their statistics within a discrete random field. To begin with, consider the following definition of correlation length l_0 of a random field F defined by [90, 91]

$$l_0[F] = \frac{\sigma_0[F]}{\sigma_1[F]}\,, \tag{2.15}$$

where $\sigma_0[F]$ and $\sigma_1[F]$ are the variance of F and the variance of its gradient, respectively. For discrete field that replaces spatial derivatives by central finite differences, the variance of the gradient becomes

$$\sigma_1^2[F] = \frac{1}{3}\left\langle \nabla F \cdot \nabla F \right\rangle_N = \frac{1}{3}\sum_{i=1}^{3}\left(\frac{F(\boldsymbol{x} + he_i) - F(\boldsymbol{x} - he_i)}{2h}\right)^2 \tag{2.16}$$

where e_i for $i = 1, 2, 3$ are the set of basis vectors in $\mathbb{R}^3$. The factor of $1/3$ is multiplied to average the variance across three spatial directions, since we consider a stationary Gaussian random field F with identical variance along different directions $\sigma_1^2[F](x_1) = \sigma_1^2[F](x_2) = \sigma_1^2[F](x_3)$. The minimum length scale of the simulation

box is normalized to $h = 1$ because the minimum resolvable scale is the unit size between grid points. Altogether, we can provide a theoretical estimation

$$\sigma_1^2[F] = \frac{1}{M^3} \sum_{\boldsymbol{\kappa}} \sin^2(\boldsymbol{k} \cdot e_i) P(k) \tag{2.17}$$

which resemble the same scaling for continuous random field $k^2 P(k)$ only for small k because $\sin^2(\boldsymbol{k} \cdot e_i) \sim k^2$. This captures the behavior we mentioned previously: The discrete random fields in their finest resolution are highly stochastic and are poorly approximated spatial derivative of a continuous random field, except when $P(k) \propto k^n$ for $n < -3$ at the large k limit. In other words, for continuous and discrete fields to agree on σ_1, it requires a sufficiently strong spatial correlation prescribed by $P(k)$.

Nevertheless, note that $l_0(n)$ estimated by (2.15) is a global quantity evaluated over the entire simulation box. A local cluster, on the contrary, occupies only a local neighborhood within the simulation box. This means that the correlation length of a local cluster that contains a rare event at position $\boldsymbol{x}_0$, is a local quantity $l_0(n, \boldsymbol{x}_0)$ that should be measured only with respect to this local cluster. While it is a complex task to analytically reformulate $l_0(n)$ to adopt a local version, it is straightforward to find a rare event and its neighborhood by numerical search within repeated simulations. Then, the local correlation length $l_0(n, \boldsymbol{x})$ can be evaluated using (2.15) within various neighborhood sizes N_B, which provides the relation between $l_0(n, \boldsymbol{x}_0)$ and N_B. The result is shown in Figure 2.4 for exponential random fields, for clusters with its center occupied with a rare event with at least $6\sigma_r$ level[4]. When the box size N_B reaches the full simulation box side N_sim, the local correlation length $l_0(n, \boldsymbol{x})$ becomes the global correlation length $l_0(n)$, which is marked by the for each n in Figure 2.4, and $l_0(n, \boldsymbol{x}_0)$ approaches its asymptotic value as the box side increases.

Using Figure 2.5 we can now decide an appropriate size for N_B: First of all, N_B should be bounded from below by at least $2\langle l_0(n, \boldsymbol{x}_0)\rangle$ because any neighborhood size smaller than $2l_0(n, \boldsymbol{x}_0)$ contains only a fraction of a local cluster. Second, we consider only box size $N_\mathrm{B} \geq 28$ because the standard deviation σ_0 is dominated by the presence of a rare event at the center for smaller box sizes. This effect is so strong that

[4]Here, we refer σ_r as the standard deviation of a normal distribution, and the notion of $6\sigma_r$ level is the probability to draw of a random event outside 6 times the standard deviation of the normal distribution.

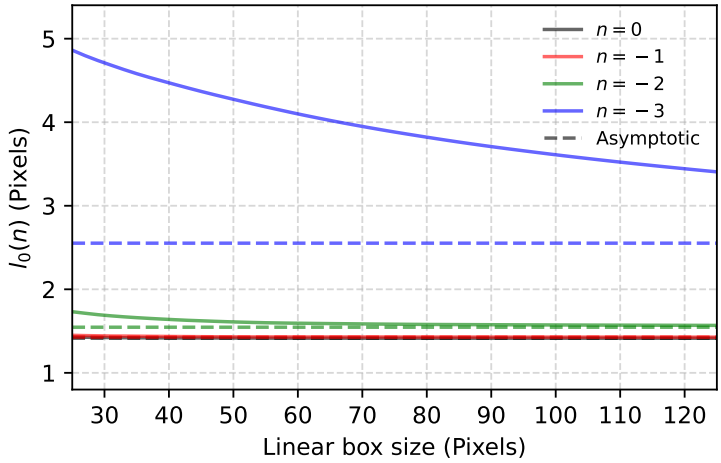

Figure 2.4. Correlation length $l_0(n)$ of exponential random fields for different spectral indices $n = 0, -1, -2, -3$ versus increasing linear box size. In each box, there exists a rare event of at least $6\sigma_r$ at the center. The flat dotted horizontal lines represent the asymptotic (global) correlation length that can be analytically derived from the full random field; Meanwhile, the solid lines are the correlation length as a function of the box size. Note that the curves for $n = 0$ and $n = -1$ are overlapped.

it causes deviation of σ_0 even for $n = 0$ from its asymptotic value $l_0(n = 0)$. Since $n = 0$ is the reference that represents the absence of spatial correlations and clustering effect, the measured value $\langle l_0(n = 0, \boldsymbol{x}_0)\rangle$ must coincide with the asymptotic value to guarantee that any observed deviation between various spectral indices n is solely caused by spatial correlation. Therefore, the box size $N_B \geq 28$ is set as the lower bound to estimate local correlation length.

Accordingly, we choose $N_\mathrm{B} = 33$ for the following analysis of the statistics of rare events in spatially correlated random fields. It is clear that $N_\mathrm{B} > 2l_0(n, \boldsymbol{x}_0)$ and $\langle l(n = 0, \boldsymbol{x}_0)\rangle$ has already reached its asymptotic value. Since it corresponds to approximately 6 times the correlation length for $n = -3$, it is certainly large enough to contain the entire cluster. Meanwhile, $N_\mathrm{B} = 33$ is sufficiently small such that it includes maximally one local cluster for the most interesting case $n = -3$, with estimation of spatial correlation without being diluted by the surrounding empty regions outside the cluster. This latter is illustrated in Figure 2.5, which shows the probability density distribution of the exponential random field within the neighborhood of size $N_\mathrm{B} = 33$, with its center occupied by a $6\sigma_r$ event. We can see that the probability density

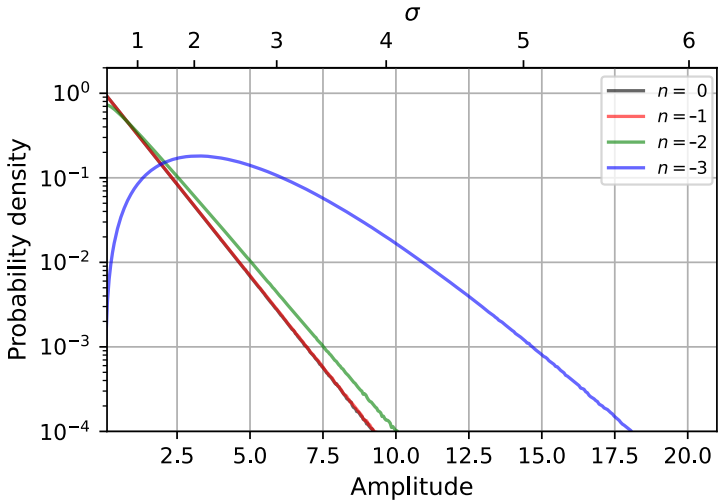

Figure 2.5. Probability density distribution of exponential random field within a block of linear dimension $N_B = 33$ pixels for different spectral indices. Note that the curves for $n = 0$ and $n = -1$ overlap. The smooth probability density distribution is achieved by repeatedly sampling at least 10^3 blocks. Notice that, for $n = -3$, the curve is qualitatively different from the rest of the curve. This is due to the fact that spatial correlation inside the box for $n = 3$ is sufficiently strong, such that it strongly suppresses low amplitude events and enhances high amplitude events.

distribution for $n = -3$ is significantly deviated from an exponential distribution: When compared to $n = 0, -1, -2$, we can see that the population of low-amplitude events (below $1\sigma_r$) are suppressed by roughly 10^{-1}; Enhancement of large-amplitude events is even stronger, where the probability density distribution to encounter a $4\sigma_r$ is increased by at least a factor of 10^2. This indicates that even if $N_B = 33$ is greater than the cluster itself, the major fraction of the neighborhood at $N_B = 33$ is still constituted by the cluster itself.

2.2.3 Block Maxima

Although extreme values drawn from an identically and uncorrelated exponential random field follow a Gumbel distribution in the asymptotic limit, i.e., $(N_B \to \infty)$, it is unclear if this result is still true for a spatially correlated exponential random field with finite N_B. The purpose of this section is to numerically derive the extreme value statistics of block maxima for spatially correlated exponential fields. To this

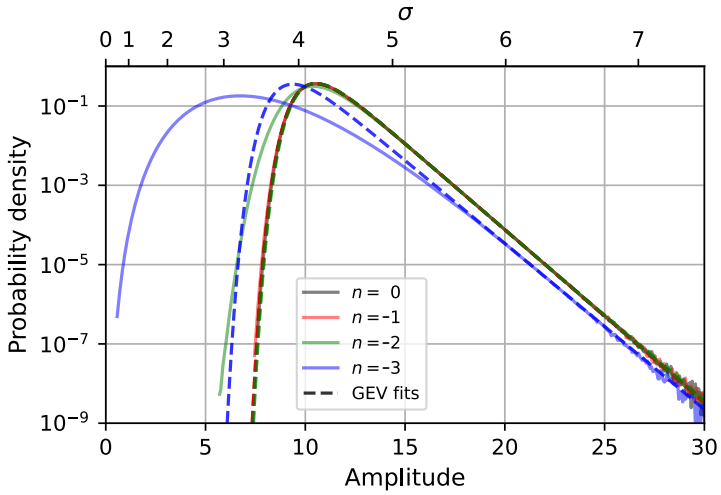

Figure 2.6. Probability density distribution of block maxima obtained by sampling exponential random fields of size $512 \times 512 \times 512$ pixels for spectral index $n = 0, -1, -2, -3$. The dashed line shows the corresponding best-fit generalized extreme value distribution (GEV) with parameters given in Table 2.1.

end, we repeatedly sample the block-maxima from simulations of exponential random fields with spectral index $n = 0, -1, -2, -3$. Each realization is partitioned into non-overlapping cubic blocks with $N_{\rm B} = 33$ containing a list of amplitudes $B = \{E(\boldsymbol{x}_1), E(\boldsymbol{x}_2), ..., E(\boldsymbol{x}_{N_{\rm B}^3})\}$, from which the block maxima is given by $M_{N_{\rm B}} = \max(B)$. For each spectral index n, at least 10^7 exponential random fields are simulated to sample block maxima for constructing the probability density distribution of block maxima, which is shown in Figure 2.6. The solid curves represent the corresponding probability density distribution of block maxima as a function of the amplitude (or rarity σ_r) for different values of n. Of particular interest are the statistics of rare events: the best-fit parameters for the generalized extreme value distribution are inferred from the tail behavior of the numerically obtained block maxima. A comparison between $n = 0$ and $n = -3$ in Figure 2.6 shows that spatial correlations broaden the shape of the probability density distribution of block maxima, which enhances the probability of finding small-amplitude maxima while suppressing those with larger amplitudes. This can be understood from a rather intuitive point of view: For strongly correlated fields, especially for $n = -3$, large amplitude events tend to cluster together. Nevertheless, block maxima can only record the strongest signal within a given block and discard

the rest of the high-amplitude events. This is in strong contrast to the uncorrelated case $n = 0$, where rare events are uniformly distributed in the entire random field, so they are more likely to be sampled individually as block maxima. For this reason, the block maxima tend to underestimate the actual population of large-amplitude events in spatially correlated random fields. This reasoning also explains the enhancement of the low-amplitude population of block maxima for $n = -3$. Spatial correlation leads to the clustering of small-amplitude events to form large under-dense regions, which enhances the likelihood of sampling smaller amplitudes as block maxima when compared to the uncorrelated case $n = 0$.

The key question is whether spatial correlation and finite size can significantly alter the tail properties of the block maxima distribution. Although spatial correlation has significantly broadened the probability density distribution of block maxima, the tail behaviors beyond the $6\sigma_r$ level show a similar statistical properties across all spectral indices considered. Specifically, the tails decay exponentially at the same rate characterized by the parallel slopes on the logarithmic scale in Figure 2.6. This behavior arises because exceedingly rare events occur only once and at most twice per simulation. Again, even if strong spatial correlation enhances the overall population of rare events (See Figure 2.5), only the maxima signal is recorded as a block maximum. So even for correlated fields, rare events beyond $6\sigma_r$ are effectively sampled in a statistically independent way, because they are sampled from different exponential field simulations[5]. As a result, the tails of spatially correlated fields resemble the characteristic form of the Gumbel distribution (See best fit parameters in Table 2.1), with the location parameter μ being the only parameter sensitive to the changes in spectral indices n. Accordingly, we conclude from Figure 2.6 that the tail behavior of extreme values is insensitive to spatial correlation when extreme values are sampled by block maxima with a block size comparable with its correlation length.

[5]A natural question that follows is whether the independent sampling process of rare events is realistic in the cosmological context. Suppose each random field is interpreted as a finite causal region of the sky, then different realizations would correspond to causally disconnected patches. This means that extremely rare overdensities in the early Universe are expected to follow a Gumbel distribution, regardless of whether the underlying primordial fluctuations are Gaussian or exponential. This interpretation can be further improved by replacing the power spectrum $P(k)$ with the actual matter power spectrum. A more detailed discussion of this point is provided in the Outlook of this thesis.

n	μ	σ	ζ
0	10.52	1.00	-9.84×10^{-5}
-1	10.51	1.00	-3.27×10^{-4}
-2	10.54	0.99	9.86×10^{-4}
-3	9.36	1.04	4.50×10^{-4}

Table 2.1. Best fit parameters for the extreme value distribution by fitting the tail behavior of the probability density distribution of block maxima of exponential random field in Figure 2.2. Here, $n = 0, -1, -2, -3$ is the spectra index of the power spectra, $\mu \in (-\infty, \infty)$ is the location parameter, $\zeta \in (-\infty, \infty)$ is the shape parameter, $\sigma > 0$ is the scale parameter, and $\mu, \zeta, \sigma \in \mathbb{R}$. Note that $\zeta \approx 0$ for all n. This means the tail behavior for spatially correlated exponential random field reduces to the Gumbel distribution as in the uncorrelated case.

2.3 Non-Sphericity

2.3.1 Preliminary: Principal Component Analysis

Spatial clustering of large peaks generated by random fields plays an important role in many astrophysical or cosmological settings. Depending on the specific type of random field, clustering can emerge with various sizes and shapes due to the strength of its spatial correlation. In this last section, we propose the use of weighted principal component analysis for measuring sphericity and the shape of a cluster, and demonstrate how rare events (of $\geq 6\sigma_r$) with various spectral indices n can influence these characteristics.

To understand how weighted principal component analysis can quantify the level of sphericity and shape of a cluster, it is useful to recall the basic idea of principal component analysis [92, 93].

Suppose we have N_{obs} observations and each observation has N_{feat} features, then each observation (data point) is given by a point $\boldsymbol{p} \in \mathbb{R}^{N_{\text{feat}}}$. The purpose of principal component analysis is to perform an orthonormal linear transformation to bring the set of bases of $\mathbb{R}^{N_{\text{feat}}}$ (features of the data) into a new set of bases that exhibits the largest variance of the distribution of data points. The basis vector that captures the greatest variance of the data is known as the first principal component; similarly, the second to the largest remaining variance that is orthogonal to the first is the second principal component, and so on.

Let $\boldsymbol{X}$ be a $N_{\text{feat}} \times N_{\text{obs}}$ matrix so each column describes an observation with respect to a set of measurements and each row describes a particular feature across all

observations. The purpose of principal component analysis is to find a decomposition of the data matrix by $\boldsymbol{X} = \boldsymbol{PC}$, for $\boldsymbol{P}$ is a $N_{\text{feat}} \times N_{\text{pc}}$ principle components matrix and $\boldsymbol{C}$ is the $N_{\text{pc}} \times N_{\text{obs}}$ covariance matrix , with N_{pc} being the number of principle components, so that Σ is a diagonal matrix given by

$$\boldsymbol{\Sigma} = \boldsymbol{P}^{\mathrm{T}} \boldsymbol{X} \boldsymbol{X}^{\mathrm{T}} \boldsymbol{P}, \tag{2.18}$$

with diagonal components of $\boldsymbol{\Sigma}$ is ordered in magnitude $|\Sigma_{ii}| \geq |\Sigma_{jj}|$ for all $i \leq j$. In other words, $\boldsymbol{P}$ is the orthonormal transformation that maximizes the variance within Σ and minimizes the off-diagonal component.

The method to achieve this purpose is mostly performed via singular value decomposition of the data matrix: $\boldsymbol{X} = \boldsymbol{PDV}^{\mathrm{T}}$, so that $\boldsymbol{C} = \boldsymbol{DV}^{\mathrm{T}}$ for $\boldsymbol{V}$ is an orthogonal matrices and $|D_{ii}| \leq |D_{jj}|$, $\forall\, i \leq j$. Inserting the singular value decomposition into (2.18), this identifies $\boldsymbol{\Sigma}$ with $\boldsymbol{D}$ by $\boldsymbol{\Sigma} = \boldsymbol{DD}^{\mathrm{T}}$. The diagonal components $\boldsymbol{D}$ encode the geometrical information of how the data are distributed in the N_{feat} dimensional space. Suppose $\Sigma_{ii} = \Sigma_{jj}$ for all i, j, then the variance of all principal components is the same, which means that the data is a N_{feat}-ball within the N_{feat} dimensional space.

2.3.2 Weighted Principal Component Analysis

While principal component analysis works generally for data analysis whose sole purpose is mostly dimensionality reduction, it is inapplicable to fields because it assumes identical weighting to each data point and its features. Scalar fields, on the other hand, assign different values to every point in space, which have physical meaning, such as density or temperature. So principal component analysis works for fields only if a threshold value is imposed to discard field values below the threshold and equalize those that are above. However, this introduces the threshold value as a hyperparameter and discards all quantitative information of the field values that could dominantly dictate the level of sphericity being measured, if the field values have a physical meaning such as matter density.

Therefore, principal component analysis is insufficient to deal with fields where the field amplitudes are indispensable information. The weighted principal component analysis can circumvent this problem by allowing the assignment of different weights to various observations and features. In the context of fields, weighted principal

component analysis allows us to incorporate the field values as weightings. Specifically, weighted principle component analysis minimize the χ^2 value [94]:

$$\chi^2 = W^{ij}\left(X_{ij} - P_i{}^k C_{kj}\right)^2 \tag{2.19}$$

For random fields, $\boldsymbol{X} = [\boldsymbol{x}_1, ..., \boldsymbol{x}_{N_B}]$ is the grid matrix, with $\boldsymbol{x}_i \equiv [x_i, y_i, z_i]^{\mathrm{T}}$, for $i \in [0, N_B]$ and $N_B \in \mathbb{N}$ is the total number of grid points within the neighborhood of a rare event. Since there is no reason to treat the field values along a specific direction differently, we weight the spatial coordinate equally by the field amplitude at a given position. For this reason, the weighting matrix $\boldsymbol{W}$ is

$$\boldsymbol{W} \equiv \frac{[F(\boldsymbol{x}_1)\mathbb{I}_3, ..., F(x_B)\mathbb{I}_3]}{\sum_i F(\boldsymbol{x}_i)} \tag{2.20}$$

where $\mathbb{I} \equiv [1, 1, 1]^{\mathrm{T}}$. Given $\boldsymbol{W}$ and $\boldsymbol{X}$, χ^2 is minimized by fitting the coefficient matrix $\boldsymbol{C}$ with the principal component matrix $\boldsymbol{P}$. This means that the rows and columns of $\boldsymbol{P}$ correspond to spatial coordinates and principal components, respectively, while the rows and columns of $\boldsymbol{C}$ correspond to principal components and grid points, respectively. Again, the principal components can be diagonalized into the distribution-variance matrix $\Sigma = \boldsymbol{C}\boldsymbol{C}^{\mathrm{T}}$ where $\Sigma_i \geq \Sigma_{i+1}$, $\forall i \in \mathbb{N}$. As a result, using the diagonal elements of the distribution variance Σ, we can quantify the level of sphericity of the random field within a block by measuring the loss of isotropy of the field. It is important to note that weighted principal component analysis is sensitive only to non-sphericity by detecting anisotropy, but it cannot distinguish between isotropy and perfectly spherical distributions. Now, to quantitatively measure anisotropy, we define the ratio between distribution variance $\Sigma_{31} \equiv \Sigma_3/\Sigma_1$, which equals to unity $\Sigma_{31} = 1$ for an isotopically distributed field and $\Sigma_{31} < 1$ in the existence of anisotropy. Together with the ratio $\Sigma_{32} \equiv \Sigma_3/\Sigma_2$., the cluster shape can also be specified: If $\Sigma_{32} = 1$ but $\Sigma_{31} < 1$, the cluster shape is approximately ellipsoidal, whereas for $\Sigma_{32} \sim \Sigma_{31}$ and $\Sigma_{31} < 1$, the cluster forms a circular disk shape.

The numerical implementation of this method is shown in Figure 2.7. Let $\sigma^2(\Sigma_{ij}) \equiv \langle \Sigma_{ij} - \langle \Sigma_{ij} \rangle_N \rangle_N^2$ for $i, j = 1, 2, 3$, and $\langle \cdot \rangle_N$ is the ensemble averages across N realization, we can see that $\sigma(\Sigma_{31})$ and $\sigma(\Sigma_{32})$ for $n = 0$ are being the

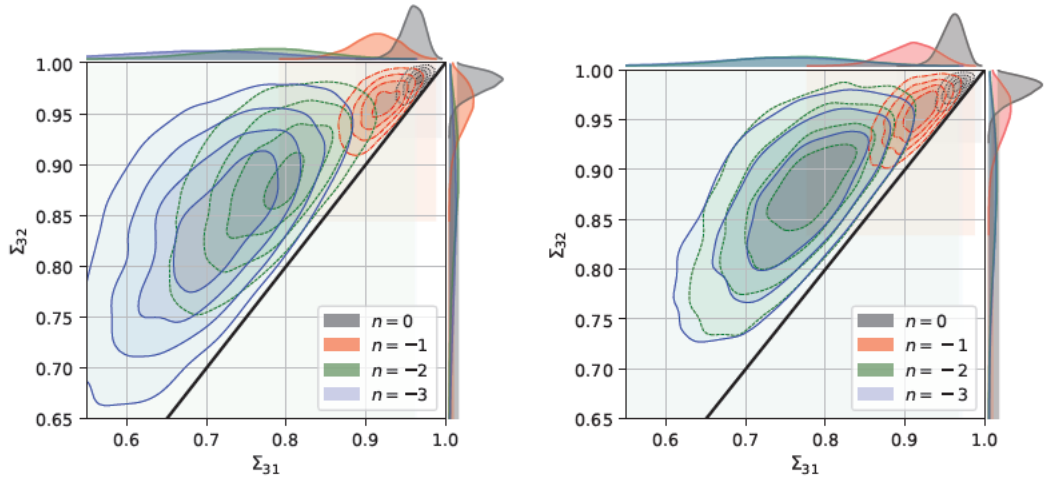

Figure 2.7. Ratio of weighted principal components Σ_{32} against Σ_{31} obtained from sampling $\sim 10^5$ exponential (left) and Gaussian (right) random field that contains at least one extreme-value event of 6 sigma rarity. The black straight line marks $\Sigma_{31} = \Sigma_{32}$. Note that the differences for $n = -2$ and $n = -3$ become substantial because the spatial correlations are strong enough to form clusters at these spectra indices.

least across over all n (gray region in Figure 2.7), with a mean value closest to unity $\langle\Sigma_{31}\rangle_N \sim \langle\Sigma_{32}\rangle_N \sim 1$, which indicates that $\langle\Sigma_3\rangle_N \sim \langle\Sigma_2\rangle_N \sim \langle\Sigma_1\rangle_N$. However, notice that $\sigma(\Sigma_{31}) \sim \sigma(\Sigma_{32}) \neq 0$ and $\langle\Sigma_i\rangle \neq 1$ for $i = 1, 2, 3$, even though a spatially uncorrelated field is homogeneous and isotropic by construction. This is because perfect isotropy measured using weighted principal component analysis is achievable only if there are infinitely many grid points, i.e. $N_B \to \infty$. Otherwise, for a finite block size $N_B \equiv 33$, $\langle\Sigma_{31}\rangle_N$ and $\langle\Sigma_{32}\rangle_N$ and their variance will always be subject to statistical fluctuation inversely proportional to N_B. For this reason, the case $n = 0$ is the reference point of isotropy achievable for any finite N_B.

Using $n = 0$ as a reference, Figure 2.7 shows that anisotropy begins to develop as n decreases. Especially the variance in anisotropy and shape measured in terms of $\sigma(\Sigma_{31})$ and $\sigma(\Sigma_{32})$ reaches its maximum for $n = -3$ for clusters containing a rare event of $\geq 6\sigma_r$ in the center. The increase in variance $\sigma(\Sigma_{31})$ and $\sigma(\Sigma_{32})$ reflects a greater diversity of cluster shapes, which ranges from an elongated shape ($\Sigma_{32} \sim 1$ and $\Sigma_{31} < 1$), flattened disk shapes ($\Sigma_{32} \sim \Sigma_{31}$ and $\Sigma_{31} < 1$), and all possible shapes in between.

Finally, to isolate the effect of the tail contribution from that of the spatial correlations, we have also performed simulations of Gaussian random fields with the same set of power spectra as for exponential fields (see the two panels of Fig. 2.7 for a direct comparison). Our results show that non-Gaussianity amplifies the degree of non-sphericity generated by spatial correlation and produces a broader variety of cluster shapes. For $n = -2$ and $n = -3$, where large spatial clusters are formed, the exponential tails in the exponential random field enhance the degree of spatial anisotropies, even though the underlying Gaussian and exponential random fields share the same power spectra by construction via (2.14). Technically, this occurs because the non-sphericity measure (2.19) weights the amplitudes of the random field within each block. In the exponential case, the existence of a heavy tail implies a larger variation in amplitude. This means that the presence of an at least $6\sigma_r$ within a cluster can significantly deform the variance Σ_{ii} for $i = 1, 2, 3$, so that Σ_{13} and Σ_{23} are more unstable when compared to the Gaussian case.

2.4 Conclusion

In this chapter, we analyzed how rare events influence clustering and the development of non-sphericity related to spatial correlation, with a particular focus on exponential random fields. For each spectra index of interest, we generated at least 10^7 numerical simulations of exponential random fields, which allows us to accurately resolve the extreme value statistics up to the 7.5 sigma level (which corresponds to a probability of 1 in 10^{13}). In the context of extreme-value theory, we developed a statistical approach that incorporates spatial correlation to determine the necessary lower bound of block size for sampling local, which extends the conventional notion of peaks to describe peaks in a discrete random field. Then, we showed that rare events in spatially-correlated exponential random fields follow the generalized extreme-value distributions (Figure 2.6). In particular, the tail behaviors of the extreme value distribution converge to the same family of extreme-value distributions as in their spatial uncorrelated case, which is the Gumbel distribution for an exponential field. More generally, this suggests that at least the Gumbel distribution can be extended to describe a sequence of random events that are identical but not independently distributed in non-asymptotic models, provided that the correlation length is a well-defined notion to quantify the statistical dependence between the random events. Finally, we proposed weighted principal component analysis as a quantitative measure of how spatial correlation could induce spatial anisotropy and non-sphericity of clusters. We compared the Gaussian and exponential random fields with strong spatial correlations ($n = -2, -3$) and found that the anisotropic effects are significantly stronger in the exponential fields (See Figure 2.7). In the cosmological context, this suggests that the neighborhood of overdensities can develop anisotropic features sensitive to both the tail behavior and the two-point statistics of the underlying density field. It remains a curious question whether such anisotropies could influence the ensemble variance of angular momentum in their final collapse structures. If that is possible, then measurement of this variance may, in turn, reveal features of clustering and tail behavior of the primordial overdensities in the early Universe.

Chapter 3

Statistics of Pressure and Matter on the Large-Scale Structures of the Universe

The results presented in this chapter are based on an ongoing collaborative work with Klaus Dolag and Eiichiro Komatsu. The manuscript is currently under preparation and to submitted to the Physical Review D.

3.1 Introduction

Primordial overdensities in the early universe provide the earliest set of regions which collapsed at a later time into bounded structures that could approximate as halos [45, 47, 76, 95–98]. Since gravitational collapses are nonlinear processes, the kinetic energy of the freely falling particles is partially thermalized through shock heating and turbulent dissipation [99–109]. This results in the hot electron gas in the galaxy clusters and groups that can induce spectral distortions of the Cosmic Microwave Background (CMB) through inverse Compton scattering of the CMB photons, which is known as the thermal Sunyaev–Zel'dovich effect. This produces the second anisotropy in the temperature of the CMB, with its magnitude proportional to the pressure of the hot electron gas integrated along the line of sight [110–116]. So using the amplitude of the thermal Sunyaev–Zel'dovich effect and thermodynamic relations, one can infer the thermal energy content of the large-scale structure, and their cross-correlation with other tracers of the matter distribution allows tomographic reconstruction of the thermal history and the evolution of large-scale structures, and thereby indirectly, also constrain the statistics of primordial density fluctuations [117–129].

Of course, there are many nonlinear baryonic processes, such as radiative cooling, star formation, and active galactic feedback, that can spatially redistribute thermal energy and pressure, so their spatial fluctuation does not necessarily trace the matter density

fluctuation. These effects, however, dominate only on small scales within individual halos [47, 130]. On sufficiently large scales, e.g. $\gtrapprox 200\mathrm{Mpc}/h$, structure formation is dominated mostly by gravitational processes, and thermal pressure integrated over each halo is expected to scale with halo mass by a relation given by the virial theorem. From the linear perturbation theory, this correlation is expected to improve at an increasingly large scale. Nevertheless, recent simulations have shown that an unexpected decorrelation between pressure and matter distribution at scales larger than roughly ($k \lesssim 0.02\, h\mathrm{Mpc}^{-1}$), with a particularly significant effect in the low redshift universe [128]. So the theoretical expectation of linear bias theory seems to break down in practice at precisely the scales where it is most reliable.

The purpose of this chapter is to identify the origin of such decorrelation between pressure and matter distribution on large scales. By analyzing the simulation data from `Magenticum`[1], we first investigate to what extent the pressure-matter decorrelation occurs on large scales, and how it depends on redshifts. We will demonstrate that such decorrelation does not imply the breakdown of linear bias theory. But rather, pressure-matter decorrelation can be accurately predicted from the halo model on large scales as one-halo contributions from the pressure distribution that acts as a stochastic noise. While it can be demonstrated that this effect originates from the halo assembly histories and an effective halo model can provide an even more accurate description of the decorrelation on large scales, the discussion of the last part is beyond the scope of this chapter.

[1]The `Magneticum` is a hydrodynamical, cosmological simulation suite that follows the formation of cosmological structures and takes into account a wide range of physical processes (See **[131]** for an excellent recent review). The simulations are performed with an advanced version of the `Gadget-3` code [132, 133], which uses an entropy-conserving formulation of smoothed particle hydrodynamics (SPH) [134]. The cosmological model follows the standard Λ cold dark matter cosmology with the WMAP7 results [135], for a flat universe with a total matter density $\Omega_m = 0.272$ (16.8% baryons), a cosmological constant $\Lambda_0 = 0.728$, a Hubble constant $H_0 = 70.4\,\mathrm{km\,s^{-1}Mpc^{-1}}$, an index of the primordial power spectrum $n_s = 0.963$ and an overall normalization of the power spectrum $\sigma_8 = 0.809$. The simulation suit accommodates many physical processes, such as radiative cooling and star formation [136], active galactic feedback [137–140], chemical evolution [141–143], and etc. More details can be found in previous works using the `Magneticum` simulation [127, 128, 144–161]. Of all available volumes, we will focus on analyzing the `Box0` in `Magneticum` since `Box0` runs the largest scales of cosmological simulation available to date, with the length of each side is $2688\,\mathrm{Mpc}/h$ and the number of particles set to 4536^3, which is the most relevant for our purpose.

3.2 Statistics of Gas Pressure

In order to investigate the origin of the observed large-scale pressure-matter decorrelation, we begin with the formal relation between pressure fluctuation and matter fluctuations on large scales. Let $\rho(\boldsymbol{x};z)$ and $\mathcal{P}(\boldsymbol{x};z)$ be the matter density and pressure field respectively, their fluctuation is a dimensionless field defined by $\delta\rho(\boldsymbol{x};z)=\rho(\boldsymbol{x};z)/\bar{\rho}(z)-1$ and $\delta\mathcal{P}(\boldsymbol{x};z)=\mathcal{P}(\boldsymbol{x};z)/\bar{\mathcal{P}}(z)-1$ for $\bar{\rho}(z)$ and $\bar{\mathcal{P}}(z)$ are the homogeneous and isotropic redshift z dependent background value. Generally, the local pressure fields is a functional of local observables $\mathcal{O}\in\mathcal{A}$ that takes the following covariant form

$$\delta\mathcal{P}(\boldsymbol{x};z)=\mathcal{K}^{(0)}(\boldsymbol{x};z)+\sum_{\mathcal{O}\in\mathcal{A}}\left(\int_{\Sigma_t}\mathrm{d}\mu(\boldsymbol{y})\;\delta\mathcal{O}(\boldsymbol{y})\mathcal{K}^{(1)}(\boldsymbol{x},\boldsymbol{y};z)\right. \tag{3.1}$$
$$\left.+\int_{\Sigma_t}\mathrm{d}\mu(\boldsymbol{y}_1)\,\mathrm{d}\mu(\boldsymbol{y}_2)\,\delta\mathcal{O}(\boldsymbol{y}_1)\delta\mathcal{O}(\boldsymbol{y}_2)\mathcal{K}^{(2)}(\boldsymbol{x},\boldsymbol{y}_1,\boldsymbol{y}_2;z)+\cdots\right)$$

where $\mathrm{d}\mu(\boldsymbol{y})$ is the covariant measure on the hypersurface Σ_t for all time t in an interval $I\in\mathbb{R}$. In this form, $\delta\mathcal{P}(\boldsymbol{x};z)$ encompass all possible nonlocal contribution prescribed by the n-point kernel functions $\mathcal{K}^{(n)}(\boldsymbol{x},\boldsymbol{y}_1,\boldsymbol{y}_2,...,\boldsymbol{y}_{n-1};z)\in\mathcal{C}_{\mathrm{c}}^{\infty}(\mathbb{R})$ within some neighborhood that was in causal contact with $\delta\mathcal{P}(\boldsymbol{x},z)$. The local contribution $\mathcal{K}^{(0)}\in\mathbb{R}$ represents the remaining stochastic scatters of $\delta\mathcal{P}$ that are irrelevant to the set of observables we have chosen $\mathcal{O}\in\mathcal{A}$. While $\delta\mathcal{P}$ is generally a functional power series of $\delta\mathcal{O}$, higher orders of $\delta\mathcal{O}$ concern only nonlinear structures at smaller scales within individual halos, which becomes negligible on large scales [126–128]. Since cosmology at large scale is well approximated by the Friedmann universe, spatial isometry allows us to express inhomogeneous spatial perturbations in the Fourier space. The momentum space representation is crucial because it allows us to perform the separation of scale effectively.

Let us consider the small $|\boldsymbol{k}|$ limit, the general expression of the pressure functions up to $\mathcal{O}(\delta\rho(\boldsymbol{k}))$ in the momentum space becomes

$$\lim_{k\to 0}\delta\mathcal{P}(\boldsymbol{k};z)\approx\mathcal{K}^{(1)}(\boldsymbol{k};z)\delta\rho(\boldsymbol{k};z)+\epsilon(\boldsymbol{k};z) \tag{3.2}$$

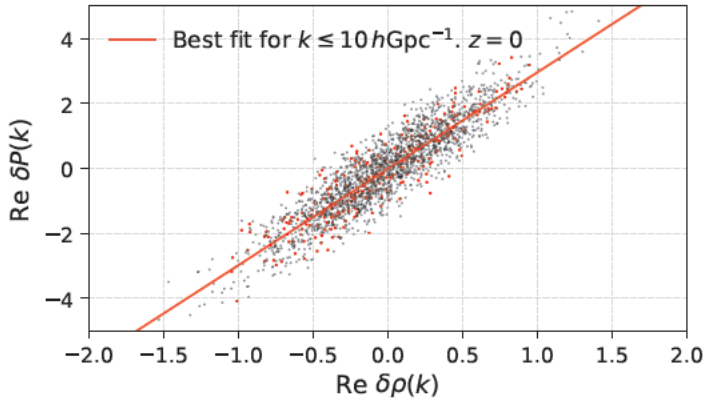

Figure 3.1. Distribution of Fourier amplitudes scatters Re $\delta\mathcal{P}(\boldsymbol{k})$ against Re $\delta\rho(\boldsymbol{k})$ calculated from the simulation data of `Magneticum Box0` at redshift $z = 0$. Each dot corresponds to the Fourier amplitude at a given value of $\boldsymbol{k}$. The red dots, in particular, are Fourier amplitudes for all $\boldsymbol{k}$ with $k \leq 10\,h\mathrm{Gpc}^{-1}$; while the black dots are Fourier amplitudes for all $\boldsymbol{k}$ with $k \in (10, 20]\,h\mathrm{Gpc}^{-1}$. The red line corresponds to the linear fit of the red scatter. This gives a linear relation between $\delta\rho(\boldsymbol{k})$ and $\delta\mathcal{P}(\boldsymbol{k})$ by $\delta\mathcal{P} = b_y(0)\delta\rho + \epsilon$ with best fit parameters $b_y(0) = 2.98$ and $\epsilon = -0.012$. As we will see later in Figure 3.3, $b_y(0)$ is the linear bias that has no k dependence. This explains why $b_y(0)$ agrees very well with $b_y(z)$ at $z = 0$ in Figure 3.3.

where the approximation is taken by discarding all higher orders of $\delta\rho$ at small $|\boldsymbol{k}|$. The function $\mathcal{K}^{(1)}(\boldsymbol{k}; z) \in \mathcal{C}_c^\infty(\mathbb{R})$ is the Fourier amplitude of $\mathcal{K}^{(1)}(\boldsymbol{x}, \boldsymbol{y}; z)$, and the reality of $\mathcal{K}^{(1)}(k; z)$ follows from the reality condition of the two point correlation function of $\delta\mathcal{P}(\boldsymbol{x}; z)$: $\zeta(\boldsymbol{r}) = \zeta^*(\boldsymbol{r}) \in \mathbb{R}$. The function $\epsilon(\boldsymbol{k}; z)$ is a stochastic noise term composed of the Fourier amplitude of $\mathcal{K}^{(0)}$ and include all contributions from the rest of all $\mathcal{O} \in \mathcal{A}$ excluding $\delta\rho$, which therefore, represent the stochastic scatters of the pressure fluctuations. The quality of the statement (3.2) regarding the linearly dependence between $\delta\mathcal{P}(\boldsymbol{k}; z)$ and $\delta\rho(\boldsymbol{k}; z)$ is evaluated in Figure 3.1 and Figure 3.2 from `Magneticum Box0`. First, Figure 3.1 illustrate the distribution of the Fourier amplitudes Re $\delta\mathcal{P}(\boldsymbol{k}; z)$ against Re $\delta\rho(\boldsymbol{k}; z)$ at $z = 0$ for all $|\boldsymbol{k}| \leq 10h\mathrm{Gpc}^{-1}$, which scatters around the linear best fit line due to the stochastic term ϵ. Then, Figure 3.2 evaluates the quality of the linear approximation in (3.2), which shows a relatively high R^2 value (> 0.82 for all redshifts) for the linear fit, and a negligible partial R^2 value is negligible for all redshifts (less than 2%). This means that the linear model can explain major portions of the Fourier amplitude scatters, meanwhile fitting with

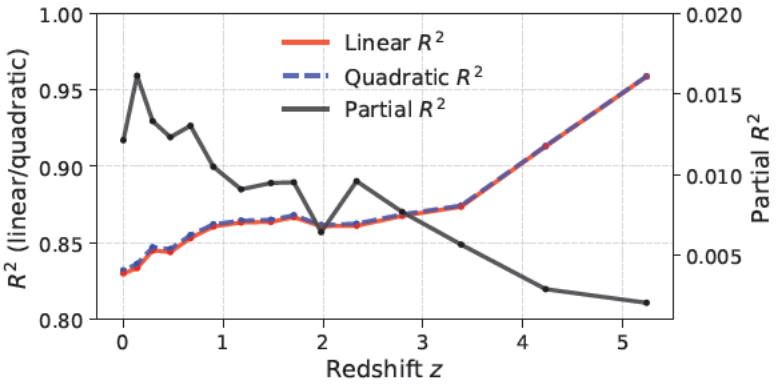

Figure 3.2. R^2 linearity test for the Fourier amplitude scatters $\delta\mathcal{P}(\boldsymbol{k})$ versus $\delta\rho(\boldsymbol{k})$ calculated from the simulation data of `Magneticum Box0` at various redshift z. The red and blue dotted curve corresponds to the R^2 value when fitting the scatters of $\mathrm{Re}\,\delta\mathcal{P}(\boldsymbol{k})$ and $\mathrm{Re}\,\delta\rho(\boldsymbol{k})$ using a linear model and a quadratic model, respectively. The black curve is then the partial R^2, which shows the variance in the scatter that can be captured by the quadratic model but not by the linear model. Since the linear $R^2 > 0.8$ and the partial R^2 is negligible (of order 10^{-2}), we can conclude that $\delta\mathcal{P}$ and $\delta\rho$ have a linear dependence, and this linear model receives no improvement from the quadratic model. Moreover, notice that the R^2 value of both the linear and quadratic models decreases with decreasing redshifts. This indicates that at lower redshifts, the scatter is distributed across a larger variance at any given $\delta\rho$ than in higher redshifts.

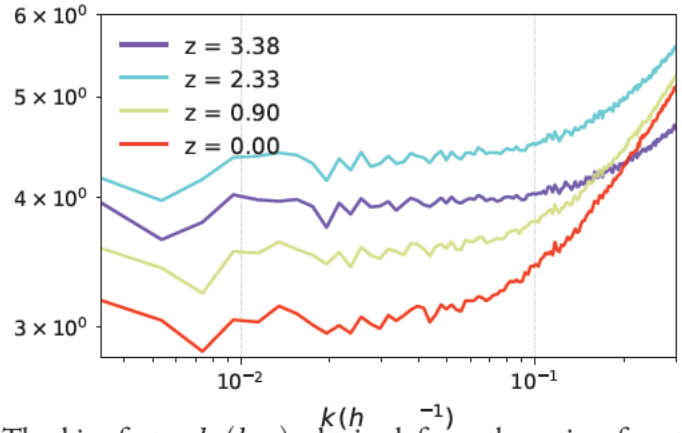

Figure 3.3. The bias factor $b_y(k;z)$ obtained from the ratio of matter density-pressure cross power spectrum and the matter density power spectrum $P_{\mathcal{P}m}(k;z)/P_{mm}(k;z)$ using the `Magneticum Box0` simulation data. As an illustration, we consider redshifts $z = 0, 0.90, 2.33, 3.38$ for brevity. Notice that, on the large scale (small k), $b_y(z)$ has no k dependence but begin to scale with k^2 for $k > 2 \times 10^{-2} h\mathrm{Mpc}^{-1}$.

a quadratic model does not bring any improvement to the linear model. So from the simulation data, the linear relation in the momentum space is accurate to describe the relation between $\delta\mathcal{P}$ and $\delta\rho$ on a large scale by:

$$\lim_{k\to 0} \delta\mathcal{P}_e(\boldsymbol{k}; z) \approx b_y(z)\delta\rho(\boldsymbol{k}; z) + \epsilon(\boldsymbol{k}; z)\,. \tag{3.3}$$

The prefactor $b_y(z) \in \mathbb{R}$ denotes $\mathcal{K}^{(1)}(k; z)$ with a vanishing dependence of k on large scales, with its value given by the limit $b_y(z) \approx \lim_{k\to 0} \mathcal{K}^{(1)}(\boldsymbol{k}; z) \in \mathbb{R}$ [2]. In practice, the function $b(z)$ is the redshift-dependent linear basis associated with the Compton-y parameters in observation. Its k independence on large scales, which can be seen from Figure 3.3, where $b_y(z)$ is calculated directly from the power spectrum of `Magneticum Box0` data via the ratio $b_y(z) = \lim_{k\to 0} P_{pm}(k; z)/P_{mm}(k; z)$, where $P_{mm}(k)$ is the matter auto power spectrum (See Figure 3.9) and $P_{pm}(k)$ is the cross power spectrum between pressure and matter density, and is insensitive to $\epsilon(k; z)$ since $\epsilon(\boldsymbol{k}; z)$ is the residue of $\delta\rho(\boldsymbol{k}; z)$ and thus $\langle\epsilon(\boldsymbol{k}; z)\delta\rho(\boldsymbol{k}; z)\rangle = 0$.

If pressure is an excellent tracer of matter at large scales, then given the tolerance of error $\delta \in \mathbb{R}^+$, we expect $\lim_{k\to 0} |\epsilon(\boldsymbol{k}; z)| \ll \delta$. This can be tested by measuring the correlation between the electron pressure and the matter density fluctuation. To do so, let us consider the cross power spectrum, which is a function of the matter power spectrum and the bias factors:

$$\begin{aligned} P_{\mathcal{P}m}(\boldsymbol{k}, z) &\equiv \langle\delta\mathcal{P}^*(\boldsymbol{k}; z)\delta\rho(\boldsymbol{p}; z)\rangle \\ &= \delta^3(\boldsymbol{p} + \boldsymbol{k}) \left[b_y(z)\, P_{mm}(\boldsymbol{k}; z) + \langle\epsilon^*(\boldsymbol{k}; z)\delta\rho(\boldsymbol{p}; z)\rangle\right] \end{aligned} \tag{3.4}$$

[2] In practice, the numerical value of $\mathcal{K}^{(1)}$ obtained from simulation data can, in general, become complex. This is, however, only due to numerical imprecision in estimating $P_{\mathcal{P}m}(k; z)$, where the imaginary part of the $P_{\mathcal{P}m}$ marks the magnitude of error. This effect is negligible and does not influence our results.

where we have used (3.3). The last term $\langle \epsilon^*(\boldsymbol{k}; z)\delta\rho(\boldsymbol{k}; z)\rangle = 0$ follows from the definition of $\epsilon(\boldsymbol{k}; z)$. Then, to measure the correlation between pressure and matter on large scales, we introduce the correlation parameter:

$$r(k; z) = \frac{P_{\mathcal{P}m}(k; z)}{(P_{\mathcal{P}\mathcal{P}}(k; z)P_{mm}(k; z))^{1/2}} = \left(1 + \frac{1}{b_y^2(k; z)}\frac{P_{\epsilon\epsilon}(k; z)}{P_{mm}(k; z)}\right)^{-1/2} \tag{3.5}$$

where we have considered that the pressure power spectrum $P_{\mathcal{P}\mathcal{P}}(k, z) = b_y^2(k; z)P_{mm}(k; z) + P_{\epsilon\epsilon}(k, z)$, for $P_{\epsilon\epsilon} = |\epsilon^*(\boldsymbol{k}; z)\epsilon(\boldsymbol{k}; z)|$ is the noise power spectrum. So the tolerance of error δ will determine the lower bound of $r(k; z)$; Any decorrelation at large scale between pressure $\delta\mathcal{P}(\boldsymbol{k}; z)$ and matter fluctuations $\delta\rho(\boldsymbol{k}; z)$ is measured by the suppression of $r(k)$ due to $P_{\epsilon\epsilon}(k; z)$. Suppose matter density fluctuation is an accurate linear biased tracer of the gas pressure fluctuations on the largest scale, the correlation parameter $r(k; z)$ of $\delta\mathcal{P}_e(k, z)$ and $\delta\rho_m(k, z)$ is expected to approach unity when k falls below a length scale k_0 which occurs approximately at the turn over point of the matter power spectrum.

This expectation can be verified from Figure 3.4. The solid curve shows the correlation parameter $r(k)$ calculated from the ratio (3.5) using the cross power spectrum $P_{\mathcal{P}m}(k; z)$, the auto power spectrum $P_{\mathcal{P}\mathcal{P}}(k; z)$, and $P_{mm}(k; z)$ from the `Magneticum Box0` simulation at various redshifts. On the other hand, the dashed curve shows the correlation parameters calculated by the same mean but using the halos catalog in the `Magneticum Box0` simulation. In both cases, the pressure-matter correlation improves only until $k \sim 10^{-2}\, h\mathrm{Mpc}^{-1}$, then it begins to decorrelate at a larger scale. This decorrelation is even stronger at lower redshifts, which indicates that the noise power spectrum grows in magnitude when redshift decreases. Since the same effect can be captured from the halo point of view, it suggests that the development of the noise power spectrum is relevant to the formation of virial structures.

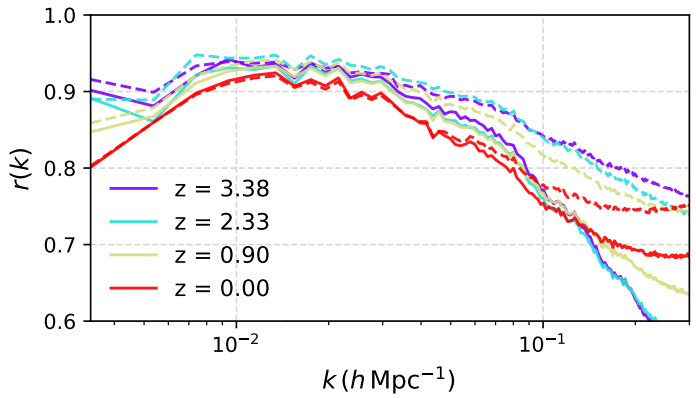

Figure 3.4. Cross correlation parameter $r(k)$ between the gas pressure fluctuation $\delta\mathcal{P}(\boldsymbol{k})$ and matter density fluctuation $\delta\rho(\boldsymbol{k})$ versus the wave vector k on a log scale. The solid lines are $r(k)$ at various redshifts obtained by directly assigning SPH particles into the grid. The dotted lines are also $r(k)$ at various redshifts; they are, however, obtained by assigning halos that are grouped by the Friends-of-Friends algorithm. Since halos at higher redshifts are still very diffuse, the solid and dotted lines are slightly deviated from each other at higher redshifts. Notice that the gas pressure and matter density begin to decorrelate as k goes below $10^{-2}h\text{Mpc}^{-1}$ at low redshift. This is in strong contrast to the expectation that the cross correlation $r(k)$ should continue to improve to an even better degree for $k < 10^{-2}h\text{Mpc}^{-1}$.

3.3 Halo model

If the observed matter-pressure decorrelation can be captured from the halo's perspective, then matter-pressure decorrelation should also be predictable from halo models, where its ambition is to make predictions of astrophysical observables at the large scale based on only the matter density information. In practice, the halo model assumes the matter and pressure distribution can be approximated by the following sum of contributions [128, 162, 163] :

$$\rho_m(\boldsymbol{x}, z) = \sum_{i=0}^{n} N_i m_i \, u_m(\boldsymbol{x} - \boldsymbol{x}_i, z, m_i) \,,$$
$$\mathcal{P}_e(\boldsymbol{x}, z) = \sum_{i=0}^{n} N_i \mathcal{P}(m_i) \, u_{\mathcal{P}}(\boldsymbol{x} - \boldsymbol{x}_i, z, m_i) \,,$$

where m_i is the total mass of the i-th halo, and $n \in \mathbb{N}$ is the total number of halos of the halo catalog in consideration. The variable $N_i \in \mathbb{N}_0 \leq n$ is the occupation

Figure 3.5. Cross correlation parameter $r(k)$ between the gas pressure fluctuation $\delta\mathcal{P}(\boldsymbol{k})$ and matter density fluctuation $\delta\rho(\boldsymbol{k})$ obtained by directly assigning SPH particles into a grid. The figure shows three curves representing different comoving wave-numbers: $k = 2.8, 6.2, 13\,h\mathrm{Gpc}^{-1}$, denoted by red, green, and blue colors respectively. Notice that while there is always some decorrelation between gas pressure and matter density distribution occurs at all redshifts, the effect becomes more significant at lower redshifts, especially for $z < 1$.

number within the i-th volume ΔV_i that the entire space is equally divided into. Here, we follow the usual assumption that ΔV is of comparable order of magnitude as halos, and there exists maximally one halo center per ΔV, and thus $N_i \in \{0, 1\}$ for all $i \in n$. The functions $u_m, u_{\mathcal{P}} \in \mathcal{C}^\infty(\mathbb{R})$ are smooth normalized density profiles which do not necessarily have a compact support. The halo model can definitely generalize to describe a large set of local observables $\mathcal{O} \in \mathcal{A}$ that have an extensive property, provided that they can be determined by halo mass and redshift $\mathcal{O}(\boldsymbol{x}, z, m) \in \mathcal{C}^\infty(\mathbb{R})$. If this holds, in general one could rewrite $\mathcal{O}(\boldsymbol{x}; z) = \sum_{i=0} \mathcal{O}(\boldsymbol{x} - \boldsymbol{x}_i, m_i; z)$ into the following form:

$$\mathcal{O}(\boldsymbol{x}, z) = \sum_{i=0} N_i \mathcal{O}(m_i; z)\, u_{\mathcal{O}}(\boldsymbol{x} - \boldsymbol{x}_i, m_i; z)\,, \tag{3.6}$$

where $\mathcal{O}(m_i; z) = \int_{\Sigma_t} \mathrm{d}^3x\ \mathcal{O}(\boldsymbol{x} - \boldsymbol{x}_i, m_i; z)$[3]. The function $u_{\mathcal{O}} \in \mathcal{C}^\infty(\mathbb{R})$ is the normalized spatial profile inherent from $\mathcal{O}(\boldsymbol{x} - \boldsymbol{x}', m; z)$, and thus its dependency on the local observable $\mathcal{O}$ is denoted by the lower script. In the following, we will assume

[3]Note that here we follow the notation in the literature that the spatial profile $u_{\mathcal{O}}$ is normalized with respect to the spatial integral $\int_{\Sigma_t} \mathrm{d}^3x$. This definition, of course, can generalize further into covariant notations in other applications.

that all quantities are redshift dependent, but we will omit the notations for brevity. The ensemble average of $\langle\mathcal{O}\rangle$ is defined via the usual assumptions of the halo model [47, 162, 163] and rewrite the discrete sum into continuous integration [4]

$$\langle\mathcal{O}(\boldsymbol{x})\rangle = \int_{\mathbb{M}} \mathrm{d}m \, \frac{\mathrm{d}n(m)}{\mathrm{d}m} \, \mathcal{O}(m) \int_{\Sigma_t} \mathrm{d}^3x' \, u_{\mathcal{O}}(\boldsymbol{x}-\boldsymbol{x}', m) = \bar{\mathcal{O}}_0 \,, \tag{3.8}$$

where $\mathbb{M} \in \mathbb{R}$ is the mass range being integrated over, which is usually specified by the support of the halo mass function $\mathrm{d}n/\mathrm{d}m$. On the other hand, the two-point correlation functions of observables $\mathcal{O}$ and $\mathcal{O}'$ are

$$\langle\mathcal{O}(\boldsymbol{x}_1)\mathcal{O}'(\boldsymbol{x}_2)\rangle = \sum_{i,j} \left\langle N_i N_j \mathcal{O}(m_i)\mathcal{O}'(m_j) \, u_{\mathcal{O}}(\boldsymbol{x}_1-\boldsymbol{x}_i, m_i) u_{\mathcal{O}'}(\boldsymbol{x}_2-\boldsymbol{x}_j, m_j)\right\rangle$$

This summation over i and j halos can be divided into two contributions $\langle\mathcal{O}(\boldsymbol{x}_1)\mathcal{O}'(\boldsymbol{x}_2)\rangle = \langle\mathcal{O}(\boldsymbol{x}_1)\mathcal{O}'(\boldsymbol{x}_2)\rangle_{1\mathrm{h}} + \langle\mathcal{O}(\boldsymbol{x}_1)\mathcal{O}'(\boldsymbol{x}_2)\rangle_{2\mathrm{h}}$, which is know as the one-halo term (1h) and two-halo term (2h) respectively. Specifically, the one-halo term collects all terms with $i = j$ that correspond to a contribution from the same halo:

$$\begin{aligned}\langle\mathcal{O}(\boldsymbol{x}_1)\mathcal{O}'(\boldsymbol{x}_2)\rangle_{1\mathrm{h}} &= \sum_{i} \left\langle N_i \mathcal{O}(m_i)\mathcal{O}'(m_i) \, u_{\mathcal{O}}(\boldsymbol{x}_1-\boldsymbol{x}_i, m_i) u_{\mathcal{O}'}(\boldsymbol{x}_2-\boldsymbol{x}_i, m_i)\right\rangle \\ &= \int_{\mathbb{R}} \mathrm{d}m \frac{\mathrm{d}n(m)}{\mathrm{d}m} \mathcal{O}(m)\mathcal{O}'(m) \int_{\Sigma_t} \mathrm{d}^3y \, u_{\mathcal{O}}(\boldsymbol{x}_1-\boldsymbol{y}, m_i) u_{\mathcal{O}'}(\boldsymbol{x}_2-\boldsymbol{y}, m_i)\end{aligned}$$

[4] Also notice that the expression here is not covariant and again following the usual convention in the literature. In the covariant way we can write

$$\langle\mathcal{O}(\boldsymbol{x}; z)\rangle = \int_{\mathbb{R}} \mathrm{d}m \, h^{-1/2}(z) \, \frac{\mathrm{d}m(m; z)}{dm} \mathcal{O}(m; z) \int_{\Sigma_t} \mathrm{d}\mu(x) \, v_{\mathcal{O}}(\boldsymbol{x}-\boldsymbol{x}', m; z) \tag{3.7}$$

where $\mathrm{d}\mu(x)$ is the covariant measure on the hypersurface. This expression reduces to the convention in the literature by rescaling $v_{\mathcal{O}} = u_{\mathcal{O}} h^{-3/2}(z)$ and normalize the profile such that $\int_{\Sigma_t} \mathrm{d}^3x' \, u_{\mathcal{O}}(\boldsymbol{x}-\boldsymbol{x}') = 1$. The same goes for $\mathcal{O}(m; z)$ for rescaling of $\mathcal{O}(m; z) \to \mathcal{O}(m; z)h^{1/2}(z)$.

where we used the fact that $N_i^2 = N_i$ for $N_i \in \{0, 1\}$. On the other hand, the two-halo term collects all the terms with $i \neq j$, which consider contributions from different halos:

$$\begin{aligned}\langle \mathcal{O}(\boldsymbol{x}_1)\mathcal{O}'(\boldsymbol{x}_2)\rangle_{\text{2h}} &= \sum_{i,j} \Big\langle N_i N_j \mathcal{O}(m_i)\mathcal{O}'(m_j)\, u_{\mathcal{O}}(\boldsymbol{x}_1 - \boldsymbol{x}_i, m_i) u_{\mathcal{O}}(\boldsymbol{x}_2 - \boldsymbol{x}_j, m_j)\Big\rangle \\ &= \int_{\mathbb{R}}\int_{\mathbb{R}} \mathrm{d}m_1\, \mathrm{d}m_2\, \frac{\mathrm{d}n(m_1)}{\mathrm{d}m_1}\, \frac{\mathrm{d}n(m_2)}{\mathrm{d}m_2}\, \mathcal{O}(m_1)\mathcal{O}(m_2) \\ &\times \int_{\Sigma_t}\int_{\Sigma_t} \mathrm{d}^3 y_1\, \mathrm{d}^3 y_2\, \left(1 + \zeta_{\text{hh}}(\boldsymbol{y}_1, \boldsymbol{y}_2, m_1, m_2)\right) \\ &\times u_{\mathcal{O}}(\boldsymbol{x}_1 - \boldsymbol{y}_1, m_i)\, u_{\mathcal{O}}(\boldsymbol{x}_2 - \boldsymbol{y}_2, m_2)\end{aligned} \tag{3.9}$$

where $\zeta_{\text{hh}}(\boldsymbol{y}_1, \boldsymbol{y}_2, m_1, m_2)$ is the two-point correlation function between halos of mass m_1 and m_2 independent of $\mathcal{O}$ and $\mathcal{O}'$. Note that the two-halo term is independent of the halo size at a sufficiently large scale, while the one-halo term is not. Intuitively, suppose at a sufficiently large scale $|\boldsymbol{x}_1 - \boldsymbol{x}_2| \gg L$, for L is the length scale of a massive halo, then $u_{\mathcal{O}}$ is roughly the smooth approximation of the Dirac delta distribution i_ϵ at the limit $\epsilon \to 0$. After integrating over the entire hypersurface, the two halo terms depend only on the halo mass function, the halo-halo correlation ζ_{hh}, and the observable $\mathcal{O}(m)$.

In the momentum space, the above statements can be made more precise because the separation of length scale can be taken by considering various limits of k. Consider the momentum space representation of the fluctuation of observable $\delta\mathcal{O} = \mathcal{O}/\mathcal{O}_0 - 1$ for each $\boldsymbol{k}$ that $k \neq 0$: $\delta\mathcal{O}(\boldsymbol{k}) = \sum_{i=0}^{n} \mathcal{O}(m_i)\, u_{\mathcal{O}}(\boldsymbol{k}, m_i)$, where $u_{\mathcal{O}}(\boldsymbol{k}, m_i)$ is the normalized spatial profile in the momentum space. For simplicity, let us assume their spatial profile is spherically symmetric $u_{\mathcal{O}}(|\boldsymbol{x} - \boldsymbol{x}_i|, m_i)$, then $u_{\mathcal{O}}(k, m_i)$ is the Hankel transform of $u_{\mathcal{O}}(r_i, m_i)$ for $r_i = |\boldsymbol{x} - \boldsymbol{x}_i|$:

$$u(k, m_i) = \int_0^R u(r_i, m_i)\, \frac{\sin kr}{kr}\, 4\pi r^2 \mathrm{d}r \tag{3.10}$$

for some upper bound [5] $R \in \mathbb{R}_{>0}$. For typical halos with mass in the range $10^{10} M_\odot - 10^{16} M_\odot$, their normalized halo profiles has vanishing k dependence at large scale limit defined by $k < 0.1h/\mathrm{Mpc}^{-1}$. Therefore, one could always approximate $u(k, m_i) = 1$ at large scale, and the two-halo terms in the large scale limit no longer receive any k dependence from $u_{\mathcal{O}}$.

Let us consider the two-point correlation of the fluctuation observables $\langle \delta\mathcal{O}(\boldsymbol{x}_1)\delta\mathcal{O}'(\boldsymbol{x}_2)\rangle$ in the momentum space, which is a power spectrum composed of the one-halo and two-halo terms: $P_{\delta\mathcal{O}\delta\mathcal{O}'}(k) = P^{\mathrm{1h}}_{\delta\mathcal{O}\delta\mathcal{O}'}(k) + P^{\mathrm{2h}}_{\delta\mathcal{O}\delta\mathcal{O}'}(k)$, where the one-halo term is

$$P^{\mathrm{1h}}_{\delta\mathcal{O}\delta\mathcal{O}'}(k) = \frac{1}{\mathcal{O}_0\mathcal{O}'_0}\int_{\mathbb{M}} \mathrm{d}m\, \frac{\mathrm{d}n(m)}{\mathrm{d}m}\mathcal{O}(m)\mathcal{O}'(m)u_{\mathcal{O}}(k,m)u_{\mathcal{O}'}(k,m) \tag{3.11}$$

and we considered $u^*_{\mathcal{O}}(k,m) = u_{\mathcal{O}}(k,m)$ because $u_{\mathcal{O}}(r_i, m_i) \in \mathbb{R}$ and spherically symmetric. Then, for the two-halo term

$$P^{\mathrm{2h}}_{\delta\mathcal{O}\delta\mathcal{O}'}(k) = \frac{1}{\mathcal{O}_0\mathcal{O}'_0}\int_{\mathbb{M}} \mathrm{d}m_1 \int_{\mathbb{M}} \mathrm{d}m_2\, \frac{\mathrm{d}n_1(m_1)}{\mathrm{d}m_1}\frac{\mathrm{d}n_2(m_2)}{\mathrm{d}m_2}\,\mathcal{O}(m_1)\mathcal{O}'(m_2) \times u_{\mathcal{O}}(k,m_1)\,u_{\mathcal{O}'}(k,m_2)\,P_{\mathrm{hh}}(k,m_1,m_2)\,. \tag{3.12}$$

where $P_{\mathrm{hh}}(k, m_1, m_2)$ is the halo power spectrum corresponding to halos of mass m_1 and m_2. In particular, halos are biased tracers of matter, so P_{hh} can be approximated to be linearly biased towards the linear matter density power spectrum P_{mm} by [47]

$$\zeta_{\mathrm{hh}}(k, m_1, m_2) = b_h(k, m_1)b_h(k, m_2)P_{mm}(k, z) + f_{\mathrm{nl}}(k, m_1, m_2) \tag{3.13}$$

where $b_h(m)$ is the linear bias of halo with mass m, and $f_{\mathrm{nl}}(k, m_1, m_2)$ are nonlinear corrections to the linear power spectrum, which vanish on large scales and thus

[5] The choice of R depends on application. For example, for gas pressure, $R \geq R_{500}$ for R_{500} is defined with respect to 500 times the critical density of the universe ρ_{cri}: $R_{500} = ((3/4\pi)(M/500\rho_{\mathrm{cri}}))^{1/3}$.

$f_{\rm nl}(k, m_1, m_2) = 0$ for our purposes. Then the two-halo power spectrum simplifies into

$$\lim_{k\to 0} P^{\rm 2h}_{\delta\mathcal{O}\delta\mathcal{O}'}(k) = P_{mm}(k) \left(\frac{1}{\mathcal{O}_0}\int_{\mathbb{R}} \mathrm{d}m\ \frac{\mathrm{d}n(m)}{\mathrm{d}m} b_h(m)\mathcal{O}(m)\right) \times \left(\frac{1}{\mathcal{O}'_0}\int_{\mathbb{R}} \mathrm{d}m\ \frac{\mathrm{d}n(m)}{\mathrm{d}m} b_h(m)\mathcal{O}'(m)\right) \tag{3.14}$$

If we consider $\mathcal{O} = \mathcal{O}' = \rho$, then $P^{\rm 2h}_{mm}(k) = P_{mm}(k)$ equals to the matter power spectrum since the matter distribution is by definition unbiased towards itself, so $\rho_0^{-1}\int_{\mathbb{R}} \mathrm{d}m\,(\mathrm{d}n/\mathrm{d}m) b_h(m) = 1$.

While the two-halo term gives a reliable prediction of the linear matter power spectrum on large scales for $\mathcal{O} = \mathcal{O}' = \rho$, the one-halo term gives a non-vanishing local contribution of each halo:

$$\lim_{k\to 0} P^{\rm 1h}_{\delta\mathcal{O}\delta\mathcal{O}'}(k) = \int_{\mathbb{R}} \mathrm{d}m\ \frac{\mathrm{d}n(m)}{\mathrm{d}m}\ \mathcal{O}(m)\mathcal{O}'(m)\,, \tag{3.15}$$

which is a stochastic noise that can eventually dominate over the linear matter power spectrum given by the two-halo term. For the matter power spectrum $\mathcal{O} \equiv \rho$, the standard halo model predicts a one-halo contribution that introduces a scale-independent stochastic component dominating over the two-halo term. This means that at a sufficiently large scale, the halo model prediction becomes inconsistent with the observed linear matter power spectrum. This inconsistency is commonly referred to as the one-halo problem [47, 162], which can be resolved by imposing mass and momentum conservation within the halo model framework. In the context of this work, however, the one-halo term does not constitute a significant source of error; across the range of scales relevant to our analysis, it contributes only approximately 5% of the total matter power spectrum in the scales of consideration.

3.3.1 Stochastic Scatters

So far, we have been considering $\mathcal{O} \in \mathcal{A}$ that is a deterministic function of the matter distribution. This is only true for the matter density since the matter density is a determinsitic function of itself. For other observables, however, they might receive other

nonlocal contributions that are all encompassed in the stochastic noise. In this section, we will incorporate the stochastic component $\epsilon(k;z)$ from (3.2) at large scale into the halo model. Let us consider $\mathcal{O}(\boldsymbol{x}) = \sum_{i=0}^{n} N_i \left(\mathcal{O}(\boldsymbol{x}-\boldsymbol{x}_i, m) + \epsilon^{(\mathcal{O})}(\boldsymbol{x}-\boldsymbol{x}_i, m)\right)$, where $\epsilon_i^{(\mathcal{O})}(\boldsymbol{x}-\boldsymbol{x}_i;z) \in \mathbb{R}$ represents the random stochastic scatters corresponding to the observable $\mathcal{O}$ and the i-th halo. We denote ϵ with m dependence that allows ϵ to be a smooth distribution with statistical properties as a function of m, but again, we are not necessarily restricted to this case. If $\sum_{i=0}^{n} N_i \epsilon_i^{(\mathcal{O})}(\boldsymbol{x}-\boldsymbol{x}_i, m) \neq 0$ has a non-vanishing mean value, then this contribution can be absorbed into $\mathcal{O}$ by rewriting $\epsilon^{(\mathcal{O})}(\boldsymbol{x}-\boldsymbol{x}_i, m_i) = \bar{\epsilon}_i^{(\mathcal{O})}(\boldsymbol{x}-\boldsymbol{x}_i, m_i) + \delta\epsilon_i^{(\mathcal{O})}(\boldsymbol{x}-\boldsymbol{x}_i, m_i)$, such that

$$\mathcal{O}(\boldsymbol{x}) = \sum_{i=0}^{n} N_i \left(\mathcal{O}_{\text{eff}}(\boldsymbol{x}-\boldsymbol{x}_i, m) + \delta\epsilon_i^{(\mathcal{O})}(\boldsymbol{x}-\boldsymbol{x}_i, \mathcal{O}\,|m)\right) \tag{3.16}$$

where $\mathcal{O}_{\text{eff}}(\boldsymbol{x}-\boldsymbol{x}_i, m) = \mathcal{O}(\boldsymbol{x}-\boldsymbol{x}_i, m_i) + \bar{\epsilon}(\boldsymbol{x}-\boldsymbol{x}_i, m_i)$ receives a correction from the mean of the stochastic scatters across all halos within a mass range $[m_i - \delta m/2, m_i + \delta m/2]$. The value of δm depends on the total number of halos n for estimating the distribution of ϵ.

In practice, it is more convenient to rewrite (3.16) in the following form

$$\mathcal{O}(\boldsymbol{x}) = \sum_{i=0}^{n} N_i \mathcal{O}_i(\boldsymbol{x}-\boldsymbol{x}_i, S|m_i) \tag{3.17}$$

where $\mathcal{O}_i(\boldsymbol{x}-\boldsymbol{x}_i, S(\mathcal{O}|m_i))$ is the random variable drawn from the distribution of scatters $S(\mathcal{O}|m_i) \in \mathbb{R}$ with a mean value $\mathcal{O}(m_i)$. For example, suppose $S(\mathcal{O}|m_i) = \delta(\mathcal{O} - \mathcal{O}(m_i))$ is given by the Dirac-delta distribution for all $i \in [0,n]$, then the possible outcome of the random sampling process is deterministically given by $\mathcal{O}(m_i)$ for all $i \in [0,n]$. This is equivalent to the case where there exists no scatter.

Let us show that (3.17) is equivalent to (3.16). By the same procedure, we separate the ensemble average $\langle\mathcal{O}\rangle_S$ with respect to S, and define the fluctuation δo by: $\mathcal{O}(\boldsymbol{x}-$

$\boldsymbol{x}_i, S|m_i) = \langle\mathcal{O}\rangle_S(\boldsymbol{x}-\boldsymbol{x}_i, m_i) + \delta o_i(\boldsymbol{x}-\boldsymbol{x}_i, S|m_i)$, and $\delta\mathcal{O}_i$ has zero mean value. Then (3.17) equals to (3.16) if

$$\langle\mathcal{O}\rangle_S(\boldsymbol{x}-\boldsymbol{x}_i, m_i) = \mathcal{O}_{\text{eff}}(\boldsymbol{x}-\boldsymbol{x}_i, m_i) = \int_{\mathbb{R}} \mathrm{d}\mathcal{O}\ \mathcal{O}(\boldsymbol{x}-\boldsymbol{x}_i, m_i)\, S(\mathcal{O}|m_i)\,, \quad (3.18)$$

$$\delta o_i(\boldsymbol{x}-\boldsymbol{x}_i, S|m_i) = \delta\epsilon_i(\boldsymbol{x}-\boldsymbol{x}_i, \mathcal{O}\,|m)\,. \quad (3.19)$$

As a consistency check, if $S(\mathcal{O}|m_i) = \delta(\mathcal{O}-\mathcal{O}(m_i))$, then we reduce to the case that there is no scatter such that the mean value is deterministic $\mathcal{O}_{\text{eff}}(\boldsymbol{x}-\boldsymbol{x}_i, m_i) = \mathcal{O}(m_i)$ and $\delta\mathcal{O}_i(\boldsymbol{x}-\boldsymbol{x}_i, \delta|m_i) = \delta\epsilon_i(\boldsymbol{x}-\boldsymbol{x}_i, \mathcal{O}\,|m) = 0$ because the variance of the Dirac-delta distribution is strictly zero.

So using (3.17) to represent (3.16), we obtain the ensemble average of $\mathcal{O}$ including the effect of scatters:

$$\langle\langle\mathcal{O}\rangle_S\rangle = \int_{\Sigma_t} \mathrm{d}^3x \int_{\mathbb{M}} \mathrm{d}m\, \frac{\mathrm{d}n(m)}{\mathrm{d}m}\, \langle\mathcal{O}\rangle_S(m) v_{\mathcal{O}}(\boldsymbol{x}-\boldsymbol{x}', m) \equiv \mathcal{O}_0 \quad (3.20)$$

where $v_{\mathcal{O}}(\boldsymbol{x}-\boldsymbol{x}', m)$ is now spatial profile normalized with respect to the spatial average of $\langle\mathcal{O}\rangle_S(m)$ instead of $\mathcal{O}(m)$. As expected, the ensemble average of $\mathcal{O}$ is shifted by a magnitude depending on the mean value of the scatters.

The advantage of using (3.17) is that the contribution of the scatters can be expressed by redefining $\mathcal{O}(m)$ using the ensemble average $\langle\mathcal{O}\rangle_S(m)$. This allows us to directly adopt the effect of scatter into the halo model. Let us consider the fluctuation field $\delta\mathcal{O} = \mathcal{O}/\mathcal{O}_0 - 1$ with $\mathcal{O}_0$ given by (3.20), then the one-halo and two-halo terms receive corrections from scatters as:

$$\begin{aligned}\langle\delta\mathcal{O}(\boldsymbol{x}_1)\delta\mathcal{O}(\boldsymbol{x}_2)\rangle_{\text{1h}} &= \int_{\Sigma_t} \mathrm{d}^3x \int_{\mathbb{R}} \mathrm{d}m\, \frac{\mathrm{d}n(m)}{\mathrm{d}m}\, \langle\mathcal{O}^2\rangle_S(m) \quad (3.21)\\ &\quad\times v_{\mathcal{O}}(\boldsymbol{x}_1-\boldsymbol{x}', m) v_{\mathcal{O}}(\boldsymbol{x}_2-\boldsymbol{x}', m)\\ \langle\delta\mathcal{O}(\boldsymbol{x}_1)\delta\mathcal{O}(\boldsymbol{x}_2)\rangle_{\text{2h}} &= \int_{\mathbb{R}}\int_{\mathbb{R}} \mathrm{d}m_1\, \mathrm{d}m_2\, \frac{\mathrm{d}n(m_1)}{\mathrm{d}m_1}\, \frac{\mathrm{d}n(m_2)}{\mathrm{d}m_2}\, \langle\mathcal{O}\rangle_S(m_1)\langle\mathcal{O}\rangle_S(m_2)\\ &\quad\times \int_{\Sigma_t}\int_{\Sigma_t} \mathrm{d}^3y_1\, \mathrm{d}^3y_2\, (1+\zeta_{\text{hh}}(\boldsymbol{y}_1, \boldsymbol{y}_2, m_1, m_2))\\ &\quad\times v_{\mathcal{O}}(\boldsymbol{x}_1-\boldsymbol{y}_1, m_i)\, v_{\mathcal{O}}(\boldsymbol{x}_2-\boldsymbol{y}_2, m_2) \quad (3.22)\end{aligned}$$

Notice that while the two-halo term depends on the ensemble averages $\langle \mathcal{O} \rangle_S(m)$, the one-halo term now scales with the variance of the scatters, that is $\langle \mathcal{O}^2 \rangle(m)$. Then by the same procedure, the power spectrum at large scale is approximately

$$\lim_{k\to 0} P^{1\mathrm{h}}_{\delta\mathcal{O}\mathcal{O}}(k) = \frac{1}{\mathcal{O}_0^2} \int_{\mathbb{M}} \mathrm{d}m \, \frac{\mathrm{d}n(m)}{\mathrm{d}m} \langle \mathcal{O}^2 \rangle_S(m) \tag{3.23}$$

$$\lim_{k\to 0} P^{2\mathrm{h}}_{\delta\mathcal{O}\delta\mathcal{O}}(k) = P_{mm}(k) \left(\frac{1}{\mathcal{O}_0} \int_{\mathbb{R}} \mathrm{d}m \, \frac{\mathrm{d}n(m)}{\mathrm{d}m} b_h(m) \langle \mathcal{O} \rangle_S(m) \right)^2 \tag{3.24}$$

3.4 Halo model of Gas Pressure

We now apply the halo model to pressure $\mathcal{P}$ and the matter density ρ for modeling their correlation in the large-scale structure of the universe. In particular, consider the volume-integrated pressure (or the thermal energy) $\mathcal{Y} = \int_{\mathbb{V}} \mathrm{d}V \mathcal{P}$ for volume $\mathbb{V} \in \mathbb{R}^3$, the halo model for gas pressure is given by:

$$\mathcal{Y}(\boldsymbol{x}, z) = \sum_i \mathcal{Y}_i(m_i) u_y(\boldsymbol{x} - \boldsymbol{x}_i, m_i) = \int_{\mathbb{M}} \mathrm{d}m \frac{\mathrm{d}n(m)}{\mathrm{d}m} \mathcal{Y}(m) \, u_y(|\boldsymbol{x} - \boldsymbol{x}'|, m) \, .$$

To estimate the normalized spatial profile, consider the fact that the scaled pressure profile can be well approximated with a self-similar profile, $\mathcal{P}(r, M_{500}) = \mathcal{P}_{500}(M_{500}) \; p(x)$, for $p(x)$ being the analytic approximation given by the generalized Navarro-Frenk White (gNFW) pressure profile [47, 164]:

$$p(x) = \frac{\mathcal{P}_0}{(c_{500}x)^\gamma [1 + (c_{500}x)^\alpha]^{(\beta-\gamma)/\alpha}} \tag{3.25}$$

where $x = r/R_{500}$ is the dimensionless radius normalized by R_{500} [6]; the parameters $\alpha = 1.33$, $\beta = 4.13$, $\gamma = 0.31$, $c_{500} = 1.81$, $\mathcal{P}_0 = 6.41$ are the best-fit parameters

[6] which is the radius that marks a total density contrast of 500 times the critical density $\rho_{\mathrm{cri}}(z)$ of the universe, and related to defines the mass $M_{500} = 500\rho_{\mathrm{cri}}(z) \times (4\pi R_{500}^3/3)$

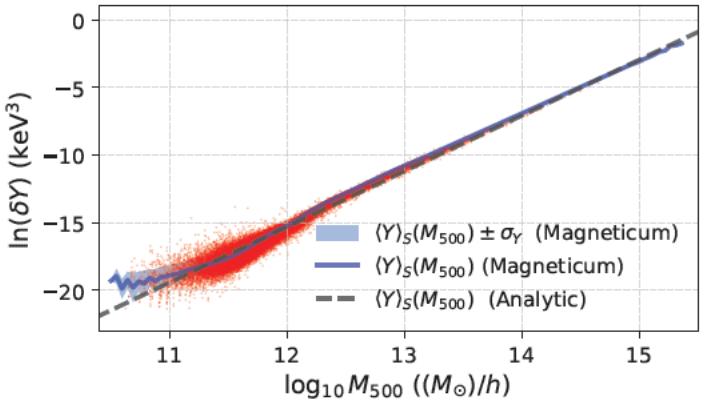

Figure 3.6. Distribution of thermal energy (pressure integrated over volume) scatters as a function of mass. Here we have shown only 4×10^4 scatters from the `Magneticum Box0` data, which is only $\sim 3.4\%$ (randomly selected) from the total number of scatters, and are all denoted by very fine red dots. On the other hand, the blue line and the light blue region represent the mean value and standard deviation, respectively, of the red scatters $\langle y \rangle_S$ within a given mass interval $M_{500} \pm \Delta M$ for $\Delta M \sim 0.05 M_{\odot/h}$. The black dashed line corresponds to the theoretical value calculated using (3.26) from [164] with rescaling $M_{500} \to M_{500}/1.2$ to account for non-thermal pressure [144]. We can see that this correction brings (3.26) is capable of taking into account the effect of scatters in `Magneticum Box0` data.

to the gNFW pressure profile obtained from *Planck* pressure profile [164], with the characteristic pressure $\mathcal{P}_{500}$ scales with the cluster total mass by [164]

$$\mathcal{P}_{500}(M_{500}) = 1.65 \times 10^{-3} E(z)^{8/3} \times \left[\frac{M_{500}}{2 \times 10^{14} h^{-1} M_\odot}\right]^{\alpha+(2/3)} h^2 \mathrm{keVcm}^{-3} \,. \tag{3.26}$$

Formally, the gNFW pressure profile should be equipped with compact support because the gNFW profile only approximates the pressure profile to radii at the scale of R_{500} and does not converge when integrated over the entire space. This can be performed by multiplying $p(x)$ with a smooth approximated characteristic function $f(x) \in \mathcal{C}_c^\infty(\mathbb{R})$ that is $f(x) = 1$ for $x \leq 1$ and $f(x) = 0$ otherwise. This generalize $\mathcal{Y}(M_{500}) \equiv$

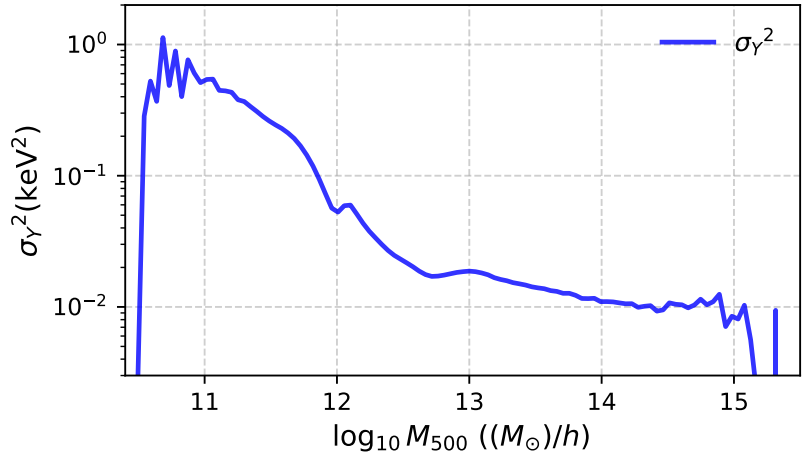

Figure 3.7. Variance of the pressure scatter versus M_{500} in the logarithmic space. Notice that the pressure scatters dominate quite strongly for $M_{500} \leq 11 M_\odot$. Nevertheless, halos with $M_{500} < 10^{11} M_\odot$ have an insignificant contribution to the de-correlation between pressure and matter density. For large halos with $M_{500} \geq 12 M_\odot$, the pressure scatter is suppressed to $\sim 10^{-2}$ so the variance contributions for large halos are also negligible.

$\int_{\mathbb{R}^3} \mathcal{P}(r, M_{500})\, \mathrm{d}V = \int_{\mathbb{V}} \mathcal{P}(r, M_{500})\, \mathrm{d}V$. Then, for each individual halo, we can define

$$\begin{aligned} \mathcal{P}_i(r_i, M_{500}) &= y_i(M_{500})\, (\mathcal{P}_i(r_i, M_{500}) y_i^{-1}(M_{500})) \\ &\equiv y_i(M_{500})\; u_y(r_i, M_{500}) \equiv y_i(r, M_{500}) \end{aligned} \tag{3.27}$$

where in the third equality sign we identified the normalized spatial profile by $u_y(r, M_{500}) = \mathcal{P}(r, M_{500}) y^{-1}(M_{500})$. So that when considering all contributions from all halos:

$$\langle y(r) \rangle = \left\langle \sum_{i=0}^{n} y(M_{500}^{(i)})\, u_y(r_i, M_{500}^{(i)}) \right\rangle = \sum_{i=0}^{n} y(M_{500}^{(i)}) \tag{3.28}$$

What remains to be determined is the halo mass function $\mathrm{d}n(m)/\mathrm{d}m$, here, we use both the empirical model from Tinker et. al. [166] based on WMAP7 cosmology [135] and the halo mass function calculated directly from `Magneticum Box0` simulation data, as shown in Figure 3.8. As a consistency check [166] agree very well with the halo mass function obtained from `Magneticum` within the mass range 10^{12} –

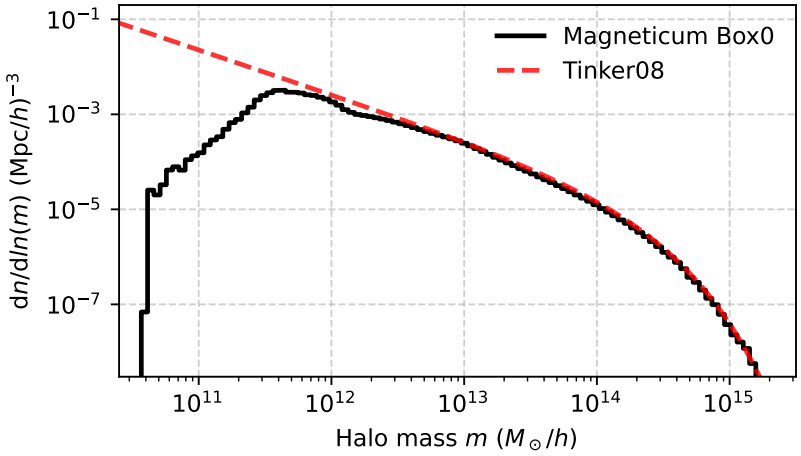

Figure 3.8. Halo mass function within the mass range $10^{10} - 10^{16} h^{-1} M_{\odot}$. The red dotted curve is obtained by using the universal functions in Tinker et. al. (Red dotted); while the black curve is obtained by logarithmically binning the number density of halos with respect to their mass in the `Mangeticum Box0` simulation (Black). Both curves agrees with high accuracy in the range $10^{12} - 10^{15} h^{-1} M_{\odot}$, but the agreement deteriorate for smaller halos. Nevertheless, as we can see later, the discrepancy of the small halo mass has negligible effects on estimating the halo power spectrum.

$10^{15} h^{-1} M_{\odot}$, and begins to deviate from each other for $M < 3 \times 10^{11} h^{-1} M_{\odot}$ and $M > 10^{15} h^{-1} M_{\odot}$. However, since the deviation occurs at small halos, it does not have a noticeable effect in both the one-halo and two-halo terms.

Let us consider the one-halo and two-halo of gas pressure that follows from the previous section:

$$P^{1h}_{\delta y \delta y}(k) = \int_{\mathbb{M}} \mathrm{d}m \, \frac{\mathrm{d}n(m)}{\mathrm{d}m} \, \langle y^2 \rangle_S(m) \, |u_y(k,m)|^2 \tag{3.29}$$

$$P^{2h}_{\delta y \delta y}(k) \approx P_{mm}(k) \left(\int_{\mathbb{M}} \mathrm{d}m \, \frac{\mathrm{d}n(m)}{dm} \, \langle y \rangle_S(m) \, b_h(m) \, u_y(k,m) \right)^2 \tag{3.30}$$

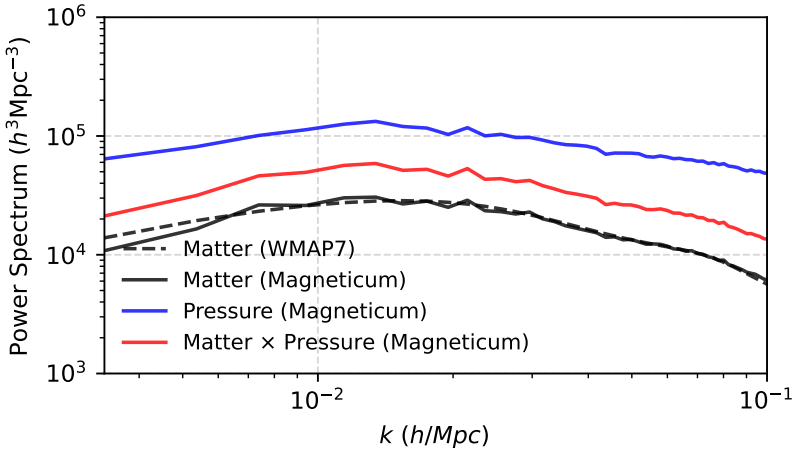

Figure 3.9. Auto power spectrum of matter density (black) and pressure (blue), and cross power spectrum between pressure and matter density (red). The solid curve represents the power spectrum obtained from the `Magneticum box0` data, and the dashed line is the matter power spectrum of WMAP7 obtained from [165] and [135] , which is included for a direct comparison.

where the approximation is taken by assuming a linear bias relation $P_{hh}(k, m_1, m_2) \approx P_{mm}(k) b_h(m_1) b_h(m_2)$; and $\langle y \rangle_S(m)$ is the thermal energy, including the effect of scatters that follows a log-normal distribution:

$$\langle y^n \rangle_S(m) = \int_{-\infty}^{\infty} \mathrm{d}y \; y^n \frac{1}{y \sigma_y(m) \sqrt{2\pi}} \exp\left(- \frac{(\ln y - \ln \bar{y}(m))^2}{2\sigma_y^2(m)} \right) \tag{3.31}$$

where $\sigma_y^2(m)$ and $\ln \bar{y}(m)$ are the variance and the mean of the scatter, respectively. The same holds for the cross-power spectrum between matter density and thermal energy:

$$P^{1h}_{\delta y \delta m}(k) = \int_{\mathbb{M}} \mathrm{d}m \, \frac{\mathrm{d}n(m)}{\mathrm{d}m} \, m \langle y \rangle_S(m) \, u_y(k, m) u_m(k, m) \tag{3.32}$$

$$P^{2h}_{\delta y \delta m}(k) \approx P_{mm}(k) \left(\int_{\mathbb{M}} \mathrm{d}m \, \frac{\mathrm{d}n(m)}{\mathrm{d}m} \, \langle y \rangle_S(m) \, b_h(m) \, u_y(k, m) \right) \times \left(\int_{\mathbb{M}} \mathrm{d}m \, \frac{\mathrm{d}n(m)}{\mathrm{d}m} \, m \, b_h(m) \, u_m(k, m) \right) \tag{3.33}$$

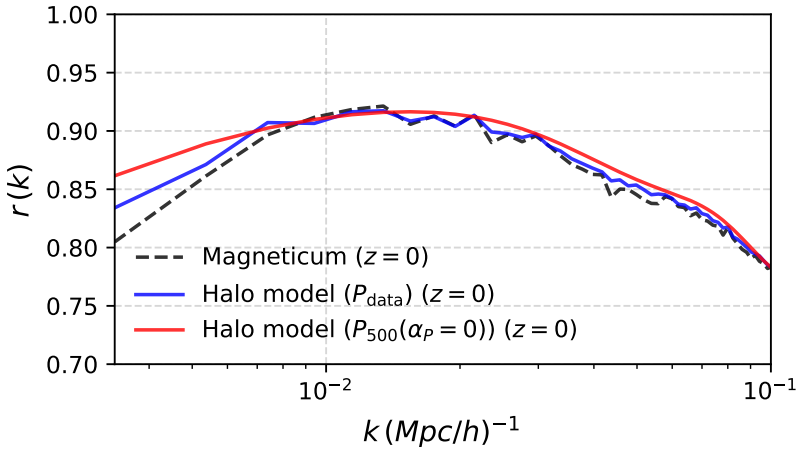

Figure 3.10. Cross correlation parameters $r(k)$ at $z = 0$ obtained from the `Magneticum Box0` and the Halo model. Notice that $r(k)$ largely agree with the `Magneticum` data over a large range of $k \geq 6(\mathrm{Mpc}/h)^{-1}$. There are minor discrepancies at $k < 6(\mathrm{Mpc}/h)^{-1}$, which is suspected to originate from the fact that $r(k)$ at small k is noisy due to a limited small set of points available.

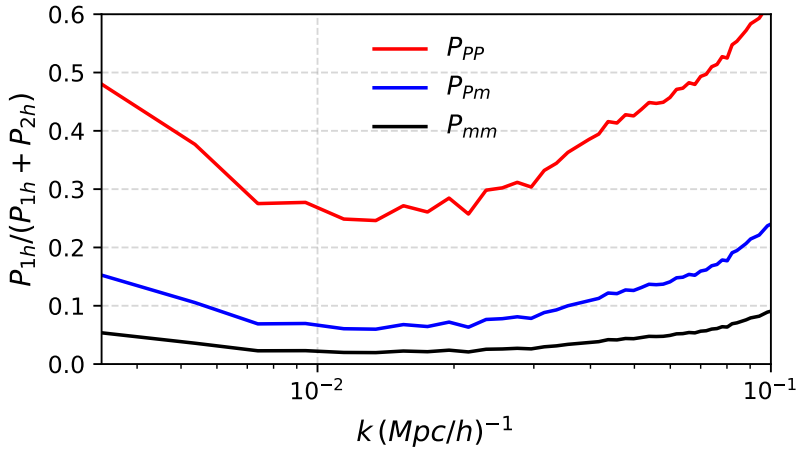

Figure 3.11. Percentage of one halo term constituting the total auto power spectrum. For the matter power spectrum, the one-halo term at small k constitutes of $\sim 5\%$. However, for the pressure power spectrum, the one-halo terms reach $\sim 45\%$ of the total power spectrum.

In the following we will consider $k \leq 10^{-1}(\mathrm{Mpc}/h)^{-1}$ because in this range $u_m \approx u_y \approx 1$. Using the halo mass function from [166] (Figure 3.8) and the halo bias

from [167], we calculated the cross-correlation parameter $r(k)$ using the halo model we described above. The black dotted curve in Figure 3.10 represents $r(k)$ obtained from the auto and cross power spectrum of pressure and material calculated from their spatial distributions within `Magneticum Box0`. The blue curve is the prediction from the halo model, using the matter power spectrum calculated from the spatial distribution of matter in `Magneticum Box0`, and the thermal energy profile obtained from the halo catalog, which is shown in Figure 3.9, 3.6 and 3.7 respectively. On the other hand, the red curve is also the prediction from the halo model without using any information from the `Magneticum Box0`. The matter power spectrum is specified by the WMAP7 cosmology in [135, 165], while the pressure profile follows the best fit parameters provided from *Planck* [164]. We set the phenomenological parameter $\alpha = 0$ so that the integrated pressure is proportional to $M^{5/3}$ simply due to the virial theorem [47]. It also has a better alignment with the actual pressure profile for very massive halos within `Magneticum Box0`, which are the most influential to the value of $r(k)$.

We can see that the halo model predictions resemble with high accuracy of $r(k)$ at $k \geq 0.01\,(\mathrm{Mpc}/h)^{-1}$, with the exception of a slight deviation at the lowest k. To understand this effect, first of all, notice that the suppression in $r(k)$ arises solely from the one-halo contribution of the cross and auto power spectrum of pressure and matter. Specifically, the one-halo term for pressure constitutes almost 50% of the total pressure power spectrum (See Figure 3.11) and it is a pure stochastic shot noise of no k dependence. For this reason, the k dependence of $r(k)$ predicted by the halo model is completely specified by the matter power spectrum. This explains the slight differences between the red and blue curves of $r(k)$ in Figure 3.10, which originates from the discrepancy of the matter power spectrum used for the halo model (See Figure 3.9).

We can see that the correlation parameter $r(k)$ measured from the pressure and matter field (black curve) in `Magneticum` shows a further suppression at small k. This deviation originates from the breakdown of the conventional halo model for describing matter density on a sufficiently large scale. Specifically, although the matter power spectrum is expected to follow a linear power spectrum at low k, conventional halo models ignore mass conservation and retain a spurious one-halo term (See Figure 3.11) in the matter power spectrum at low $k \leq 10^{-2} h\mathrm{Mpc}^{-1}$. So the deviation predicted by the halo model is directly related to the degree to which the matter power spectrum

predicted by the halo model's matter power spectrum deviates from the linear power spectrum, which is approximately 5% as we can see from Figure 3.11. While it is beyond the scope of this chapter, this issue can be resolved by an effective halo model that takes into account mass conservation and results in a vanishing one-halo term for the matter power spectrum on large scales [168].

Chapter 4

Outlook

In this Outlook, we will discuss briefly various ongoing projects that are relevant to previous Chapters of this thesis:

Detectors in Effective Field Theories

The diagnostic framework for quantum field theory in curved spacetime developed in Chapter 1 can be extended further to incorporate realistic detector sensitivity and resolution. The former is relevant to the resolution limit in resolving details finer than a particular length scale (or time scale for temporal resolution), while the latter is related to the sensitivity to differentiate changes in the magnitude of detected signals. It is possible to show that the detector resolution can be included by the same treatment in Chapter 1 by replacing the short distance cutoff that defines (1.16) with the finest resolution scales available to the detector. Detector sensitivity, however, requires further treatment: In the first step, it follows a similar treatment using the geometric criteria (1.18). Specifically, let us consider a stochastic noise background $\mathcal{O}'_0 = \mathcal{O}_{\text{ns}}$ that can be measured with a detector of sensitivity S_r, and let $\langle\mathcal{O}\rangle$ be the expectation value of an observable that is not necessarily detectable if its signal is too weak to be distinguishable from the noise background. Provided that both (1.18) and (1.16) are satisfied, then the quantum observables is measurable if

$$N(\mathcal{O}, \Psi_t; U_0) = \max_{\mathcal{O}\subset\mathcal{A}_0} \sup_{U_0\in\Gamma(\mathcal{C}_t)} |\mathcal{R}_{\text{ns}}(\mathcal{O}, \Psi_t; U_0)| \geq \delta_r \tag{4.1}$$

where δ_r is a signal-to-noise ratio defined in according to the detector sensitivity S_r. Suppose the maximum of the set of physical observables $\mathcal{O}$ chosen by some observer does not exceed δ_r, then it implies that the considered set of quantum fluctuations is indistinguishable from the environment since it is not distinguishable from the environment through the entire set of local observables.

Once an effective field theory is equipped with an effective configuration space qualified by (4.1), (1.16), and (1.18), then the spectral analysis for the canonical conjugate momentum operator follows a similar treatment as in the kinematic section of Chapter 1. This analysis defines the self-adjoint domain $D(\Pi)$ defined with respect to the neighborhood $U = U_0 \cap U_{\mathrm{d}}$ where U_0 is the effective configuration space with boundaries defined by (1.16) and (1.18), while U_{d} is the effective configuration space with boundaries defined by (4.1). It can be shown that the conjugated momentum operator admits infinitely many self-adjoint extensions that intersect nontrivially with the solution space of the Schrodinger equation. By the same functional calculus arguments, this possibility is extended to the Hamiltonian operator on the kinematical, but again not dynamically, because of the vanishing nontrivial intersection with the solution space of the functional Schrodinger equation.

Similar to our previous section, however, in this case, the requirement that the evolution must admit at least a contractive evolution semigroup will enforce a more restrictive condition on the allowed choice of initial states in order to eliminate a potential probability source. The probability source is not relevant to the existence of ghosts, but rather in relation to unresolvable degrees of freedom due to the finite sensitivity of the detector. Technically, there are given by probability current outside the configuration space U_{d}, which penetrates the boundary and flows into the effective configuration space. In other words, the existence of probability sources is related to assuming the same dynamics and interaction to hold for those degrees of freedom that are unresolvable, and we had no control in the first place. As a result, a more restrictive choice of initial states eliminates those that describe almost no resolvable degree of freedom.

Peak Theory for Discrete Random Field

The results described here are based on an ongoing collaborative work with Florian Kuhnel and Dominik Schwarz.

In the earlier section, we discussed the limitations of the conventional peaks theory when applied to discrete field theory. The problem lies in the breakdown of the primary assumption for peak detection based on the extremum constraint. For any

random field characterized by a power spectrum $P(k) \propto k^n$ for $n \geq -3$ at large k, finite difference methods poorly approximate spatial derivatives. So, a more robust and intuitive approach is to identify local maxima in a discrete field with an appropriate choice of neighborhood size that is at least bounded below by the correlation length of the random field. This naturally leads to the formal definition of block maxima in extreme value theory for replacing the definition of peaks based on the extremum constraint.

Our purpose is to develop a more rigorous approach for generalizing the conventional peak theory to consider realistic discrete random fields. We examine the accuracy of the spatial derivative approximated by the finite differences method across discrete random fields with various power spectra. We find that the approximation quality is inversely proportional to the deviation between the numerically measured and analytically predicted probability distribution of peak number density. In particular, in the high peak limit, the number density of peaks found by numerical search is suppressed by roughly an order of magnitude compared to the analytic expectations in [76]. Consequently, analytical frameworks assuming a specific continuous spatial profile below an effective resolution scale overestimate the number density of rare events detectable in discrete fields with finite resolution.

Nevertheless, the numerical search produces a similar scaling in the tail distribution as in [76]. This is expected since the asymptotic scaling behavior of the tail is determined by the distribution function of the underlying random field. Our future work will investigate the cumulative number density of peaks in [76] that converges to an extreme value statistics similar to the one obtained from numerical search by following a similar treatment in Chapter 2.

Backreaction in a Gravitational Collapse

The results described here are based on an ongoing collaborative work with Ludwig Eglseer and Stefan Hofmann.

When quantum field theory operates within dynamical spacetimes, quantum fluctuations of the matter field can be amplified to an extent that excites fluctuations of spacetime geometry. At leading order, we can estimate such an effect by measuring

the expectation value $\langle \delta g \rangle_\rho$ where ρ is the density matrix that evolves according to the Liouville equation $i\partial_t \rho = [H, \rho]$. The Hamiltonian, briefly speaking, is expanded to the third perturbative order, so it includes the coupling between the energy-momentum stress tensor of the matter field and the fluctuation of the spacetime geometry. Altogether, we solve explicitly for the time dependence of an initially a pure Gaussian state using the time-order evolution operator obtained from the Liouville equation. This approach allows numerical implementation to compute the full-time evolution of the density matrix to the point where third order assumption breaks down. In combination with numerical methods, we simulate the quantum backreaction in a contracting radiation-dominated universe, which mimics a similar physical condition within a collapsing star that could lead to the formation of a black hole. Our focus is on whether initial spatial inhomogeneities can be amplified through the accumulation of quantum backreaction and result in the development of large local deformation of spacetime geometry. If these initial inhomogeneities are not smoothed out over time, then their accumulation could accelerate the breakdown of the semiclassical framework, as new local geometry emerges in the neighborhood of the initial inhomogeneities.

Chapter A

Appendix

A.1 Technical Aspects of the Functional Representation of QFTCS

In this Appendix we will cover a minimal amount of the technical method of functional (Schrodinger) representation of quantum field theory in curved spacetimes, which should be sufficient for the computations in the Chapter 1. These are well established in the literature [20–23, 25, 26, 29, 30, 32–34, 39, 169, 170].

We will begin with the well known covariant approach using the action functional S for a free scalar field ϕ with mass m, which couples to the Ricci scalar through the parameter ζ:

$$S[\phi] = -\frac{1}{2}\int_{\mathcal{M}} \mathrm{d}^4x\, \sqrt{-g(x)}\, \left[g^{\mu\nu}\partial_\mu\phi(x)\,\partial_\nu\phi(x) + (m^2 + \zeta R)\,\phi^2(x)\right] \tag{A.1}$$

The functional Schrodinger representation of quantum field theory in curved spacetimes is a Hamiltonian formulation that foliates the spacetimes manifold $(\mathcal{M}, g) = \mathbb{R}\times\Sigma$ into three-dimensional hypersurfaces Σ_t of constant $x^0 \equiv t \in \mathbb{R}$, for t is the leaves of the foliation. Of course, such foliation can be made arbitrary, and the usual expression of the four metric can be decomposed into the $3+1$ form [171–174]:

$$\mathrm{d}s^2 = (-N^2 + N_iN^i)\,\mathrm{d}t^2 + 2N_i\mathrm{d}x^i\mathrm{d}t + h_{ij}\mathrm{d}x^i\mathrm{d}x^j \tag{A.2}$$

where N and N_i are the lapse function and shift vector, respectively; h_{ij} is the induced metric on Σ_t. They depends on $\boldsymbol{x}$ and t in general, but for brevity such notation is

hidden. Let us take the action as the starting point and foliating $\mathcal{M}$ by $\mathcal{M} \equiv \mathbb{R} \times \Sigma$, the action can be rewritten as

$$S = -\frac{1}{2}\int_{\mathbb{R}} \mathrm{d}t \int_{\Sigma_t} \mathrm{d}^3x\, N h^{1/2} \Bigg[\frac{\dot{\phi}^2(t,\boldsymbol{x})}{N^2} - \frac{2N^i}{N^2}\partial_i\phi(t,\boldsymbol{x})\dot{\phi}(t,\boldsymbol{x}) - \left(h^{ij} - \frac{N^iN^j}{N^2}\right)\partial_i\phi(t,\boldsymbol{x})\partial_j\phi(t,\boldsymbol{x})\Bigg] \quad \text{(A.3)}$$

where $\dot{\phi}(t,\boldsymbol{x}) \equiv \partial_t\phi(t,\boldsymbol{x})$ denotes the time derivative with respect to the field. The canonical conjugated momenta $\pi(t,\boldsymbol{x})$ are defined by:

$$\pi(t,\boldsymbol{x}) = \frac{\delta S}{\delta\dot{\phi}(t,\boldsymbol{x})} = \frac{h^{1/2}}{N}\left[\dot{\phi}(t,\boldsymbol{x}) - N^i\partial_i\phi(t,\boldsymbol{x})\right] . \quad \text{(A.4)}$$

Using the canonical momenta, we obtain the Hamiltonian from the action by performing the Legendre transformation

$$S[\phi] = \int_{\mathbb{R}} \mathrm{d}t \int_{\Sigma_t} \mathrm{d}^3x \ \left[\dot{\phi}(t,\boldsymbol{x})\pi(t,\boldsymbol{x}) - N\mathcal{H} - N^i\mathcal{H}_i\right] \quad \text{(A.5)}$$

where $\mathcal{H}$ and $\mathcal{H}_i$ are the Hamiltonian densities, which are projections of the energy-momentum stress tensor $T_{\mu\nu}$ by

$$\begin{aligned} \mathcal{H} &= h^{1/2} n^\mu n^\nu T_{\mu\nu} \\ \mathcal{H}_i &= h^{1/2} n^\mu E_i^\nu T_{\mu\nu} \\ T_{\mu\nu} &= \partial_\mu\phi(t,\boldsymbol{x})\partial_\nu\phi(t,\boldsymbol{x}) + g_{\mu\nu}\mathcal{L}, \end{aligned} \quad \text{(A.6)}$$

where $\mathcal{L}$ is the Lagrangian density, and again all spacetime dependence is hidden for brevity. The function $E : \Sigma \to \mathcal{M}$ is the embedding that defines the arbitrary foliation. n is the normal to the hypersurfaces Σ_t that is uniquely defined once the embedding E is specified: $n_\mu E_i^\mu = 0$ for $i = 1, 2, 3$ and $g^{\mu\nu}n^\mu n^\nu = -1$.

A.1. Technical Aspects of the Functional Representation of QFTCS

The dynamic of the quantum field in the functional representation of quantum field theory is governed by the time-dependent Schrodinger equation, which determines the time evolution of a quantum state $|\Psi_t\rangle$ along the foliation by:

$$i\frac{\partial}{\partial t}|\Psi_t\rangle = H|\Psi_t\rangle \tag{A.7}$$

where $H = \int_{\Sigma_t} \mathrm{d}^3x\,(N\mathcal{H} + N^i\mathcal{H}_i)$ is the Hamiltonian. The full field configuration space, which does not necessarily comply with the semiclassical approximation, contains a complete set of orthonormal bases $|\phi\rangle$. The quantum state that is expressed in terms of the orthonormal basis is the wave functional $\Psi_t[\phi] \equiv \langle\phi|\Psi_t\rangle$, and its time evolution is given by the functional Schrodinger equation: $i\partial_t\Psi_t[\phi] = H\Psi_t[\phi]$. Again, H is the same Hamiltonian as in (A.6), except that $\phi(t,\boldsymbol{x})$ and $\pi(t,\boldsymbol{x})$ are now promoted to canonical operators of fields and its momentum, $\Phi(\boldsymbol{x})$ and $\Pi(\boldsymbol{x})$, that satisfy the uncertainty principle: $[\Phi(\boldsymbol{x}),\Pi(\boldsymbol{y})] = i\delta^3(\boldsymbol{x}-\boldsymbol{y})$. Given that the field operator is a multiplicative operator that returns the field value itself: $\Phi(\boldsymbol{x})\Psi_t[\phi] = \phi(x)\Psi_t[\phi]$, the momentum operators $\Pi(\boldsymbol{x})$ that satisfy the uncertainty principle are the functional derivatives with respect to the field $\Pi(\boldsymbol{x}) = -i\delta/\delta\phi(\boldsymbol{x})$.

Let us solve for the dynamical equation of the functional Schrodinger equation following a similar treatment in [20, 21, 23]. Consider a free field theory and its ground state wave functional

$$\Psi_t[\phi] = \mathcal{N}_t \exp\left(-\frac{1}{2}\int_{\Sigma_t} \mathrm{d}\mu(\boldsymbol{x},\boldsymbol{y})\,\phi(\boldsymbol{x})\mathcal{K}_t(\boldsymbol{x},\boldsymbol{y})\phi(\boldsymbol{y})\right) \tag{A.8}$$

where $\mathcal{N}_t \in \mathbb{C}$ is the normalization factor, $\mathcal{K}_t(\boldsymbol{x},\boldsymbol{y})$ is the bikernel function. To evaluate the functional Schrodinger equation corresponding to the Gaussian ground state wave function, consider the time derivative ground state wave functional:

$$\frac{\partial}{\partial t}\Psi_t[\phi] = \left(\frac{\partial}{\partial t}\ln\mathcal{N}_t - \frac{1}{2}\frac{\partial}{\partial t}\int_{\Sigma_t} \mathrm{d}\mu(\boldsymbol{x},\boldsymbol{y})\,\phi(\boldsymbol{x})\,\mathcal{K}_t(\boldsymbol{x},\boldsymbol{y})\,\phi(\boldsymbol{y})\right)\Psi_t[\phi] \tag{A.9}$$

where $\mathrm{d}\mu(\boldsymbol{x},\boldsymbol{y}) \equiv \mathrm{d}^3x\,\mathrm{d}^3y\sqrt{h(x)h(y)}$ is the covariant measure of the hypersurface Σ_t. On the other hand, consider the Hamiltonian operator

$$H_t\Psi_t[\phi] = \int_{\Sigma_t} \mathrm{d}\mu(\boldsymbol{x}) N \left[-\frac{1}{h(x)}\frac{\delta^2}{\delta\phi(\boldsymbol{x})^2} + \phi(\boldsymbol{x})P_x\phi(\boldsymbol{x}) \right]\Psi_t[\phi] \tag{A.10}$$

where $P_x \equiv (-\Delta_x + m^2 + \zeta R)$ and Δ_x the spatial Laplace operator defined by $\Delta_x = (Nh^{1/2})^{-1}\partial_i(Nh^{1/2}g^{ij}\partial_j)$. Insert the time derivative and apply the Hamiltonian operator onto the wave functional, by power counting, we obtain two dynamic equations that determine the time evolution of the bi-local kernel function $\mathcal{K}_t(\boldsymbol{x},\boldsymbol{y})$:

$$i\partial_t\tilde{\mathcal{K}}_t(\boldsymbol{x},\boldsymbol{y}) = \int_{\Sigma_t} \mathrm{d}\mu(\boldsymbol{z})\,\frac{N}{h(\boldsymbol{z})}\,\left[\tilde{\mathcal{K}}_t(\boldsymbol{x},\boldsymbol{z})\tilde{\mathcal{K}}_t(\boldsymbol{z},\boldsymbol{y})\right] - Nh^{1/2}(\boldsymbol{x})P_x\delta^3(\boldsymbol{x},\boldsymbol{y})$$

where $\tilde{\mathcal{K}}_t(\boldsymbol{x},\boldsymbol{y}) = h^{1/2}(\boldsymbol{x})h^{1/2}(\boldsymbol{y})\mathcal{K}_t(\boldsymbol{x},\boldsymbol{y})$ and $\delta^3(\boldsymbol{x},\boldsymbol{y}) \equiv h^{-1/2}(\boldsymbol{x})\delta^3(\boldsymbol{x}-\boldsymbol{y})h^{-1/2}(\boldsymbol{y})$. The time evolution of the normalization factor $\mathcal{N}_t$ can be uniquely determined by the coincident limit of the bikernel function

$$\partial_t \ln \mathcal{N}_t = -\frac{i}{2}\int_{\Sigma_t} \mathrm{d}\mu(\boldsymbol{x})\, N_t\mathcal{K}_t(\boldsymbol{x},\boldsymbol{x}) \tag{A.11}$$

This can be readily resolved to show that the normalization factor $\mathcal{N}_t$ is in fact a function of the bi-local kernel function

$$\mathcal{N}_t = \mathcal{N}_0 \exp\left(-\frac{i}{2}\int_I \mathrm{d}t \int_{\Sigma_t} \mathrm{d}\mu(x)\, N_t\ \mathcal{K}_t(\boldsymbol{x},\boldsymbol{x})\right) \tag{A.12}$$

where $t \in I \in \mathbb{R}$ and $\mathcal{N}_0$ is the integration constant determined by the initial data of the wave functional Ψ_{t_0} at the initial time t_0. So once the bi-local kernel function is solved, the time dependence of the wave functional is uniquely determined.

At last, we follow the same procedure in [20, 23] to show that the solution to the functional Schrodinger equation is related to the solution of the Klein-Gordon equation in the Heisenberg picture by the following relation:

$$\frac{1}{N}\frac{\partial}{\partial t}\psi(t,\boldsymbol{x}) = i\int_{\Sigma_t} \mathrm{d}\mu(\boldsymbol{y})\ \mathcal{K}_t(\boldsymbol{x},\boldsymbol{y})\psi(t,\boldsymbol{y}) \tag{A.13}$$

This can be seen straightforwardly by multiplying the kernel equation on both sides and integrate over $\boldsymbol{y}$. By doing so we can rewrite the kernel equation as

$$\begin{aligned} & i\int_{\Sigma_t} \mathrm{d}^3y \left[\partial_t(\tilde{\mathcal{K}}(\boldsymbol{x},\boldsymbol{y}))\psi(t,\boldsymbol{y})\right] \\ & \qquad = -i\int_{\Sigma_t} \mathrm{d}^3y \ \left[\tilde{\mathcal{K}}(\boldsymbol{x},\boldsymbol{y})\partial_t\psi(t,\boldsymbol{y})\right] - Nh^{1/2}(\boldsymbol{x})P_x\psi(t,\boldsymbol{x}) \end{aligned} \tag{A.14}$$

This can be recast into the following form using integration by parts:

$$i\frac{\partial}{\partial t}\left(\int_{\Sigma_t} \mathrm{d}^3y\ \tilde{\mathcal{K}}_t(\boldsymbol{x},\boldsymbol{y})\,\psi(t,\boldsymbol{y})\right) + Nh^{1/2}(\boldsymbol{x})P_x\psi(t,\boldsymbol{x}) = 0 \tag{A.15}$$

Apply the relation (A.13) once again, and we obtain the Klein-Gordon equation

$$\frac{\partial}{\partial t}\left(\sqrt{-g}g^{00}\frac{\partial}{\partial t}\psi(t,\boldsymbol{x})\right) + Nh^{1/2}(\boldsymbol{x})P_x\psi(t,\boldsymbol{x}) = (\Box_x - m^2)\psi(t,\boldsymbol{x}) = 0 \tag{A.16}$$

where $\Box_x = g^{-1/2}\partial_\mu(g^{1/2}g^{\mu\nu}\partial_\nu)$ is the Klein-Gordon operator. As we will next and in Chapter 1, the relation (A.13) allows us to express the variance of quantum fluctuation in the momentum space in terms of the power spectrum. This is consistent with what we expect when calculating the two-point correlation function in the momentum space for free fields in both the Heisenberg and the Schrodinger picture.

A.2 Example using the Friedmann universe

Now, to get an intuitive understanding of the bi-local kernel functional, we consider an explicit example, such as the homogeneous and isotropic Friedmann universe. Spatial symmetries allow us to rewrite (A.13) in the momentum space representation and compare mode-by-mode:

$$\frac{1}{N}\frac{\partial}{\partial t}\psi(t,\boldsymbol{k}) = ih^{1/2}\mathcal{K}_t(\boldsymbol{k})\psi(t,\boldsymbol{k}) \tag{A.17}$$

This means that the real part of the kernel function is

$$\mathrm{Re}\,\mathcal{K}_t(\boldsymbol{k}) = -\frac{i}{Nh^{1/2}}\frac{W(\psi,\psi^*)}{|\psi(t,\boldsymbol{k})|^2} \tag{A.18}$$

where $W(\psi,\psi) = \psi^*(t,\boldsymbol{k})\partial_t\psi(t,\boldsymbol{k}) - \psi(t,\boldsymbol{k})\partial_t\psi^*(t,\boldsymbol{k})$ is the Wronskian. Since the scalar field $\psi(t,\boldsymbol{k})$ is the solution to the Klein-Gordon equation, the Wronskian is $W(\psi,\psi^*) = iNh^{-1/2}$ [40], such that

$$\mathrm{Re}\,\mathcal{K}_t(\boldsymbol{k}) = \frac{1}{h(t)}\frac{1}{|\psi(t,\boldsymbol{k})|^2} \tag{A.19}$$

Notice that the probability density distribution of the ground state Gaussian wave functional is given by its modulus square

$$P_t[\phi] = |\Psi_t[\phi]|^2 = |\mathcal{N}_t|^2 \exp\left[-\int_{\mathbb{K}}\frac{\mathrm{d}^3k}{(2\pi)^3}|\phi(\boldsymbol{k})|^2 h_t\ \mathrm{Re}\,\mathcal{K}_t(\boldsymbol{k})\right] \tag{A.20}$$

This means that $\mathrm{Re}\,\mathcal{K}_t(\boldsymbol{k})$ represents the statistical variance of the quantum fluctuations. So the exponential for each $\boldsymbol{k}$ can actually rewritten as

$$-\int_{\mathbb{K}}\frac{\mathrm{d}^3k}{(2\pi)^3}\frac{|\phi(\boldsymbol{k})|^2}{|\psi(t,\boldsymbol{k})|^2} \tag{A.21}$$

As a result, for each mode, the variance of the probability density distribution is given by $|\psi(t,\boldsymbol{k})|^2$, which agrees with the Heisenberg approach

$$\langle\, 0 \,|\, \psi(t,\boldsymbol{x})\psi(t,\boldsymbol{x}) \,|\, 0 \,\rangle = \int_{\mathbb{K}} \frac{\mathrm{d}^3k}{(2\pi)^3}\, |\psi(t,\boldsymbol{k})|^2 \tag{A.22}$$

A.2.1 Normalization of the wave functional

Finally, using the Friedmann universe as an example, we will show that the norm wave functional, when considering a field configuration space without compact support, is always conserved, such that $\|\Psi_t\|^2 = 1$ for all time $t \in \mathbb{R}$ [1].

Consider the total probability is given by integrating over the entire field configuration space is given by

$$\|\Psi_t\|^2 = \int_{\mathcal{C}} \mathscr{D}\phi\ |P_t[\phi]|^2 \tag{A.23}$$

Given that $\mathcal{K}_t(\boldsymbol{k})$ satisfies the functional Schrodinger equation and solves the Klein-Gordon equation simultaneously, one can recast the probability density distribution as follows

$$\|\Psi_t\|^2 = \left[\prod_{\boldsymbol{k}} \int_{-\infty}^{\infty} \mathrm{d}\phi(\boldsymbol{k})\right]\ |\mathcal{N}_t|^2 \exp\left(-\int_{\mathbb{K}} \frac{\mathrm{d}^3k}{(2\pi)^3}\ \frac{\phi(\boldsymbol{k})\phi(-\boldsymbol{k})}{|\psi(\boldsymbol{k},t)|^2}\right) \tag{A.24}$$

Since the Fourier modes of different $\boldsymbol{k}$ in the Friedmann universe are decoupled, the probability density distribution for each $\boldsymbol{k}$ can be integrated individually as the usual Gaussian integral:

$$\|\Psi_t\|^2 = |\mathcal{N}_t|^2 \prod_{\boldsymbol{k}} \left[\int_{-\infty}^{\infty} \mathrm{d}\phi(\boldsymbol{k}) \exp\left(-\frac{1}{V}\frac{\phi(\boldsymbol{k})\phi(-\boldsymbol{k})}{|\psi(\boldsymbol{k},t)|^2}\right)\right] \tag{A.25}$$

[1] It can be shown that the norm of the wave functional is also conserved for general spacetimes with a field configuration space without compact support. This can be proven relatively easily using generating functional [21] and show that $\partial_t\|\Psi_t\|^2 = 0$ for all $t \in \mathbb{R}$; or with some extra effort to show that $\|\Psi_t\|^2 = 1$ once the initial Gaussian wave functional is normalized to unity.

where we have converted the continuous integral into a discrete sum via

$$\int_{-\infty}^{\infty} \frac{\mathrm{d}^3 k}{(2\pi)^3} \to \frac{1}{V} \sum_{\boldsymbol{k}} , \tag{A.26}$$

$V \equiv \int_{-\infty}^{\infty} \mathrm{d}^3 x$ is the total comoving volume Integrating over the Gaussian distribution of individual $\boldsymbol{k}$, we obtain the product

$$\|\Psi_t\|^2 = |\mathcal{N}_t|^2 \prod_{\boldsymbol{k}} \left(\pi |\psi(\boldsymbol{k}, t)|^2\right)^{1/2} \tag{A.27}$$

Now, given that the normalization factor in the momentum space has the form

$$|\mathcal{N}_t|^2 = |\mathcal{N}_0|^2 \, \exp\left[-i \int_{-\infty}^{\infty} \mathrm{d}t \, N_t \, h_t^{1/2} \, V \int_{\mathbb{K}} \frac{\mathrm{d}^3 k}{(2\pi)^3} \, \mathrm{Im}\, \mathcal{K}_t(\boldsymbol{k}) \right] , \tag{A.28}$$

and the imaginary part of the bi-local kernel function can be expressed in terms of the mode function using (A.13)

$$\mathrm{Im}\, \mathcal{K}_t(\boldsymbol{k}) = -\frac{i}{2N_t} \frac{\partial}{\partial t} \ln |\psi(t, \boldsymbol{k})|^2 \, . \tag{A.29}$$

Inserting this expression, we obtain

$$|\mathcal{N}_t|^2 = |\mathcal{N}_0|^2 \exp\left(-\frac{1}{2} \sum_{\boldsymbol{k}} \int_I \mathrm{d}t \, \partial_t \ln |\psi(t, \boldsymbol{k})|^2 \right) = |\mathcal{N}_0|^2 \prod_{\boldsymbol{k}} \left| \frac{\psi(t_0, \boldsymbol{k})}{\psi(t, \boldsymbol{k})} \right| \tag{A.30}$$

where we have again converted the continuous k-integral into a discrete sum of infinitesimally separated elements. This expression tells us that the exponential function of the normalization factor is just the product of the mode function $\psi(t, \boldsymbol{k})$ for all $\boldsymbol{k} \in \mathbb{K}$. Altogether, the norm of the state is

$$\|\Psi_t\|^2 = |\mathcal{N}_0|^2 \prod_{\boldsymbol{k}} \left(\pi |\psi(t_0, \boldsymbol{k})|^2\right)^{1/2} = \|\Psi_{t_0}\|^2 \tag{A.31}$$

which is the norm at the initial time. Given that the initial state is normalizable, $\|\Psi_{t_0}\| = 1$, the quantum state remains normalized for all time $t \in \mathbb{R}$. So we have

shown that the norm is indeed conserved for field configuration space without compact support.

Appendix A. Appendix

Bibliography

[1] Steven Weinberg. "Phenomenological Lagrangians". In: *Physica A: Statistical Mechanics and its Applications* 96.1 (Apr. 1979), pp. 327–340. ISSN: 0378-4371. DOI: 10.1016/0378-4371(79)90223-1.

[2] John F. Donoghue. "General relativity as an effective field theory: The leading quantum corrections". In: *Physical Review D* 50.6 (Sept. 1994). Publisher: American Physical Society, pp. 3874–3888. DOI: 10.1103/PhysRevD.50.3874.

[3] John F. Donoghue. *Introduction to the Effective Field Theory Description of Gravity*. arXiv:gr-qc/9512024. Dec. 1995. DOI: 10.48550/arXiv.gr-qc/9512024.

[4] Cliff P. Burgess. "Quantum Gravity in Everyday Life: General Relativity as an Effective Field Theory". en. In: *Living Reviews in Relativity* 7.1 (Dec. 2004). Company: Springer Distributor: Springer Institution: Springer Label: Springer Publisher: Springer International Publishing, pp. 1–56. ISSN: 1433-8351. DOI: 10.12942/lrr-2004-5.

[5] C. P. Burgess. "Introduction to Effective Field Theory". In: *Annual Review of Nuclear and Particle Science* 57.1 (Nov. 2007). arXiv:hep-th/0701053, pp. 329–362. ISSN: 0163-8998, 1545-4134. DOI: 10.1146/annurev.nucl.56.080805.140508.

[6] Steven Weinberg. "Effective field theory for inflation". In: *Physical Review D* 77.12 (June 2008). Publisher: American Physical Society, p. 123541. DOI: 10.1103/PhysRevD.77.123541.

[7] C. P. Burgess, Hyun Min Lee, and Michael Trott. "Power-counting and the validity of the classical approximation during inflation". en. In: *Journal of High Energy Physics* 2009.09 (Sept. 2009), p. 103. ISSN: 1126-6708. DOI: 10.1088/1126-6708/2009/09/103.

[8] John F. Donoghue. "The effective field theory treatment of quantum gravity". In: *AIP Conference Proceedings* 1483.1 (Oct. 2012), pp. 73–94. ISSN: 0094-243X. DOI: 10.1063/1.4756964.

[9] Peter Adshead et al. "Power-counting during single-field slow-roll inflation". en. In: *Journal of Cosmology and Astroparticle Physics* 2018.02 (Feb. 2018), p. 016. ISSN: 1475-7516. DOI: 10.1088/1475-7516/2018/02/016.

[10] John F. Donoghue. *Quantum General Relativity and Effective Field Theory*. arXiv:2211.09902 [hep-th]. Jan. 2023. DOI: 10.48550/arXiv.2211.09902.

[11] R. E. Behrends, R. J. Finkelstein, and A. Sirlin. "Radiative Corrections to Decay Processes". In: *Physical Review* 101.2 (Jan. 1956). Publisher: American Physical Society, pp. 866–873. DOI: 10.1103/PhysRev.101.866.

[12] Toichiro Kinoshita and Alberto Sirlin. "Radiative Corrections to Fermi Interactions". In: *Physical Review* 113.6 (Mar. 1959). Publisher: American Physical Society, pp. 1652–1660. DOI: 10.1103/PhysRev.113.1652.

[13] Alberto Sirlin and Andrea Ferroglia. "Radiative corrections in precision electroweak physics: A historical perspective". In: *Reviews of Modern Physics* 85.1 (Feb. 2013). Publisher: American Physical Society, pp. 263–297. DOI: 10.1103/RevModPhys.85.263.

[14] Alexander Vilenkin. "The Interpretation of the Wave Function of the Universe". In: *Phys. Rev. D* 39 (1989), p. 1116. DOI: 10.1103/PhysRevD.39.1116.

[15] Chung-I Kuo and L. H. Ford. "Semiclassical gravity theory and quantum fluctuations". In: *Phys. Rev. D* 47 (1993), pp. 4510–4519. DOI: 10.1103/PhysRevD.47.4510.

[16] Hiroki Matsui and Naoki Watamura. "Quantum spacetime instability and breakdown of semiclassical gravity". In: *Physical Review D* 101.2 (2020), p. 025014.

[17] Serge Massar and Renaud Parentani. "Unitary and nonunitary evolution in quantum cosmology". In: *Physical Review D* 59.12 (1999), p. 123519.

[18] Paul R Anderson, Carmen Molina-Paris, and Emil Mottola. "Linear response, validity of semiclassical gravity, and the stability of flat space". In: *Physical Review D* 67.2 (2003), p. 024026.

[19] Michael Reed and Barry Simon. *Methods of modern mathematical physics, Vol. II*. Academic Press, New York, 1975.

[20] Oscar J. P. Eboli, So-Young Pi, and M. Samiullah. "Renormalizability of Functional Schrodinger Picture in Robertson-walker Space-time". In: *Annals Phys.* 193 (1989), p. 102. DOI: 10.1016/0003-4916(89)90354-0.

[21] Brian Hatfield. *Quantum field theory of point particles and strings*. CRC Press, 2018.

[22] Jonathan J. Halliwell. "Global space-time symmetries in the functional Schrodinger picture". In: *Phys. Rev. D* 43 (1991), pp. 2590–2609. DOI: 10.1103/PhysRevD.43.2590.

[23] D. V. Long and G. M. Shore. "The Schrodinger wave functional and vacuum states in curved space-time". In: *Nucl. Phys. B* 530 (1998), pp. 247–278. DOI: 10.1016/S0550-3213(98)00408-8.

[24] Jennie H. Traschen and Robert H. Brandenberger. "Particle Production During Out-of-equilibrium Phase Transitions". In: *Phys. Rev. D* 42 (1990), pp. 2491–2504. DOI: 10.1103/PhysRevD.42.2491.

[25] Alan H Guth and So-Young Pi. "Quantum mechanics of the scalar field in the new inflationary universe". In: *Physical Review D* 32.8 (1985), p. 1899.

[26] D. Boyanovsky, H. J. de Vega, and R. Holman. "Nonequilibrium evolution of scalar fields in FRW cosmologies". In: *Phys. Rev. D* 49 (6 Mar. 1994), pp. 2769–2785. DOI: 10.1103/PhysRevD.49.2769.

[27] R. Floreanini, C. T. Hill, and R. Jackiw. "Functional Representation for the Isometries of de Sitter Space". In: *Annals Phys.* 175 (1987), p. 345. DOI: 10.1016/0003-4916(87)90213-2.

[28] Jemal Guven, Ben Lieberman, and Christopher T. Hill. "Schrodinger Picture Field Theory in Robertson-walker Flat Space-times". In: *Phys. Rev. D* 39 (1989), p. 438. DOI: 10.1103/PhysRevD.39.438.

[29] Stefan Hofmann and Marc Schneider. "Classical versus quantum completeness". In: *Phys. Rev. D* 91.12 (2015), p. 125028. DOI: 10.1103/PhysRevD.91.125028.

[30] Stefan Hofmann and Marc Schneider. "Non-Gaussian ground-state deformations near a black-hole singularity". In: *Phys. Rev. D* 95.6 (2017), p. 065033. DOI: 10.1103/PhysRevD.95.065033.

[31] Ludwig Eglseer, Stefan Hofmann, and Marc Schneider. "Quantum populations near black-hole singularities". In: *Phys. Rev. D* 104.10 (2021), p. 105010. DOI: 10.1103/PhysRevD.104.105010.

[32] Stefan Hofmann, Marc Schneider, and Maximilian Urban. "Quantum complete prelude to inflation". In: *Phys. Rev. D* 99.6 (2019), p. 065012. DOI: 10.1103/PhysRevD.99.065012.

[33] Curtis G. Callan Jr. and Frank Wilczek. "On geometric entropy". In: *Phys. Lett. B* 333 (1994), pp. 55–61. DOI: 10.1016/0370-2693(94)91007-3.

[34] Jürgen Berges, Stefan Floerchinger, and Raju Venugopalan. "Dynamics of entanglement in expanding quantum fields". In: *JHEP* 04 (2018), p. 145. DOI: 10.1007/JHEP04(2018)145.

[35] Charles G Torre and Madhavan Varadarajan. "Quantum fields at any time". In: *Physical Review D* 58.6 (1998), p. 064007.

[36] Tosio Kato. *Perturbation theory for linear operators*. Vol. 132. Springer Science & Business Media, 2013.

[37] M. Reed and B. Simon. *Methods of Modern Mathematical Physics. 2. Fourier Analysis, Self-adjointness*. 1975.

[38] Kôsaku Yosida. *Functional analysis*. Vol. 123. Springer Science & Business Media, 2012.

[39] Einar Hille and Ralph Saul Phillips. *Functional analysis and semi-groups*. Vol. 31. American Mathematical Soc., 1996.

[40] Leonard E. Parker and D. Toms. *Quantum Field Theory in Curved Spacetime: Quantized Field and Gravity*. Cambridge Monographs on Mathematical Physics. Cambridge University Press, Aug. 2009. ISBN: 978-0-521-87787-9, 978-0-521-87787-9, 978-0-511-60155-2. DOI: 10.1017/CBO9780511813924.

[41] Viatcheslav F. Mukhanov, H. A. Feldman, and Robert H. Brandenberger. "Theory of cosmological perturbations. Part 1. Classical perturbations. Part 2. Quantum theory of perturbations. Part 3. Extensions". In: *Phys. Rept.* 215 (1992), pp. 203–333. DOI: 10.1016/0370-1573(92)90044-Z.

[42] N. D. Birrell and P. C. W. Davies. *Quantum Fields in Curved Space*. Cambridge Monographs on Mathematical Physics. Cambridge, UK: Cambridge Univ. Press, Feb. 1984. ISBN: 978-0-521-27858-4, 978-0-521-27858-4. DOI: 10.1017/CBO9780511622632.

[43] Nicholas David Birrell and Paul Charles William Davies. "Quantum fields in curved space". In: (1984).

[44] Viatcheslav Mukhanov and Sergei Winitzki. *Introduction to quantum effects in gravity*. Cambridge University Press, June 2007. ISBN: 978-0-521-86834-1, 978-1-139-78594-5.

[45] William H. Press and Paul Schechter. "Formation of Galaxies and Clusters of Galaxies by Self-Similar Gravitational Condensation". In: *The Astrophysical Journal* 187 (Feb. 1974). ADS Bibcode: 1974ApJ...187..425P, pp. 425–438. ISSN: 0004-637X. DOI: 10.1086/152650.

[46] David Matravers. "Steven Weinberg: Cosmology". en. In: *General Relativity and Gravitation* 41.6 (June 2009). Company: Springer Distributor: Springer Institution: Springer Label: Springer Publisher: Springer US, pp. 1455–1458. ISSN: 1572-9532. DOI: 10.1007/s10714-008-0728-z.

[47] Houjun Mo, Frank van den Bosch, and Simon White. *Galaxy Formation and Evolution*. Cambridge: Cambridge University Press, 2010. ISBN: 978-0-521-85793-2. DOI: 10.1017/CBO9780511807244.

[48] Rohan P. Naidu et al. "Two Remarkably Luminous Galaxy Candidates at z ≈ 10–12 Revealed by JWST". en. In: *The Astrophysical Journal Letters* 940.1 (Nov. 2022). Publisher: The American Astronomical Society, p. L14. ISSN: 2041-8205. DOI: 10.3847/2041-8213/ac9b22.

[49] Ivo Labbé et al. "A population of red candidate massive galaxies ~600 Myr after the Big Bang". en. In: *Nature* 616.7956 (Apr. 2023). Publisher: Nature Publishing Group, pp. 266–269. ISSN: 1476-4687. DOI: 10.1038/s41586-023-05786-2.

[50] Hakim Atek et al. "Revealing galaxy candidates out to z ~ 16 with JWST observations of the lensing cluster SMACS0723". In: *Monthly Notices of the Royal Astronomical Society* 519.1 (Feb. 2023), pp. 1201–1220. ISSN: 0035-8711. DOI: 10.1093/mnras/stac3144.

[51] N J Adams et al. "Discovery and properties of ultra-high redshift galaxies (9 < z < 12) in the JWST ERO SMACS 0723 Field". In: *Monthly Notices of the Royal Astronomical Society* 518.3 (Jan. 2023), pp. 4755–4766. ISSN: 0035-8711. DOI: 10.1093/mnras/stac3347.

[52] L Barrufet et al. "Unveiling the nature of infrared bright, optically dark galaxies with early JWST data". In: *Monthly Notices of the Royal Astronomical Society* 522.1 (June 2023), pp. 449–456. ISSN: 0035-8711. DOI: 10.1093/mnras/stad947.

[53] Mengyuan Xiao et al. "Accelerated formation of ultra-massive galaxies in the first billion years". en. In: *Nature* 635.8038 (Nov. 2024). Publisher: Nature Publishing Group, pp. 311–315. ISSN: 1476-4687. DOI: 10.1038/s41586-024-08094-5.

[54] R Gottumukkala et al. "Unveiling the hidden Universe with JWST: the contribution of dust-obscured galaxies to the stellar mass function at z ~ 3 – 8". In: *Monthly Notices of the Royal Astronomical Society* 530.1 (May 2024), pp. 966–983. ISSN: 0035-8711. DOI: 10.1093/mnras/stae754.

[55] Andrea Weibel et al. “Galaxy build-up in the first 1.5 Gyr of cosmic history: insights from the stellar mass function at z ~ 4–9 from JWST NIRCam observations”. In: *Monthly Notices of the Royal Astronomical Society* 533.2 (Sept. 2024), pp. 1808–1838. ISSN: 0035-8711. DOI: 10.1093/mnras/stae1891.

[56] Katherine Chworowsky et al. “Evidence for a Shallow Evolution in the Volume Densities of Massive Galaxies at z = 4–8 from CEERS”. en. In: *The Astronomical Journal* 168.3 (Aug. 2024). Publisher: The American Astronomical Society, p. 113. ISSN: 1538-3881. DOI: 10.3847/1538-3881/ad57c1.

[57] Adam C. Carnall et al. “A massive quiescent galaxy at redshift 4.658”. en. In: *Nature* 619.7971 (July 2023). Publisher: Nature Publishing Group, pp. 716–719. ISSN: 1476-4687. DOI: 10.1038/s41586-023-06158-6.

[58] Caitlin M. Casey et al. “COSMOS-Web: Intrinsically Luminous z □ 10 Galaxy Candidates Test Early Stellar Mass Assembly”. en. In: *The Astrophysical Journal* 965.1 (Apr. 2024). Publisher: The American Astronomical Society, p. 98. ISSN: 0004-637X. DOI: 10.3847/1538-4357/ad2075.

[59] Stefano Carniani et al. “Spectroscopic confirmation of two luminous galaxies at a redshift of 14”. en. In: *Nature* 633.8029 (Sept. 2024). Publisher: Nature Publishing Group, pp. 318–322. ISSN: 1476-4687. DOI: 10.1038/s41586-024-07860-9.

[60] L. Napolitano et al. “Seven wonders of Cosmic Dawn: JWST confirms a high abundance of galaxies and AGN at z □ 9–11 in the GLASS field”. en. In: *Astronomy & Astrophysics* 693 (Jan. 2025). Publisher: EDP Sciences, A50. ISSN: 0004-6361, 1432-0746. DOI: 10.1051/0004-6361/202452090.

[61] Michael Boylan-Kolchin. “Stress testing ΛCDM with high-redshift galaxy candidates”. en. In: *Nature Astronomy* 7.6 (June 2023). Publisher: Nature Publishing Group, pp. 731–735. ISSN: 2397-3366. DOI: 10.1038/s41550-023-01937-7.

[62] Thomas Harvey et al. “EPOCHS. IV. SED Modeling Assumptions and Their Impact on the Stellar Mass Function at 6.5 ≤ z ≤ 13.5 Using PEARLS and Public JWST Observations”. en. In: *The Astrophysical Journal* 978.1 (Dec. 2024). Publisher: The American Astronomical Society, p. 89. ISSN: 0004-637X. DOI: 10.3847/1538-4357/ad8c29.

[63] Qianran Xia, Dragan Huterer, and Nhat-Minh Nguyen. "Late-time growth weakly affects the significance of high-redshift massive galaxies". In: *The Open Journal of Astrophysics* 8 (May 2025). arXiv:2503.00155 [astro-ph]. ISSN: 2565-6120. DOI: 10.33232/001c.137793.

[64] Joshua J. Ziegler et al. *Explaining the "too massive" high-redshift galaxies in JWST data: numerical study of three effects and a simple relation*. arXiv:2507.21409 [astro-ph]. July 2025. DOI: 10.48550/arXiv.2507.21409.

[65] Eduardo Bañados et al. "An 800-million-solar-mass black hole in a significantly neutral Universe at a redshift of 7.5". en. In: *Nature* 553.7689 (Jan. 2018). Publisher: Nature Publishing Group, pp. 473–476. ISSN: 1476-4687. DOI: 10.1038/nature25180.

[66] Lukas J. Furtak et al. "A high black-hole-to-host mass ratio in a lensed AGN in the early Universe". en. In: *Nature* 628.8006 (Apr. 2024). Publisher: Nature Publishing Group, pp. 57–61. ISSN: 1476-4687. DOI: 10.1038/s41586-024-07184-8.

[67] Jenny E. Greene et al. "UNCOVER Spectroscopy Confirms the Surprising Ubiquity of Active Galactic Nuclei in Red Sources at z > 5". en. In: *The Astrophysical Journal* 964.1 (Mar. 2024). Publisher: The American Astronomical Society, p. 39. ISSN: 0004-637X. DOI: 10.3847/1538-4357/ad1e5f.

[68] Roberto Maiolino et al. "A small and vigorous black hole in the early Universe". en. In: *Nature* 627.8002 (Mar. 2024). Publisher: Nature Publishing Group, pp. 59–63. ISSN: 1476-4687. DOI: 10.1038/s41586-024-07052-5.

[69] Roberto Maiolino et al. *A black hole in a near-pristine galaxy 700 million years after the Big Bang*. arXiv:2505.22567 [astro-ph]. Sept. 2025. DOI: 10.48550/arXiv.2505.22567.

[70] Junehyoung Jeon et al. *The Emerging Black Hole Mass Function in the High-Redshift Universe*. arXiv:2503.14703 [astro-ph]. June 2025. DOI: 10.48550/arXiv.2503.14703.

[71] Ignas Juodžbalis et al. *A direct black hole mass measurement in a Little Red Dot at the Epoch of Reionization*. arXiv:2508.21748 [astro-ph]. Sept. 2025. DOI: 10.48550/arXiv.2508.21748.

[72] V. Mukhanov. *Physical Foundations of Cosmology*. Oxford: Cambridge University Press, 2005. ISBN: 978-0-521-56398-7. DOI: 10.1017/CBO9780511790553.

[73] Sidney I. Resnick. *Extreme Values, Regular Variation and Point Processes*. Ed. by Thomas V. Mikosch, Sidney I. Resnick, and Stephen M. Robinson. Springer Series in Operations Research and Financial Engineering. New York, NY: Springer, 1987. ISBN: 978-0-387-75952-4 978-0-387-75953-1. DOI: 10.1007/978-0-387-75953-1.

[74] Stuart Coles. *An Introduction to Statistical Modeling of Extreme Values*. Springer Series in Statistics. London: Springer, 2001. ISBN: 978-1-84996-874-4 978-1-4471-3675-0. DOI: 10.1007/978-1-4471-3675-0.

[75] Edmund Bertschinger. "Multiscale Gaussian Random Fields and Their Application to Cosmological Simulations". en. In: *The Astrophysical Journal Supplement Series* 137.1 (Nov. 2001). Publisher: IOP Publishing, p. 1. ISSN: 0067-0049. DOI: 10.1086/322526.

[76] J. M. Bardeen et al. "The Statistics of Peaks of Gaussian Random Fields". In: *The Astrophysical Journal* 304 (May 1986). ADS Bibcode: 1986ApJ...304...15B, p. 15. ISSN: 0004-637X. DOI: 10.1086/164143.

[77] R. Brandenberger, H. Feldman, and V. Mukhanov. *Classical and Quantum Theory of Perturbations in Inflationary Universe Models*. arXiv:astro-ph/9307016. July 1993. DOI: 10.48550/arXiv.astro-ph/9307016.

[78] Eiichiro Komatsu. "Hunting for primordial non-Gaussianity in the cosmic microwave background". en. In: *Classical and Quantum Gravity* 27.12 (May 2010), p. 124010. ISSN: 0264-9381. DOI: 10.1088/0264-9381/27/12/124010.

[79] P. a. R. Ade et al. "Planck 2013 results. XXIV. Constraints on primordial non-Gaussianity". en. In: *Astronomy & Astrophysics* 571 (Nov. 2014). Publisher: EDP Sciences, A24. ISSN: 0004-6361, 1432-0746. DOI: 10.1051/0004-6361/201321554.

[80] P. a. R. Ade et al. "Planck 2015 results - XVII. Constraints on primordial non-Gaussianity". en. In: *Astronomy & Astrophysics* 594 (Oct. 2016). Publisher: EDP Sciences, A17. ISSN: 0004-6361, 1432-0746. DOI: 10.1051/0004-6361/201525836.

[81] Chris Pattison et al. "Quantum diffusion during inflation and primordial black holes". en. In: *Journal of Cosmology and Astroparticle Physics* 2017.10 (Oct. 2017), p. 046. ISSN: 1475-7516. DOI: 10.1088/1475-7516/2017/10/046.

[82] Jose María Ezquiaga, Juan García-Bellido, and Vincent Vennin. "The exponential tail of inflationary fluctuations: consequences for primordial black holes". en. In: *Journal of Cosmology and Astroparticle Physics* 2020.03 (Mar. 2020), p. 029. ISSN: 1475-7516. DOI: 10.1088/1475-7516/2020/03/029.

[83] Daniel G. Figueroa et al. “Non-Gaussian Tail of the Curvature Perturbation in Stochastic Ultraslow-Roll Inflation: Implications for Primordial Black Hole Production”. In: *Physical Review Letters* 127.10 (Sept. 2021). Publisher: American Physical Society, p. 101302. DOI: 10.1103/PhysRevLett.127.101302.

[84] Shi Pi. “Primordial black hole formation in nonminimal curvaton scenarios”. In: *Physical Review D* 108.10 (2023). DOI: 10.1103/PhysRevD.108.L101301.

[85] Tomoaki Murata and Yuichiro Tada. *Stochastic-tail of the curvature perturbation in hybrid inflation*. arXiv:2507.22439 [astro-ph]. July 2025. DOI: 10.48550/arXiv.2507.22439.

[86] B. Gnedenko. “Sur La Distribution Limite Du Terme Maximum D’Une Série Aléatoire”. In: *Annals of Mathematics* 44.3 (1943). Publisher: [Annals of Mathematics, Trustees of Princeton University on Behalf of the Annals of Mathematics, Mathematics Department, Princeton University], pp. 423–453. ISSN: 0003-486X. DOI: 10.2307/1968974.

[87] Emil Julius Gumbel. *Statistics of extremes*. Columbia university press, 1958.

[88] Harald Cramér. *Mathematical Methods of Statistics*. en. Google-Books-ID: jV2YDwAAQBAJ. Princeton University Press, Apr. 1999. ISBN: 978-0-691-00547-8.

[89] Dionissios T. Hristopulos. *Random Fields for Spatial Data Modeling: A Primer for Scientists and Engineers*. en. Advances in Geographic Information Science. Dordrecht: Springer Netherlands, 2020. ISBN: 978-94-024-1916-0 978-94-024-1918-4. DOI: 10.1007/978-94-024-1918-4.

[90] P. D. Naselsky and D. I. Novikov. “General Statistical Properties of the Cosmic Microwave Background Polarization Field”. en. In: *The Astrophysical Journal* 507.1 (Nov. 1998). Publisher: IOP Publishing, p. 31. ISSN: 0004-637X. DOI: 10.1086/306294.

[91] Jaan Kasak. “Statistics of nonpolarized points in the CMB polarization maps”. In: *Physical Review D* 104.2 (2021). DOI: 10.1103/PhysRevD.104.023502.

[92] Ian Jolliffe. “Principal component analysis”. In: *International encyclopedia of statistical science*. Springer, 2011, pp. 1094–1096.

[93] Jonathon Shlens. *A Tutorial on Principal Component Analysis*. arXiv:1404.1100 [cs]. Apr. 2014. DOI: 10.48550/arXiv.1404.1100.

[94] L. Delchambre. "Weighted principal component analysis: a weighted covariance eigendecomposition approach". In: *Monthly Notices of the Royal Astronomical Society* 446.4 (Feb. 2015), pp. 3545–3555. ISSN: 0035-8711. DOI: 10.1093/mnras/stu2219.

[95] Ya. B. Zel'dovich. "Gravitational instability: An approximate theory for large density perturbations." In: *Astronomy and Astrophysics* 5 (Mar. 1970). Publisher: EDP ADS Bibcode: 1970A&A.....5...84Z, pp. 84–89. ISSN: 0004-6361.

[96] P. J. E. Peebles. *The large-scale structure of the universe*. Publication Title: Large-Scale Structure of the Universe by Phillip James Edwin Peebles. Princeton University Press ADS Bibcode: 1980lssu.book.....P. Jan. 1980.

[97] Scott Dodelson and Fabian Schmidt. *Modern Cosmology*. Publication Title: Modern Cosmology ADS Bibcode: 2020moco.book.....D. Jan. 2020. DOI: 10.1016/C2017-0-01943-2.

[98] Volker Springel et al. "Simulations of the formation, evolution and clustering of galaxies and quasars". en. In: *Nature* 435.7042 (June 2005). Publisher: Nature Publishing Group, pp. 629–636. ISSN: 1476-4687. DOI: 10.1038/nature03597.

[99] David Layzer. "A Preface to Cosmogony. I. The Energy Equation and the Virial Theorem for Cosmic Distributions." In: *The Astrophysical Journal* 138 (July 1963). Publisher: IOP ADS Bibcode: 1963ApJ...138..174L, p. 174. ISSN: 0004-637X. DOI: 10.1086/147625.

[100] Craig L. Sarazin. "X-ray emission from clusters of galaxies". In: *Reviews of Modern Physics* 58.1 (1986), pp. 1–115. DOI: 10.1103/RevModPhys.58.1.

[101] Ya. B. Zeldovich and R. A. Sunyaev. "The Interaction of Matter and Radiation in a Hot-Model Universe". In: *Astrophysics and Space Science* 4 (July 1969). Publisher: Springer ADS Bibcode: 1969Ap&SS...4..301Z, pp. 301–316. ISSN: 0004-640X. DOI: 10.1007/BF00661821.

[102] Yuval Birnboim and Avishai Dekel. "Virial shocks in galactic haloes?" In: *Monthly Notices of the Royal Astronomical Society* 345.1 (Oct. 2003), pp. 349–364. ISSN: 0035-8711. DOI: 10.1046/j.1365-8711.2003.06955.x.

[103] Francesco Miniati et al. "Properties of Cosmic Shock Waves in Large-Scale StructureFormation". en. In: *The Astrophysical Journal* 542.2 (Oct. 2000). Publisher: IOP Publishing, p. 608. ISSN: 0004-637X. DOI: 10.1086/317027.

[104] Dongsu Ryu et al. “Cosmological Shock Waves and Their Role in the Large-Scale Structure of the Universe”. en. In: *The Astrophysical Journal* 593.2 (Aug. 2003). Publisher: IOP Publishing, p. 599. ISSN: 0004-637X. DOI: 10.1086/376723.

[105] K. Dolag et al. “Turbulent gas motions in galaxy cluster simulations: the role of smoothed particle hydrodynamics viscosity”. en. In: *Monthly Notices of the Royal Astronomical Society* 364.3 (Dec. 2005). Publisher: Oxford Academic, pp. 753–772. ISSN: 0035-8711. DOI: 10.1111/j.1365-2966.2005.09630.x.

[106] F. Vazza et al. “Turbulent motions and shocks waves in galaxy clusters simulated with adaptive mesh refinement”. en. In: *Astronomy & Astrophysics* 504.1 (Sept. 2009). Publisher: EDP Sciences, pp. 33–43. ISSN: 0004-6361, 1432-0746. DOI: 10.1051/0004-6361/200912535.

[107] Andrey V. Kravtsov and Stefano Borgani. “Formation of Galaxy Clusters”. en. In: *Annual Review of Astronomy and Astrophysics* 50.Volume 50, 2012 (Sept. 2012). Publisher: Annual Reviews, pp. 353–409. ISSN: 0066-4146, 1545-4282. DOI: 10.1146/annurev-astro-081811-125502.

[108] I. Zhuravleva et al. “Turbulent heating in galaxy clusters brightest in X-rays”. en. In: *Nature* 515.7525 (Nov. 2014). Publisher: Nature Publishing Group, pp. 85–87. ISSN: 1476-4687. DOI: 10.1038/nature13830.

[109] Francesco Miniati. “THE MATRYOSHKA RUN: A EULERIAN REFINEMENT STRATEGY TO STUDY THE STATISTICS OF TURBULENCE IN VIRIALIZED COSMIC STRUCTURES”. en. In: *The Astrophysical Journal* 782.1 (Jan. 2014). Publisher: The American Astronomical Society, p. 21. ISSN: 0004-637X. DOI: 10.1088/0004-637X/782/1/21.

[110] R. A. Sunyaev and Ya. B. Zeldovich. “Small-Scale Fluctuations of Relic Radiation”. In: *Astrophysics and Space Science* 7 (Apr. 1970). Publisher: Springer ADS Bibcode: 1970Ap&SS...7....3S, pp. 3–19. ISSN: 0004-640X. DOI: 10.1007/BF00653471.

[111] R. A. Sunyaev and Ya. B. Zeldovich. “The Observations of Relic Radiation as a Test of the Nature of X-Ray Radiation from the Clusters of Galaxies”. In: *Comments on Astrophysics and Space Physics* 4 (Nov. 1972). ADS Bibcode: 1972CoASP...4..173S, p. 173. ISSN: 0010-26790146-2970.

[112] R. A. Sunyaev and Ia. B. Zeldovich. "Microwave background radiation as a probe of the contemporary structure and history of the universe". In: *Annual Review of Astronomy and Astrophysics* 18 (Jan. 1980). ADS Bibcode: 1980ARA&A..18..537S, pp. 537–560. ISSN: 0066-4146. DOI: 10.1146/annurev.aa.18.090180.002541.

[113] John E. Carlstrom, Gilbert P. Holder, and Erik D. Reese. "Cosmology with the Sunyaev-Zel'dovich Effect". en. In: *Annual Review of Astronomy and Astrophysics* 40.Volume 40, 2002 (Sept. 2002). Publisher: Annual Reviews, pp. 643–680. ISSN: 0066-4146, 1545-4282. DOI: 10.1146/annurev.astro.40.060401.093803.

[114] Mark Birkinshaw. "The Sunyaev–Zel'dovich effect". In: *Physics Reports* 310.2 (Mar. 1999), pp. 97–195. ISSN: 0370-1573. DOI: 10.1016/S0370-1573(98)00080-5.

[115] Wayne Hu and Scott Dodelson. "Cosmic Microwave Background Anisotropies". en. In: *Annual Review of Astronomy and Astrophysics* 40.Volume 40, 2002 (Sept. 2002). Publisher: Annual Reviews, pp. 171–216. ISSN: 0066-4146, 1545-4282. DOI: 10.1146/annurev.astro.40.060401.093926.

[116] Tony Mroczkowski et al. "Astrophysics with the Spatially and Spectrally Resolved Sunyaev-Zeldovich Effects: A Millimetre/Submillimetre Probe of the Warm and Hot Universe". In: *Space Science Reviews* 215.1 (Feb. 2019). arXiv:1811.02310 [astro-ph], p. 17. ISSN: 0038-6308, 1572-9672. DOI: 10.1007/s11214-019-0581-2.

[117] E. Komatsu and U. Seljak. "The Sunyaev-Zel'dovich angular power spectrum as a probe of cosmological parameters". In: *Monthly Notices of the Royal Astronomical Society* 336 (Nov. 2002). Publisher: OUP ADS Bibcode: 2002MNRAS.336.1256K, pp. 1256–1270. ISSN: 0035-8711. DOI: 10.1046/j.1365-8711.2002.05889.x.

[118] Yin-Zhe Ma et al. "Probing the diffuse baryon distribution with the lensing-tSZ cross-correlation". en. In: *Journal of Cosmology and Astroparticle Physics* 2015.09 (Sept. 2015), p. 046. ISSN: 1475-7516. DOI: 10.1088/1475-7516/2015/09/046.

[119] Tony Mroczkowski et al. "Astrophysics with the Spatially and Spectrally Resolved Sunyaev-Zeldovich Effects". en. In: *Space Science Reviews* 215.1 (Feb. 2019), p. 17. ISSN: 1572-9672. DOI: 10.1007/s11214-019-0581-2.

[120] L. Van Waerbeke et al. "CFHTLenS: mapping the large-scale structure with gravitational lensing". In: *Monthly Notices of the Royal Astronomical Society* 433.4 (Aug. 2013), pp. 3373–3388. ISSN: 0035-8711. DOI: 10.1093/mnras/stt971.

[121] Ludovic Van Waerbeke. "Detection of warm and diffuse baryons in large scale structure from the cross correlation of gravitational lensing and the thermal Sunyaev-Zeldovich effect". In: *Physical Review D* 89.2 (2014). DOI: 10.1103/PhysRevD.89.023508.

[122] J. Colin Hill and David N. Spergel. "Detection of thermal SZ-CMB lensing cross-correlation in Planck nominal mission data". en. In: *Journal of Cosmology and Astroparticle Physics* 2014.02 (Feb. 2014), p. 030. ISSN: 1475-7516. DOI: 10.1088/1475-7516/2014/02/030.

[123] Vinu Vikram, Adam Lidz, and Bhuvnesh Jain. "A Measurement of the Galaxy Group-Thermal Sunyaev-Zel'dovich Effect Cross-Correlation Function". In: *Monthly Notices of the Royal Astronomical Society* 467 (May 2017). Publisher: OUP ADS Bibcode: 2017MNRAS.467.2315V, pp. 2315–2330. ISSN: 0035-8711. DOI: 10.1093/mnras/stw3311.

[124] S. Pandey et al. "Constraints on the redshift evolution of astrophysical feedback with Sunyaev-Zel'dovich effect cross-correlations". en. In: *Physical Review D* 100.6 (Sept. 2019), p. 063519. ISSN: 2470-0010, 2470-0029. DOI: 10.1103/PhysRevD.100.063519.

[125] Nick Koukoufilippas et al. "Tomographic measurement of the intergalactic gas pressure through galaxy-tSZ cross-correlations". In: *Monthly Notices of the Royal Astronomical Society* 491 (Feb. 2020). Publisher: OUP ADS Bibcode: 2020MNRAS.491.5464K, pp. 5464–5480. ISSN: 0035-8711. DOI: 10.1093/mnras/stz3351.

[126] Yi-Kuan Chiang et al. "The Cosmic Thermal History Probed by Sunyaev–Zeldovich Effect Tomography". en. In: *The Astrophysical Journal* 902.1 (Oct. 2020). Publisher: The American Astronomical Society, p. 56. ISSN: 0004-637X. DOI: 10.3847/1538-4357/abb403.

[127] Sam Young, Eiichiro Komatsu, and Klaus Dolag. "Testing the Sunyaev-Zeldovich-based tomographic approach to the thermal history of the Universe with pressure-density cross correlations: Insights from the Magneticum simulation". In: *Physical Review D* 104.8 (Oct. 2021). Publisher: American Physical Society, p. 083538. DOI: 10.1103/PhysRevD.104.083538.

[128] Ziyang Chen. "Statistics of thermal gas pressure as a probe of cosmology and galaxy formation". In: *Physical Review D* 109.6 (2024). DOI: 10.1103/PhysRevD.109.063513.

[129] Sara Maleubre et al. *The impact of galaxy bias on cross-correlation tomography*. arXiv:2508.05319 [astro-ph]. Aug. 2025. DOI: 10.48550/arXiv.2508.05319.

[130] Marcel P. van Daalen et al. "The effects of galaxy formation on the matter power spectrum: a challenge for precision cosmology". In: *Monthly Notices of the Royal Astronomical Society* 415.4 (Aug. 2011), pp. 3649–3665. ISSN: 0035-8711. DOI: 10.1111/j.1365-2966.2011.18981.x.

[131] Klaus Dolag et al. *Encyclopedia Magneticum: Scaling Relations from Cosmic Dawn to Present Day*. arXiv:2504.01061 [astro-ph]. Apr. 2025. DOI: 10.48550/arXiv.2504.01061.

[132] Volker Springel. "The cosmological simulation code gadget-2". en. In: *Monthly Notices of the Royal Astronomical Society* 364.4 (Dec. 2005), pp. 1105–1134. ISSN: 0035-8711, 1365-2966. DOI: 10.1111/j.1365-2966.2005.09655.x.

[133] A. M. Beck et al. "An improved SPH scheme for cosmological simulations". In: *Monthly Notices of the Royal Astronomical Society* 455.2 (Jan. 2016), pp. 2110–2130. ISSN: 0035-8711. DOI: 10.1093/mnras/stv2443.

[134] V. Springel and L. Hernquist. "Cosmological smoothed particle hydrodynamics simulations: the entropy equation". en. In: *Monthly Notices of the Royal Astronomical Society* 333.3 (July 2002), pp. 649–664. ISSN: 0035-8711, 1365-2966. DOI: 10.1046/j.1365-8711.2002.05445.x.

[135] E. Komatsu et al. "SEVEN-YEAR WILKINSON MICROWAVE ANISOTROPY PROBE (WMAP*) OBSERVATIONS: COSMOLOGICAL INTERPRETATION". en. In: *The Astrophysical Journal Supplement Series* 192.2 (Jan. 2011). Publisher: The American Astronomical Society, p. 18. ISSN: 0067-0049. DOI: 10.1088/0067-0049/192/2/18.

[136] Volker Springel and Lars Hernquist. "Cosmological smoothed particle hydrodynamics simulations: a hybrid multiphase model for star formation". In: *Monthly Notices of the Royal Astronomical Society* 339.2 (Feb. 2003), pp. 289–311. ISSN: 0035-8711. DOI: 10.1046/j.1365-8711.2003.06206.x.

[137] D. Fabjan et al. "Simulating the effect of active galactic nuclei feedback on the metal enrichment of galaxy clusters". In: *Monthly Notices of the Royal Astronomical Society* 401.3 (Jan. 2010), pp. 1670–1690. ISSN: 0035-8711. DOI: 10.1111/j.1365-2966.2009.15794.x.

[138] Volker Springel, Tiziana di Matteo, and Lars Hernquist. "Modelling feedback from stars and black holes in galaxy mergers". In: *Monthly Notices of the Royal Astronomical Society* 361.3 (Aug. 2005), pp. 776–794. ISSN: 0035-8711. DOI: 10.1111/j.1365-2966.2005.09238.x.

[139] Volker Springel, Tiziana Di Matteo, and Lars Hernquist. "Black Holes in Galaxy Mergers: The Formation of Red Elliptical Galaxies". en. In: *The Astrophysical Journal* 620.2 (Jan. 2005). Publisher: IOP Publishing, p. L79. ISSN: 0004-637X. DOI: 10.1086/428772.

[140] Michaela Hirschmann et al. "Cosmological simulations of black hole growth: AGN luminosities and downsizing". In: *Monthly Notices of the Royal Astronomical Society* 442.3 (Aug. 2014), pp. 2304–2324. ISSN: 0035-8711. DOI: 10.1093/mnras/stu1023.

[141] L. Tornatore et al. "Chemical enrichment of galaxy clusters from hydrodynamical simulations". In: *Monthly Notices of the Royal Astronomical Society* 382.3 (Nov. 2007), pp. 1050–1072. ISSN: 0035-8711. DOI: 10.1111/j.1365-2966.2007.12070.x.

[142] L. Tornatore et al. "Simulating the metal enrichment of the intracluster medium". In: *Monthly Notices of the Royal Astronomical Society* 349.1 (Mar. 2004), pp. L19–L24. ISSN: 0035-8711. DOI: 10.1111/j.1365-2966.2004.07689.x.

[143] Robert P. C. Wiersma et al. "Chemical enrichment in cosmological, smoothed particle hydrodynamics simulations". In: *Monthly Notices of the Royal Astronomical Society* 399.2 (Oct. 2009), pp. 574–600. ISSN: 0035-8711. DOI: 10.1111/j.1365-2966.2009.15331.x.

[144] K. Dolag, E. Komatsu, and R. Sunyaev. "SZ effects in the Magneticum Pathfinder simulation: comparison with the Planck, SPT, and ACT results". In: *Monthly Notices of the Royal Astronomical Society* 463.2 (Dec. 2016), pp. 1797–1811. ISSN: 0035-8711. DOI: 10.1093/mnras/stw2035.

[145] K. Dolag et al. "Numerical study of halo concentrations in dark-energy cosmologies". en. In: *Astronomy & Astrophysics* 416.3 (Mar. 2004). Publisher: EDP Sciences, pp. 853–864. ISSN: 0004-6361, 1432-0746. DOI: 10.1051/0004-6361:20031757.

[146] Klaus Dolag et al. "Constrained simulations of the magnetic field in the local Universe and the propagation of ultrahigh energy cosmic rays". en. In: *Journal of Cosmology and Astroparticle Physics* 2005.01 (Jan. 2005), p. 009. ISSN: 1475-7516. DOI: 10.1088/1475-7516/2005/01/009.

[147] K. Dolag and F. Stasyszyn. "An MHD gadget for cosmological simulations". In: *Monthly Notices of the Royal Astronomical Society* 398.4 (Oct. 2009), pp. 1678–1697. ISSN: 0035-8711. DOI: 10.1111/j.1365-2966.2009.15181.x.

[148] Giorgia Pollina et al. "On the linearity of tracer bias around voids". In: *Monthly Notices of the Royal Astronomical Society* 469.1 (July 2017), pp. 787–799. ISSN: 0035-8711. DOI: 10.1093/mnras/stx785.

[149] V. Biffi, K. Dolag, and H. Böhringer. "Investigating the velocity structure and X-ray observable properties of simulated galaxy clusters with PHOX". In: *Monthly Notices of the Royal Astronomical Society* 428.2 (Jan. 2013), pp. 1395–1409. ISSN: 0035-8711. DOI: 10.1093/mnras/sts120.

[150] Lisa K. Steinborn et al. "Origin and properties of dual and offset active galactic nuclei in a cosmological simulation at $\boldsymbol {z=2}$". In: *Monthly Notices of the Royal Astronomical Society* 458.1 (May 2016), pp. 1013–1028. ISSN: 0035-8711. DOI: 10.1093/mnras/stw316.

[151] Klaus Dolag, Emilio Mevius, and Rhea-Silvia Remus. "Distribution and Evolution of Metals in the Magneticum Simulations". en. In: *Galaxies* 5.3 (Sept. 2017). Publisher: Multidisciplinary Digital Publishing Institute, p. 35. ISSN: 2075-4434. DOI: 10.3390/galaxies5030035.

[152] Rhea-Silvia Remus et al. "The co-evolution of total density profiles and central dark matter fractions in simulated early-type galaxies". In: *Monthly Notices of the Royal Astronomical Society* 464.3 (Jan. 2017), pp. 3742–3756. ISSN: 0035-8711. DOI: 10.1093/mnras/stw2594.

[153] Adelheid F. Teklu et al. "The morphology–density relation: impact on the satellite fraction". In: *Monthly Notices of the Royal Astronomical Society* 472.4 (Dec. 2017), pp. 4769–4785. ISSN: 0035-8711. DOI: 10.1093/mnras/stx2303.

[154] Rhea-Silvia Remus, Klaus Dolag, and Tadziu L. Hoffmann. "The Outer Halos of Very Massive Galaxies: BCGs and their DSC in the Magneticum Simulations". en. In: *Galaxies* 5.3 (Sept. 2017). Publisher: Multidisciplinary Digital Publishing Institute, p. 49. ISSN: 2075-4434. DOI: 10.3390/galaxies5030049.

[155] Adelheid F. Teklu et al. "CONNECTING ANGULAR MOMENTUM AND GALACTIC DYNAMICS: THE COMPLEX INTERPLAY BETWEEN SPIN, MASS, AND MORPHOLOGY". en. In: *The Astrophysical Journal* 812.1 (Oct.

2015). Publisher: The American Astronomical Society, p. 29. ISSN: 0004-637X. DOI: 10.1088/0004-637X/812/1/29.

[156] Tiago Castro et al. "On the impact of baryons on the halo mass function, bias, and cluster cosmology". In: *Monthly Notices of the Royal Astronomical Society* 500.2 (Jan. 2021), pp. 2316–2335. ISSN: 0035-8711. DOI: 10.1093/mnras/staa3473.

[157] Antonio Ragagnin et al. "Dependency of halo concentration on mass, redshift and fossilness in Magneticum hydrodynamic simulations". In: *Monthly Notices of the Royal Astronomical Society* 486.3 (July 2019), pp. 4001–4012. ISSN: 0035-8711. DOI: 10.1093/mnras/stz1103.

[158] Bjoern Soergel et al. "Cosmology with the pairwise kinematic SZ effect: calibration and validation using hydrodynamical simulations". In: *Monthly Notices of the Royal Astronomical Society* 478.4 (Aug. 2018), pp. 5320–5335. ISSN: 0035-8711. DOI: 10.1093/mnras/sty1324.

[159] N. Gupta et al. "SZE observables, pressure profiles and centre offsets in Magneticum simulation galaxy clusters". In: *Monthly Notices of the Royal Astronomical Society* 469.3 (Aug. 2017), pp. 3069–3087. ISSN: 0035-8711. DOI: 10.1093/mnras/stx715.

[160] Sebastian Bocquet et al. "Halo mass function: baryon impact, fitting formulae, and implications for cluster cosmology". In: *Monthly Notices of the Royal Astronomical Society* 456.3 (Mar. 2016), pp. 2361–2373. ISSN: 0035-8711. DOI: 10.1093/mnras/stv2657.

[161] K. Dolag et al. "Constraints on the distribution and energetics of fast radio bursts using cosmological hydrodynamic simulations". In: *Monthly Notices of the Royal Astronomical Society* 451.4 (Aug. 2015), pp. 4277–4289. ISSN: 0035-8711. DOI: 10.1093/mnras/stv1190.

[162] Asantha Cooray and Ravi Sheth. "Halo Models of Large Scale Structure". In: *Physics Reports* 372.1 (Dec. 2002). arXiv:astro-ph/0206508, pp. 1–129. ISSN: 03701573. DOI: 10.1016/S0370-1573(02)00276-4.

[163] Marika Asgari, Alexander J. Mead, and Catherine Heymans. "The halo model for cosmology: a pedagogical review". In: *The Open Journal of Astrophysics* 6 (Nov. 2023). arXiv:2303.08752 [astro-ph], 10.21105/astro.2303.08752. ISSN: 2565-6120. DOI: 10.21105/astro.2303.08752.

[164] P. a. R. Ade et al. “Planck intermediate results - V. Pressure profiles of galaxy clusters from the Sunyaev-Zeldovich effect”. en. In: *Astronomy & Astrophysics* 550 (Feb. 2013). Publisher: EDP Sciences, A131. ISSN: 0004-6361, 1432-0746. DOI: 10.1051/0004-6361/201220040.

[165] Benedikt Diemer. “COLOSSUS: A Python Toolkit for Cosmology, Large-scale Structure, and Dark Matter Halos”. en. In: *The Astrophysical Journal Supplement Series* 239.2 (Dec. 2018). Publisher: The American Astronomical Society, p. 35. ISSN: 0067-0049. DOI: 10.3847/1538-4365/aaee8c.

[166] Jeremy Tinker et al. “Toward a Halo Mass Function for Precision Cosmology: The Limits of Universality”. en. In: *The Astrophysical Journal* 688.2 (Dec. 2008). Publisher: IOP Publishing, p. 709. ISSN: 0004-637X. DOI: 10.1086/591439.

[167] Jeremy L. Tinker et al. “THE LARGE-SCALE BIAS OF DARK MATTER HALOS: NUMERICAL CALIBRATION AND MODEL TESTS”. en. In: *The Astrophysical Journal* 724.2 (Nov. 2010). Publisher: The American Astronomical Society, p. 878. ISSN: 0004-637X. DOI: 10.1088/0004-637X/724/2/878.

[168] Fabian Schmidt. “Towards a self-consistent halo model for the nonlinear large-scale structure”. In: *Physical Review D* 93.6 (Mar. 2016). ISSN: 2470-0029. DOI: 10.1103/physrevd.93.063512.

[169] Timothy S Bunch and Paul CW Davies. “Quantum field theory in de Sitter space: renormalization by point-splitting”. In: *Proceedings of the Royal Society of London. A. Mathematical and Physical Sciences* 360.1700 (1978), pp. 117–134.

[170] Jennie H. Traschen and Robert H. Brandenberger. “Particle production during out-of-equilibrium phase transitions”. In: *Phys. Rev. D* 42 (8 Oct. 1990), pp. 2491–2504. DOI: 10.1103/PhysRevD.42.2491.

[171] R. Arnowitt, S. Deser, and C. W. Misner. “Dynamical Structure and Definition of Energy in General Relativity”. In: *Physical Review* 116.5 (Dec. 1959). Publisher: American Physical Society, pp. 1322–1330. DOI: 10.1103/PhysRev.116.1322.

[172] R. Arnowitt, S. Deser, and C. W. Misner. “Canonical Variables for General Relativity”. In: *Physical Review* 117.6 (Mar. 1960). Publisher: American Physical Society, pp. 1595–1602. DOI: 10.1103/PhysRev.117.1595.

[173] Richard Arnowitt, Stanley Deser, and Charles W. Misner. “Republication of: The dynamics of general relativity”. en. In: *General Relativity and Gravitation* 40.9 (Sept. 2008), pp. 1997–2027. ISSN: 1572-9532. DOI: 10.1007/s10714-008-0661-1.

[174] Charles W. Misner, K. S. Thorne, and J. A. Wheeler. *Gravitation*. San Francisco: W. H. Freeman, 1973. ISBN: 978-0-7167-0344-0, 978-0-691-17779-3.

Acknowledgment

I would like to thank all the individuals who have supported and encouraged me throughout the course of this work. Your companionship has been one of my greatest rewards of my journey.

I wish to express my gratitude to my thesis supervisor, Professor Stefan Hofmann, who has offered me his invaluable guidance that has greatly influenced my research style, as well as my intellectual and personal growth. I am also indebted to Dr. James Creswell, Dr. Florian Kuhnel and Professor Dominik Schwarz for revealing to me the beauty of statistics and the magnificent landscape of the early Universe. Furthermore, I am grateful to Professor Klaus Dolag and Professor Eiichiro Komatsu for their valuable guidance on the fascinating topics on the large-scale structures of the Universe and their simulations. My sincere appreciation also extends to Ludwig Eglseer and Dr. Marc Schneider for their support and inspiring collaboration. Finally, I wish to express my gratitude to Daniel Bockisch, Carlo Alberto Cremonini, Katrin Hammer, Josef Kunisch and Mariam Khaldieh for their companionship and enjoyable moments we have shared.

I also owe my deepest gratitude to my family, whose encouragement and unwavering faith in me have been a constant source of strength.

This work is supported by the Excellence Cluster ORIGINS. The author would like to acknowledge the *Gauss Centre for Supercomputing e.V.* for providing the computational resources on the *GCS Supercomputer SuperMUC at Leibniz Supercomputing Centre*. Also, the author acknowledge the *High Performance Computation Linux Cluster*, administrated by the *Fakultät für Physik* in the *Ludwig-Maximilians-Universität München*, for providing their computational resources.